Dynamics of Atmospheres and Oceans, 2 (1978) 213—291

A DESCRIPTION OF NUMERICAL ANTARCTIC CIRCUMPOLAR CURRENTS *

JAMES C. McWILLIAMS, WILLIAM R. HOLLAND and JULIANNA H.S. CHOW
National Center for Atmospheric Research, Boulder, Colo. 80307 (U.S.A.)

(Received July 19, 1977; Revised January 19, 1978; Accepted January 19, 1978)

ABSTRACT

McWilliams, J.C., Holland, W.R. and Chow, J.H.S., 1978. A description of numerical Antarctic Circumpolar Currents. Dyn. Atmos. Oceans, 2: 213—291.

A sequence of numerical calculations has been made for the equilibrium balances of eddies and mean currents in open and partially blocked, periodic channels. The physical model employed is a two-layer, quasigeostrophic, wind-driven one, with important bottom friction and weak lateral friction. The resolved eddies provide the interior fluxes of momentum and potential vorticity which allow the mean state to be a balanced one. The set of calculations does not provide a parameter study as such, but does provide examples of the influences of alternative physical processes and geometrical constraints. These alternatives include the presence or absence of a partial barrier across the channel, the length of the channel, the addition of a transient component to the wind-driving, and the addition of a topographic sill across the channel gap. Particular attention is focused upon the steadily driven general circulation of a β-plane channel, because of the structural simplicity of the solution. The results may be broadly summarized as follows. The eddies are generated by a baroclinic instability of the mean flow. They act to intensify the upper layer mean jet and mean cross-jet potential vorticity gradient (through eddy horizontal Reynolds stress and relative vorticity flux divergence, respectively) and to transfer downwards mean zonal momentum, energy, and potential vorticity gradient (through eddy interfacial pressure drag, vertical pressure work, and vortex stretching flux divergence, respectively). In the case of a zonally uniform channel, the meridional heat flux is found not to conform closely to previously proposed parameterizations. The presence of a partial meridional barrier and a topographic obstacle are found to strongly influence the equilibrium solution, while neither a change in the basin length nor the presence of a transient wind component appear to importantly alter the solution.

1. INTRODUCTION

The general circulation of the world's oceans can, to some extent, be separated into distinct and perhaps only weakly related current systems. The most prominent separate systems would be the subtropical gyres (such as the Gulf Stream gyre in the North Atlantic Ocean), the zonally banded equatorial current systems (the countercurrents, the undercurrents), and the

---

* MODE Contribution No 92.

Antarctic Circumpolar Current. The present study is based upon isolated and idealized models of the latter. The foundations of the models comprise two related hypotheses, and the plausibility of the model results can be viewed as indirectly confirming them. The first hypothesis is that, apart from small-scale, turbulent boundary regions (whose contributions will be parameterized in our models), the important components of the general circulation are geostrophic. The second is that interior, homogeneous, down-gradient diffusions from small-scale turbulence are weak in the ocean, and that the inhomogeneous geostrophic eddy field, by itself, can provide the vertical and horizontal fluxes needed to maintain the mean currents.

The character of geostrophic (mesoscale) eddies and their probable role in the general circulation are research topics which are currently being actively pursued. In this decade several large, cooperative, mesoscale experiments have been or are being performed — Polygon (Brekhovskikh et al., 1971), MODE (W. Simmons et al., 1977), and POLYMODE (USPMOC, 1976), for example. In addition, a variety of other observations have demonstrated that mesoscale eddies are globally ubiquitous, though not with spatially uniform characteristics (e.g., Wyrtki et al., 1976). The greatest abundance of mesoscale observations occurs in the northern hemisphere subtropical gyres. The region of the Antarctic Circumpolar Current has especially sparse data, but they do support the existence of energetic mesoscale variability (Baker et al., 1977; T.J. Harris, personal communication, 1977). Because of the data sparseness, however, extensive comparisons between our model eddies and observed ones will not be possible.

Eddy-resolving, general circulation studies with numerical models have occurred in parallel with the mesoscale observations. The earliest work was that of Holland and Lin (1975a, b), which demonstrated that mesoscale eddies can develop from fluid instabilities of the more systematic currents and, in turn, provide significant Reynolds' stresses upon those currents. More recently, several additional numerical calculations have been reported, either within the geostrophic approximation (Haidvogel, 1976; Holland, 1977, 1978) or using primitive equation models (Robinson et al., 1977; Semtner and Mintz, 1977). A particular comparison by Semtner and Holland (1978) indicates that the differences between these two classes of models are unimportant for the circumstances examined to date.

The present study lies well within the preceding line of development. The numerical models which we use are among the simplest and, in our opinion, most fundamental of those above; that is, they are quasigeostrophic, two-layer, and wind-driven and have minimal explicit diffusion processes. None of these basic constraints are examined here; rather, they are accepted in order to efficiently examine a new geographical regime. The previous numerical calculations have been made for enclosed ocean basins, modeled after the subtropical gyres, where the mean currents are circular and flow in directions oblique to the winds; their motive force is at least partially through a Sverdrup vorticity balance (Sverdrup, 1947). In an open basin (a zonally continuous circumpolar region), however, the mean currents can be rectilinear and more directly driven by momentum transfer from the winds. The calculations reported below are intended to illustrate the nature of equilibrium balances between geostrophic eddies and mean currents in the open basin regime.

Two further restrictions of scope have been adopted. Firstly, we only intend here to describe the solutions, not completely "explain" them. This latter is inevitably a lengthier process than simply performing the calculations, and, in a complicated turbulent system, is perhaps most usefully done by developing simpler analogs of the behavior exhibited in the general circulation model. There are as yet too few useful and apt analogs for eddy-resolving numerical model results, though, as examples, we cite Rhines (1975), Bretherton and Haidvogel (1976), Salmon et al. (1976), and McWilliams (1977a). Nevertheless, a reasonably unbiased description of the results should serve as a target for developing these analogs — much as a purely descriptive observational paper might. Secondly, the set of calculations is intended only as a survey of various processes which influence the Circumpolar Current, not as a comprehensive parameter study. To do the latter properly, one would have to identify all of the possible physical regimes and document the nature of the transitions between them. Thus, our purpose here is a more preliminary one. If the results of the present phenomenological survey warrant it, a careful parametric study could follow.

2. THE MODEL EQUATIONS AND SELECTED BUDGETS

The equations of the numerical model are those appropriate to a hydrostatic, adiabatic, quasigeostrophic, two-layer (or two-level; the two formulations are indistinguishable in the quasigeostrophic approximation) fluid which is driven by a body force in the upper layer (a depth-distributed surface stress) and dissipated by a fourth order lateral friction and a Rayleigh friction (a bottom drag) in the lower layer. These equations will simply be stated here; for a derivation the reader is referred to McWilliams (1977b).

The basic equations of the model are potential vorticity balances in each layer:

$$\begin{aligned}\frac{\partial q_1}{\partial t} + J(\psi_1, q_1) &= \operatorname{curl} \underset{\sim}{\tau} - A_4 H_1 \nabla^6 \psi_1 \\ \frac{\partial q_3}{\partial t} + J(\psi_3, q_3) &= -\epsilon H_3 \nabla^2 \psi_3 - A_4 H_3 \nabla^6 \psi_3\end{aligned} \tag{1}$$

In these equations, the two layers are indicated by subscripts 1 and 3, the ψ_i are velocity streamfunctions ($u_i = -\psi_{iy}$, $v_i = \psi_{ix}$; $i = 1, 3$), the H_i are average layer thicknesses, $\underset{\sim}{\tau}$ is a surface wind stress divided by the water density, ϵ is a coefficient of bottom friction, and A_4 is a coefficient of a fourth order lateral viscosity. The rationale behind using a scale-selective, higher order lateral viscosity is discussed in Holland (1978). The q_i are potential vorticities multiplied by H_i^2:

$$\begin{aligned} q_1 &= H_1\nabla^2\psi_1 - (f_0^2/g')(\psi_1 - \psi_3) + H_1 f \\ q_3 &= H_3\nabla^2\psi_3 + (f_0^2/g')(\psi_1 - \psi_3) + H_3 f + f_0 B \end{aligned} \qquad (2)$$

where $f = f_0 + \beta(y - y_0)$, $B(x, y)$ is the elevation of the bottom above its mean level, and $g' = g\,\Delta\rho/\rho$ is the reduced gravitational constant based upon the relative change in density between the fluid layers.

The fluid domain is that of a zonal channel with an imposed length of zonal periodicity L_x. In addition, in most cases there is a partial barrier across the channel, extending over the full fluid depth where it is present, but leaving a gap in the walls along $x = 0$ and L_x. This domain is the Cartesian approximation to an annulus with radial barriers extending towards each other from the inner and outer walls. This, in turn, is an idealization of the geometry of the Antarctic Circumpolar region where the Drake Passage provides the greatest constriction of the flow.

The boundary conditions for (1) are:

$$\psi_i = \begin{cases} c_{iN}(t) \text{ on the northern solid wall } \delta\Omega_N \\ c_{iS}(t) \text{ on the southern solid wall } \delta\Omega_S \end{cases} \qquad (3)$$

$$\nabla^2\psi_i = \nabla^4\psi_i = 0 \text{ on both solid walls}$$

(for $i = 1, 3$) with all quantities periodic in the gap. The conditions (3) are appropriate to no flow through the walls, no flux of tangential momentum through the walls (i.e., free slip of the fluid), and no external energy sources for the fluid as a result of the fourth order friction. The functions of time only (c_{iN} and c_{iS}) must be determined from auxiliary conditions (McWilliams, 1977b). For the geometry described above, the southern wall can be thought of as bounding an interior island (i.e., Antarctica), and four auxiliary conditions are required (one for each c). The following ones have been adopted for our model:

ⓐ $H_1 c_{1N} + H_3 c_{3N} = 0 \quad \text{on } \delta\Omega_N$

ⓑ $\displaystyle\iint_\Omega (\psi_1 - \psi_3)\mathrm{d}x\,\mathrm{d}y = 0$

ⓒ $$\int_0^{L_x} \left\{\frac{\partial}{\partial y}\left[\frac{\partial}{\partial t}(H_1\psi_1 + H_3\psi_3) + H_1\psi_{1,x}\psi_{1,y} + H_3\psi_{3,x}\psi_{3,y}\right] + \underset{\sim}{\tau}\cdot\hat{e}_x \right. \qquad (4)$$
$$\left. + f_0 B\psi_{3,x} + H_3\epsilon\psi_{3,y} + A_4(H_1\nabla^4\psi_{1,y} + H_3\nabla^4\psi_{3,y})\right\}\Bigg|_{y=\hat{y}} \mathrm{d}x = 0$$

ⓓ $$\oint_{\delta\Omega_S} \left\{(\partial_t + A_4\nabla^4)\frac{\partial\psi_1}{\partial n} - \underset{\sim}{\tau}\cdot\hat{s}/H_1\right\}\mathrm{d}s = 0$$

Condition ⓐ is an arbitrary elimination of the barotropic pressure signal on $\delta\Omega_N$; condition ⓑ prevents net mass exchange between the layers; condition ⓒ is a transport circulation integral around the southern boundary (i.e., Antarctica); and condition ⓓ, together with ⓑ and ⓒ, assures mass conservation for the upper layer. In (4), Ω is the entire fluid domain $\{x, y \mid 0 < x < L_x, 0 < y < L_y\}$, $\hat{y}$ is the meridional coordinate of a zonal line centered in the gap [i.e., $\hat{y} = 1/2(y_N + y_S)$ where y_S and y_N define the meridional extremes of the gap], $\delta\Omega_S$ and $\delta\Omega_N$ define the island and exterior solid walls respectively [e.g., $\delta\Omega_S = \{x, y \mid (x = 0, 0 \leqslant y \leqslant y_S) \cup (0 \leqslant x \leqslant L_x, y = 0) \cup (x = L_x, 0 \leqslant x \leqslant y_S)\}$], and s and n (with unit vectors $\hat{s}$ and $\hat{n}$) define coordinates parallel and outwardly normal to the boundary. The integrals in (4), as well as all other ones in this paper, should be interpreted as integral averages.

The equations (1)–(4) are sufficient to fully determine the evolution of the streamfunctions in each layer. For numerical integrations, of course, particular discretizations must be applied. The formulas we have used are standard, second-order, centered finite differences which are spatially consistent and spatially conservative in the sense of Arakawa (1966). For explicit formulas the reader is referred to Appendix A.

Various integral budgets of the equations will be useful in analyzing the numerical solutions. In particular, we shall record here the budget equations for an area and time average of energy, and zonal and time averages of zonal momentum and potential vorticity. The reader might prefer to skip ahead to section 3 and return to the budget equations where necessary.

For an energy budget over the whole domain, we partition the flow into time averaged and fluctuating (eddy) components; for example:

$$\begin{aligned} \psi_i &= \overline{\psi}_i + \psi_i' \\ \overline{\psi}_i &= \int_{t_0}^{t_0+T} \psi_i \, dt \end{aligned} \tag{5}$$

where t_0 is a time within the equilibrium period for the solutions and T is the averaging interval (recall our convention of writing integral averages simply as integrals). We shall discuss first the budget for six types of energy, composed of mean and eddy, layer integrated kinetic and potential energies:

$$\begin{aligned} &\left.\begin{aligned} K_i &\equiv \tfrac{1}{2} H_i \iint_\Omega \nabla\overline{\psi}_i \cdot \nabla\overline{\psi}_i \, dx\, dy \\ K_i' &\equiv \tfrac{1}{2} H_i \iint_\Omega \overline{\nabla\psi_i' \cdot \nabla\psi_i'} \, dx\, dy \end{aligned}\right\} i = 1, 3 \\ &P \equiv \tfrac{1}{2} f_0^2/g' \iint (\overline{\psi}_1 - \overline{\psi}_3)^2 \\ &P' \equiv \tfrac{1}{2} f_0^2/g' \iint \overline{(\psi_1' - \psi_3')^2} \end{aligned} \tag{6}$$

The balance equations for these energies can be written in the following form:

$$\begin{aligned}
\overline{K_{1t}} &= \{\tau, K_1\} - \{K_1, A_4\} + \{K_1', K_1\} - \{K_1, P\} \\
\overline{K_{3t}} &= -\{K_3, P\} - \{K_3, A_4\} - \{K_3, \epsilon\} + \{K_3', K_3\} \\
\overline{K_{1t}'} &= \{\tau, K_1'\} - \{K_1', A_4\} - \{K_1', K_1\} + \{P', K_1'\} \\
\overline{K_{3t}'} &= -\{K_3', A_4\} - \{K_3', \epsilon\} - \{K_3', K_3\} + \{P', K_3'\} \\
\overline{P_t} &= \{K_1, P\} + \{K_3, P\} - \{P, P'\} \\
\overline{P_t'} &= -\{P', K_1'\} - \{P', K_3'\} + \{P, P'\}
\end{aligned} \tag{7}$$

where the transfer terms on the right-hand sides of (7) are written in a notation which indicates the type of transfer which can occur. Explicitly, these transfer terms are:

$$\begin{aligned}
\{\tau, K_1\} &= -\hat{e}_z \cdot \iint \overline{\underset{\sim}{\tau}} \times \nabla \overline{\psi}_1 \\
\{\tau, K_1'\} &= -\hat{e}_z \cdot \iint \overline{\underset{\sim}{\tau}' \times \nabla \psi_1'} \\
\{K_i, A_4\} &= H_1 A_4 \iint \nabla (\nabla^2 \overline{\psi}_i)^2 \\
\{K_i', A_4\} &= H_i A_4 \iint \overline{\nabla (\nabla^2 \psi_i')^2} \\
\{K_i', K_i\} &= H_i \iint \overline{\psi}_i \, \overline{J(\psi_i', \nabla^2 \psi_i')} \\
\{K_i, P\} &= (-1)^{(i+1)/2} f_0 \iint \overline{\omega} \overline{\psi}_i \\
\{P', K_i'\} &= (-1)^{(i-1)/2} f_0 \iint \overline{\omega' \psi_i'} \\
\{K_3, \epsilon\} &= H_3 \epsilon \iint \nabla \overline{\psi}_3^2 \\
\{K_3', \epsilon\} &= H_3 \epsilon \iint \overline{\nabla \psi_3'^2} \\
\{P, P'\} &= f_0 \iint \overline{\omega} (\overline{\psi}_3 - \overline{\psi}_1)
\end{aligned} \tag{8}$$

Various integrations by parts have been performed to obtain (6)—(8); also several applications of (4) were required. The vertical velocities which appear in (8) are:

$$\begin{aligned}
\overline{\omega} &= f_0/g' [\overline{(\psi_3 - \psi_1)_t} + J(\overline{\psi}_1, \overline{\psi}_3) + \overline{J(\psi_1', \psi_3')}] \\
\omega' &= f_0/g' [(\psi_3' - \psi_1')_t + J(\overline{\psi}_1, \psi_3') + J(\psi_1', \overline{\psi}_3)]
\end{aligned} \tag{9}$$

The budget equations (7) and (8) are equivalent to those of Holland (1978), with one exception. Holland defined $\{K_1, K_3\}$ and $\{K_1', K_3'\}$ exchanges in addition to kinetic-potential exchanges; in (7), these six exchanges have been absorbed into four kinetic-potential exchanges. Conversion formulas between the two representations are the following:

$$\left.\begin{aligned} \{K_i \hat{,} P\} &= \frac{H_i}{H}\left(\{K_1, P\} + \{K_3, P\}\right) \\ \{P' \hat{,} K_i'\} &= \frac{H_i}{H}\left(\{P', K_1'\} + \{P', K_3'\}\right) \end{aligned}\right\} (i = 1, 3)$$

$$\begin{aligned} \{K_1 \hat{,} K_3\} &= \frac{H_3}{H}\{K_1, P\} - \frac{H_1}{H}\{K_3, P\} \\ \{K_1' \hat{,} K_3'\} &= -\frac{H_3}{H}\{P', K_1'\} + \frac{H_1}{H}\{P', K_3'\} \end{aligned} \qquad (10)$$

where $H = H_1 + H_3$ and the caret indicates the transfer terms in Holland (1978). In a primitive equation model the six left-hand side terms in (10) are independent quantities; in a quasigeostrophic model, they are partially redundant as indicated in (10). All of these terms are pressure work terms (of the general form $\iint pw$), as discussed in Holland (1978).

For finite time averages, there are possible contributions to these budgets on the left sides of (7) from trends in the data set (i.e., the time average of a time derivative does not vanish). An example is:

$$\bar{K}_{1t} = -\frac{H_1}{T} \iint_{\Omega} \bar{\psi}_1[\nabla^2\psi_1'(t_0 + T) - \nabla^2\psi_1'(t_0)]\, \mathrm{d}x\, \mathrm{d}y \qquad (11)$$

which indicates an intermediate form, prior to integration by parts, in the derivation of the K_1 budget. In what follows, only the larger terms in (7) will be reported, and trend terms such as (11) are never among the larger ones. Therefore, we shall not systematically record the trend terms — neither for (7) nor the other integral budgets below.

In the predominately zonal geometry of our domain, it will also prove useful to further decompose the time mean field into a zonal average and a standing eddy component:

$$\begin{aligned} \bar{\psi}_i &\equiv \langle \bar{\psi}_i \rangle + \bar{\psi}_{*i} \\ \langle \bar{\psi}_i \rangle &= \int_0^{L_x} \bar{\psi}_i \, \mathrm{d}x \end{aligned} \qquad (12)$$

The various energies appropriate to such a decomposition are given by:

$$\left.\begin{aligned} K_{zi} &= \tfrac{1}{2}H_i \iint_{\Omega} \langle \overline{\psi}_i \rangle_y^2 \, \mathrm{d}x \, \mathrm{d}y \\ K_{*i} &= \tfrac{1}{2}H_i \iint \nabla \overline{\psi}_{*i}^2 \end{aligned}\right\} (i = 1, 3)$$

$$P_z = \tfrac{1}{2}f_0^2/g' \iint (\langle \overline{\psi}_1 \rangle - \langle \overline{\psi}_3 \rangle)^2 \tag{13}$$

$$P_* = \tfrac{1}{2}f_0^2/g' \iint (\overline{\psi}_{*1} - \overline{\psi}_{*3})^2$$

where $K_1 = K_{z1} + K_{*1}$, etc. The budget equations are:

$$\overline{K_{z1,t}} = \{\tau, K_{z1}\} - \{K_{z1}, A_4\} + \{K_1', K_{z1}\} + \{K_{*1}, K_{z1}\} - \{K_{z1}, P_z\}$$

$$\overline{K_{z3,t}} = -\{K_{z3}, A_4\} - \{K_{z3}, \epsilon\} + \{K_3', K_{z3}\} + \{K_{*3}, K_{z3}\}$$

$$- \{K_{z3}, P_z\} - \{K_{z3}, B\}$$

$$\overline{K_{*1,t}} = \{\tau, K_{*1}\} - \{K_{*1}, A_4\} - \{K_{*1}, K_{z1}\} + \{K_1', K_{*1}\} - \{K_{*1}, P_*\}$$

$$\overline{K_{*3,t}} = -\{K_{*3}, A_4\} - \{K_{*3}, \epsilon\} - \{K_{*3}, K_{z3}\} + \{K_3', K_{*3}\} \tag{14}$$

$$- \{K_{*3}, P_*\} + \{K_{z3}, B\}$$

$$\overline{P_{z,t}} = \{K_{z1}, P_z\} + \{K_{z3}, P_z\} - \{P_z, P_*\} - \{P_z, P'\}$$

$$\overline{P_{*,t}} = \{K_{*1}, P_*\} + \{K_{*3}, P_*\} + \{P_z, P_*\} - \{P_*, P'\}$$

where most of the transfer terms are defined in strict analogy to those in (8). The terms which are perhaps less directly analogous are defined by:

$$\{K_{zi}, A_4\} = H_i A_4 \iint \langle \overline{\psi}_i \rangle_{yyy} [\langle \overline{\psi}_i \rangle_{yyy} + \nabla^2 \overline{\psi}_{*i,y}]$$

$$\{K_{*i}, A_4\} = H_i A_4 \iint [\nabla (\nabla^2 \overline{\psi}_{*i})^2 + \langle \overline{\psi}_i \rangle_{yyy} \nabla^2 \overline{\psi}_{*i,y}]$$

$$\{K_{*i}, K_{zi}\} = H_i \iint \langle \overline{\psi}_i \rangle J(\overline{\psi}_{*i}, \nabla^2 \overline{\psi}_{*i}) \tag{15}$$

$$+ \frac{H_i}{l} \oint_{\delta\Omega} \langle \overline{\psi}_i \rangle [\overline{\psi_{i,nt}} + A_4 \nabla^4 \overline{\psi_{i,n}} + \delta_{i3} \epsilon \overline{\psi_{3,n}}] \mathrm{d}s$$

$$\{K_{zi}, P_z\} = f_0 (-1)^{(i-1)/2} \iint \langle \overline{\psi}_i \rangle \langle \overline{\omega} \rangle$$

(cont.)

(cont.)

$$\{K_{*i}, P_*\} = f_0(-1)^{(i+1)/2}\iint \overline{\psi}_{*i}\overline{\omega}_*$$

$$\{P_z, P_*\} = -f_0^2/g' \iint (\langle\overline{\psi}_1\rangle - \langle\overline{\psi}_3\rangle)\, J(\overline{\psi}_{*1}, \overline{\psi}_{*3}) \tag{15}$$

$$\{K_{z3}, B\} = -f_0 \iint \langle\overline{\psi}_3\rangle\, J(\overline{\psi}_3, B)$$

The line integral average in (15) is around the full boundary of Ω, δ_{i3} is a Kronecker delta function, and the length factor is $l = L_yL_x/[2(L_y + L_x)]$. The vertical velocities in (15) are defined by:

$$\langle\overline{\omega}\rangle = f_0/g'[\overline{\langle(\psi_3 - \psi_1)_t\rangle} + J(\overline{\psi}_{*1}, \overline{\psi}_{*3}) + \overline{\langle J(\psi_1', \psi_3')\rangle}]$$

$$\overline{\omega}_* = f_0/g'[\overline{(\psi_3 - \psi_1)_t} - \overline{\langle(\psi_3 - \psi_1)\rangle_t} + J(\langle\overline{\psi}_1\rangle, \overline{\psi}_{*3}) \tag{16}$$

$$+ J(\overline{\psi}_{*1}, \langle\overline{\psi}_3\rangle) + \overline{J(\psi_1', \psi_3')} - \overline{\langle J(\psi_1', \psi_3')\rangle}]$$

The budget equations (14) are equivalent to the mean energy equations in (7); their compatibility with the eddy energy budgets is assured by relations such as:

$$\{K_i', K_i\} = \{K_i', K_{zi}\} + \{K_i', K_{*i}\} \tag{17}$$

The zonal momentum is clearly a crucial quantity to monitor in a zonally driven, zonally open channel. The budgets in each layer for the time and zonal average of the zonal velocity $\langle\overline{u_i}\rangle$ can be written as:

$$H_1\overline{\langle u_1\rangle_t} = \overline{\underset{\sim}{\tau} \cdot \hat{e}_x} + A_1 + B_1 + C_1 + \mathcal{P}_1 - D_* - D'$$

$$H_3\overline{\langle u_3\rangle_t} = -H_3\epsilon\langle\overline{u_3}\rangle + A_3 + B_3 + C_3 + \mathcal{P}_3 + D_* + D' - E \tag{18}$$

where the source and sink terms are defined by:

$$A_i = H_iA_4 \int_0^{L_x} \nabla^4\overline{\psi}_{i,y}\, dx$$

$$B_i = H_i \int_0^{L_x} J(\overline{\psi}_{*i}, \overline{\psi}_{*i,y})\, dx$$

$$C_i = H_i \int_0^{L_x} \overline{J(\psi_i', \psi_{i,y}')}\, dx \tag{19}$$

$$\mathcal{P}_i = H_i/L_x[\overline{p_i^{(1)}(x = L_x)} - \overline{p_i^{(1)}(x = 0)}]$$

$$D_* = \frac{f_0^2}{g'}\int_0^{L_x} \overline{\psi}_{*1}\overline{\psi}_{*3,x}\, dx$$

(cont.)

(cont.)

$$D' = \frac{f_0^2}{g'} \int_0^{L_x} \overline{\psi_1' \psi_{3,x}'}\, dx$$

$$E = f_0 \int_0^{L_x} \overline{\psi}_3 B_x \, dx \tag{19}$$

In this budget there are contributions from the forcing, the frictional mechanisms, Reynolds' stresses due to both the standing and transient eddies (B_i and C_i), a zonal pressure gradient ($\mathcal{P}_i$), and pressure drag forces at the interface (D_* and D') and the bottom (E). The zonal pressure gradients involve the first correction to the mean pressure in a Rossby number expansion $\overline{p}_i^{(1)}$; hence, they are incalculable from our model equations (1)–(4). In the gap, however, the assumption of zonal periodicity implies $\mathcal{P}_i \equiv 0$. It is only there that the budget (18) will be examined. One can see that D_*, D', and E are all pressure drags by rewriting them as follows:

$$D_* = -\int_0^{L_x} [f_0 \overline{\psi}_{*1}] \frac{\partial}{\partial x}\left[H_1 + \frac{f_0}{g'}(\overline{\psi}_1 - \overline{\psi}_3)\right] dx$$

$$D' = -\int_0^{L_x} \overline{[f_0 \psi_1'] \frac{\partial}{\partial x}\left[H_1 + \frac{f_0}{g'}(\psi_1' - \psi_3')\right]}\, dx \tag{20}$$

$$E = -\int_0^{L_x} [f_0 \overline{\psi}_3] \frac{\partial}{\partial x} [H_3 - B]\, dx$$

In each case in (20), there is an integral of the product of a pressure (equal to f_0 times a streamfunction to leading order) and the spatial gradient of a change in layer thickness (equal to minus the projection into the fluid of the region exterior to it). They are thus of the form:

$$\int \overline{p \hat{e}_z \cdot \underset{\sim}{ds}}$$

where $\underset{\sim}{ds}$ is the incremental vector arc length along a projecting surface and $\hat{e}_z$ is a unit vector aligned vertically. Such a term is a net zonal pressure force exerted by an obstacle, which we call a drag. In the case of D', the obstacle is the instantaneous interfacial height and the net drag is the time average of the instantaneous drag. The dynamic pressure drags D_* and D' are the only terms which represent momentum transfer vertically between the layers. They may be expressed in a number of alternative forms, including horizontal heat flux (see Appendix B). In the analyses below, we shall examine the first equation in (18) as well as the sum of both equations in (18). This latter is a budget for total zonal transport.

The following are budgets for the time and zonally averaged potential vorticities in each layer:

$$\begin{aligned} H_1^{-1}\,\overline{\frac{\partial}{\partial t}\langle q_1\rangle} &= H_1^{-1}\,\mathrm{curl}\,\overline{\underline{\tau}} - a_1 + b_1 + c_1 + d_1 + e_1 \\ H_3^{-1}\,\overline{\frac{\partial}{\partial t}\langle q_3\rangle} &= -\epsilon \int_0^{L_x} (\nabla^2\overline{\psi}_3 - a_3 + b_3 + c_3 + d_3 + e_3)\,\mathrm{d}z \\ &\quad - \frac{f_0}{H_3}\int_0^{L_x} J(\overline{\psi}_3, B)\,\mathrm{d}x \end{aligned} \tag{21}$$

Various source and sink terms in (21) are defined by:

$$\begin{aligned} a_i &= A_4 \int_0^{L_x} \nabla^6 \overline{\psi}_i \;\mathrm{d}x \\ b_i &= (-1)^{(i+1)/2} f_0^2/g' H_i \int J(\overline{\psi}_{*1}, \overline{\psi}_{*3}) \\ c_i &= -\int J(\overline{\psi}_{*i}, \nabla^2 \overline{\psi}_{*i}) \\ d_i &= (-1)^{(i+1)/2} f_0^2/g' H_i \int \overline{J(\psi_1', \psi_3')} \\ e_i &= -\int \overline{J(\psi_i', \nabla^2 \psi_i')} \end{aligned} \tag{22}$$

The preceding budgets are complicated. However, it will be shown that a few terms are frequently dominant (sections 5, 8, and 9) and that some terms in different budgets can be identified as alternative expressions of a single process (Appendix B).

3. THE SET OF ANTARCTIC CIRCUMPOLAR CURRENTS

As was discussed in the introduction, we shall not present a parameter study of the model defined by equations (1)–(4). Consequently, most of the parameters have unique values, which we simply list as follows:

$$\begin{array}{ll} L_y = 10^6\ \mathrm{m} & g' = 0.02\ \mathrm{m\ s^{-2}} \\ H_1 = 10^3\ \mathrm{m} & A_4 = 10^{10}\ \mathrm{m^4\ s^{-1}} \\ H_3 = 4\cdot 10^3\ \mathrm{m} & \epsilon = 10^{-7}\ \mathrm{s^{-1}} \\ f_0 = -1.1\cdot 10^{-4}\ \mathrm{s^{-1}} & y_S = 2.2\cdot 10^5\ \mathrm{m} \\ \beta = 1.4\cdot 10^{-11}\ \mathrm{s^{-1}\ m^{-1}} & y_N = 5.3\cdot 10^5\ \mathrm{m} \\ y_0 = 5\cdot 10^5\ \mathrm{m} & \Delta y_{\mathrm{gap}} = 3.1\cdot 10^5\ \mathrm{m} \end{array} \tag{23}$$

All of these parameters were defined in section 2, except for the gap width, $\Delta y_{\text{gap}} \equiv y_N - y_S$. Obviously, the y_S, y_N, and Δy_{gap} values in (23) do not apply to the channel case (where $y_S = 0$ and $y_N = L_y$).

The frictional parameters can be interpreted as spin-down times. Clearly, the dominant friction in this sense is the bottom drag, since $\epsilon^{-1} = 120$ days while $L_y^4 A_4^{-1} = 3 \cdot 10^6$ years. For currents with scales smaller than the basin width L_y, however, the decay rate for lateral friction is more rapid. The grid size for these calculations is $\Delta x = \Delta y = 19.6 \cdot 10^3$ m ($20.0 \cdot 10^3$ m for the channel); thus a resolution-scale spin-down time is $\Delta x^4 A_4^{-1} = 170$ days. The value of A_4 was chosen as small as was consistent with computational stability. The internal deformation radius:

$$r = \sqrt{g' H_1 H_3/(H_1 + H_3)}\, |f_0|^{-1}$$

is equal to 36 km from (23).[*] The time step for the computations was $\Delta t = 7.2 \cdot 10^3$ s. Brief comparison integrations were made with smaller Δt and larger A_4 values; no discernible changes occurred in the streamfunction patterns over a 100 day period.

The wind stress for all cases was assumed to be directed towards the east, with a maximum value in the center of the basin:

$$\underset{\sim}{\tau} = 10^{-4}\, f(t) \sin \frac{\pi y}{L_y}\, \hat{e}_x [\text{m}^2\ \text{s}^{-2}] \qquad (24)$$

This wind-stress amplitude is equivalent to 1 dyne cm^{-2}. In (24) there is time varying function f, which has a steady component plus a semi-annual oscillation with amplitude α (which is nonzero in two cases):

$$f(t) = 1 + \alpha \sin 2\pi (t/1.55 \cdot 10^7\ \text{s}) \qquad (25)$$

Van Loon (1971) has shown that an energetic semi-annual oscillation occurs in the Southern Hemisphere Westerly Wind latitudes.

The dominant topographic obstruction of the Antarctic Circumpolar Current occurs in the vicinity of the Drake Passage. Consequently, the idealized form which we shall use for $B(x, y)$ in one case is an elongated, Gaussian mound centered in the gap. It is defined by:

$$B(x, y) = B_0 B_1(x) B_2(y) \qquad (26)$$

where:

$$B_1(x) = \begin{cases} e^{-(x/\mathcal{L})^2} & \text{if } x \leqslant L_x/2 \\ e^{-(L_x - x)^2/\mathcal{L}^2} & \text{if } x \geqslant L_x/2 \end{cases} \qquad (27)$$

---

[*] This value may be somewhat larger than occurs in the Circumpolar Current. Baker et al. (1977) report a value of about 20 km as characteristic of NHf_0^{-1} in the top 1000 m in the Drake Passage (where N is the mean Vaisala frequency).

$$B_2(y) = \begin{cases} e^{-(y_S - y)^2/\mathcal{L}^2} & \text{if } y \leqslant y_S \\ 1 & \text{if } y_S \leqslant y \leqslant y_N \\ e^{-(y-y_N)^2/\mathcal{L}^2} & \text{if } y \geqslant y_N \end{cases} \tag{27}$$

B_0 is the topographic amplitude and $\mathcal{L}$ is the horizontal scale (chosen to be $1.5 \cdot 10^5$ m).

The several different cases for which numerical calculations were made are defined in Table I; henceforth, they will be referred to by their case labels. These six calculations allow an examination of the influences of the gap width, the zonal extent of the basin, the strength of the semi-annual oscillation in the wind forcing, and the topographic barrier in the gap. These cases were not selected so the solutions would be only slightly different from each other; our purpose was to expose qualitatively different flow regimes, if present. WW represents a mild exception to this criterion since its behavior proved to be close to that of LB; consequently, it will be discussed less extensively than SW. The value of B_0 in TB was chosen so that the topographic Rossby number $B_0 H_3^{-1}$ remained small enough to be quasigeostrophic, but large enough so that the lower layer f/(thickness) contours were closed in the neighborhood of the least depth; a sufficient condition for assuring this is:

$$B_0 > \frac{\beta y_0 H_3}{f_0} \tag{28}$$

From (23), the right-hand side of (28) is 400 m. Thus the value of B_0 = 500 m in Table I does satisfy (28). However, it is considerably smaller than the O(2000 m) value which occurs near the Drake Passage.

The numerical solutions will all be analyzed as if the initial conditions were irrelevant. This approach is appropriate to a turbulent flow characterized by a limited period of predictability. Therefore, only periods of statistical equilibrium for the solutions will be presented (see Table I). Our criterion for identifying these equilibrium periods is a reasonably crude one; namely, we require that there be no apparent trends in the gross statistics of the solutions (primarily gap transports and volume averaged energies).

The analyses which folow are lengthy and detailed; we feel that the partial insights provided by many different types of description are necessary for exposing the nature of these numerical solutions. The six cases listed in Table I are analyzed in parallel so that their sometimes unfamiliar characteristics can be interpreted at least by mutual contrast. It will perhaps be useful in reading these descriptions to think of LB as the parametrically central case for this study, CH as the simplest and most fundamental case, and TB as the most complex but probably most realistic; we shall elaborate upon these characterizations in section 12.

The following is a brief guide to the topics discussed. Firstly, in section 4 we present qualitative descriptions of the streamfunction and velocity fields,

TABLE I

The Antarctic Circumpolar Currents

Case label	Case name	L_x (10^6 m)	Δy_{gap} (10^6 m)	α	B_0 (m)	Analyzed equilibrium period (in days since initialization)	Initial conditions (at day 0)
CH	Channel Flow	1	1.0	0	0	800—2160	the middle $(10^6\ \text{m})^2$ from end state of SW, with periodicity imposed
SB	Small Basin	1	0.3	0	0	702—2250	end state of a computationally erroneous version of this case *
LB	Large Basin	2	0.3	0	0	202—1440	end state of a computationally erroneous version of this case *
WW	Weak Transient Winds	2	0.3	0.33	0	0—1440	end state of LB
SW	Strong Transient Winds	2	0.3	0.67	0	0—1440	end state of WW
TB	Topographic Barrier	2	0.3	0	500	1080—4320	end state of LB

* The error was a misapplication of the conditions (4).

both instantaneously and with time and zonal averages. Section 5 presents the volume averaged energetics of the solutions. Energy time sequences provide both an integral measure of the variability of the solutions and a basis for defining the periods of statistical equilibrium. Two energy budgets are examined: one partitioned into time mean and transient eddy components and another with the time mean partitioned into zonal mean and standing eddy components. Time sequences of volume transports through the gap are presented in section 6. Aspects of the transient eddies are described in section 7: time sequences at fixed locations, spectra, propagation characteristics, and principal components of the variability. Section 8 presents time and zonal averaged momentum budgets. In section 9, similar potential vorticity budgets are examined, along with scatter plots which expose the validity of $\overline{q}_i(\psi_i)$ functional relationships (these are the general solutions of steady, inviscid, unforced fluid motions). A linearized stability analysis of the mean jet for CH is presented in section 10. In addition, an assessment is made of several, previously proposed eddy heat flux parameterizations. A discussion of previous theoretical calculations for the Antarctic Circumpolar Current is given in section 11, and a summary of results is made in section 12.

4. STREAMFUNCTION AND VELOCITY CHARACTERISTICS

Fig. 1 shows typical instantaneous streamfunction patterns during the equilibrium periods defined in Table I. All cases are included except for WW which is quite similar in character to LB. Three types of patterns are shown: ψ_1, ψ_3, and $\psi_3 - \psi_1$ [which is proportional to the vertical displacement of the interface, $d = f_0/g'(\psi_3 - \psi_1)$].

These figures illustrate the qualitative character of the flows. In all cases there is a discernible, essentially zonal jet, but one which is disrupted by eddies and meanders. The jet is broadest and its transport (the increment in $H_i\psi_i$ across the jet) is greatest in CH, where there are no zonal obstacles. The transport is least and the eddy disruption greatest in TB, where there are both partial zonal walls and a topographic barrier in the gap.

The eddies have relatively large scales, typically on the order of 100—200 km (wavelengths of 400—800 km). It is uncommon for the eddies to have scales this much larger than r (=36 km here), either in subtropical gyre observations (McWilliams, 1976a) or closed basin numerical solutions (Holland and Lin, 1975a). The eddy scales here seem similar to that of the horizontal shear of the zonal jet, which itself is broader than closed basin jets. The broadest scales are evident in the lower layer, the narrowest in the interfacial displacements. The patterns are approximately equivalent barotropic; that is, the flows in the two layers have nearly the same configurations, but differ in their strengths (the upper layer velocities are stronger than the lower ones). The greatest departure from this approximation is shown in TB; there, ψ_3 is almost entirely a pattern of eddies, while ψ_1 exhibits some features of a meandering jet. The smallest eddy scales are also found in TB.

The mean states of the various numerical solutions are shown in Fig. 2.

The time averages are stable ones here; in all cases an average over half the equilibrium period is only slightly different from the average over the whole period. The patterns in $\overline{\psi}_1$ and $\overline{\psi}_3$ are those of zonal jets, broader in the mean than instantaneously, with reasonably zonally uniform meanders. The latter are most clearly seen as standing eddies in $\overline{\psi}_{*1}$. The standing eddies are weakest in CH (because of the invariance of the geometry with respect to arbitrary zonal translations); they have virtually identical horizontal scale and are zonally uniform in SB, LB, and SW; and they are zonally inhomogeneous in TB (they are strongest immediately downstream of the topography). TB also has something of the character of closed gyres in the mean, with a counterclockwise one to the north and a clockwise one to the south. These gyres rotate in directions corresponding to Sverdrup balances, driven by the local curl of the wind stress (positive in the north, negative in the south). Finally, we note that the regions where the streamfunction gradients are largest seem to be slightly narrower in the upper layer than in the lower layer.

This is further illustrated in Fig. 3, which contains plots of $\langle \overline{u}_i \rangle$ against y. In all cases the upper layer jet is stronger than the lower one. Its strength is greatest in CH and least in TB. There is an intermediate hierarchy of jet strengths — with SB, LB, SW an increasing sequence — although the differences are not great here. The clear suggestion, however, is that both zonal walls and topographic barriers impede the jet, and that the lesser influences of increased basin extent L_x and a pulsating forcing by the wind transience tend to increase the jet strength.

It is apparent from comparing Figs. 1 and 2 that transient eddies are a significant component of the numerical solutions. The upper layer streamfunction variance patterns are shown in Fig. 4. The eddy variability is strongly concentrated in the locations of the mean jet (compare with $\overline{\psi}_1$ in Fig. 2) and shows a further enhancement in the locations of the centers of the mean standing eddies (compare with $\overline{\psi}_{*1}$ in Fig. 2). This latter suggests that some of the transience is associated with non-propagating oscillations in the amplitudes of the instantaneous standing eddies. The spatial envelope of the variability is not much greater in extent than the size of the individual eddies shown in Fig. 1. The order of the cases, from greatest eddy variance to least, is given by SW, LB, SB, CH, and TB with, respectively, peak r.m.s. values of 5.8, 5.3, 4.2, 4.2, and $2.8 \cdot 10^4$ m^2 s^{-1}. There is somewhat less range here than there was in the strength of the mean jets (Fig. 3). Furthermore, the orders are not identical (CH is displaced from first in jet strength to fourth in eddy intensity), thus belying any exact correspondence between these two quantities. The patterns for $\overline{\psi_3'^2}$ (not shown) are similar to those for $\overline{\psi_1'^2}$, though typically they have magnitudes which are only 0.2—0.4 as large. The patterns for velocity variances, $\overline{u_i'^2}$ and $\overline{v_i'^2}$, also have their maxima in the neighborhoods of the mean jets. In addition, they show local maxima on the flanks of the standing eddies and either near the interior edges of the gap (for $\overline{u'^2}$) or along the partial zonal walls (for $\overline{v'^2}$).

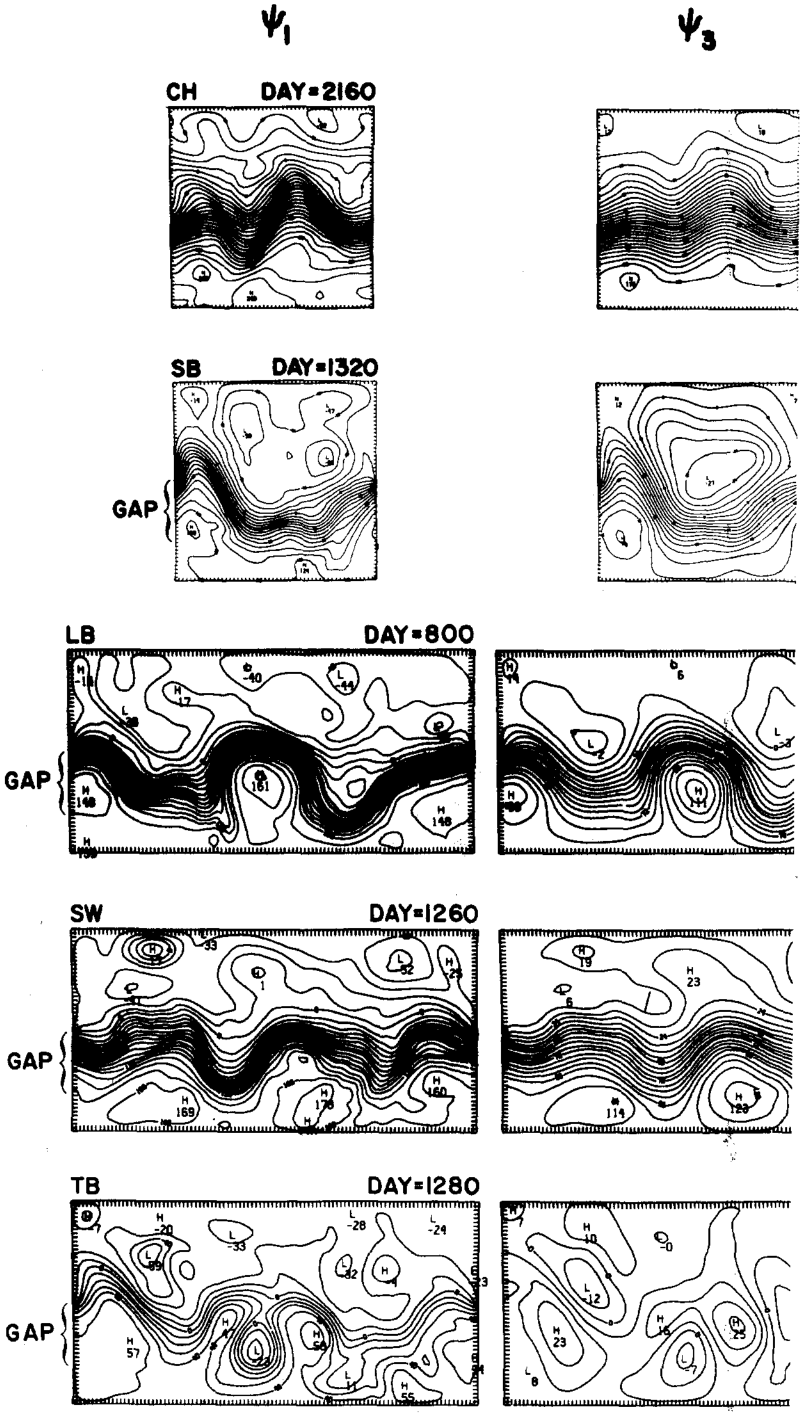

Fig. 1. Instantaneous streamfunction patterns on selected days during the
each case are the upper and lower streamfunctions and their difference, w
yields the interfacial displacement. The contour intervals are 10^4 m^2 s^{-1}
in units of 10^3 m^2 s^{-1}. The range of ψ values in each of these figures (fro
105, 108, 205, 116, 103, 230, 126, 116, 117, 37, and 104 · 10^3 m^2 s^{-1},

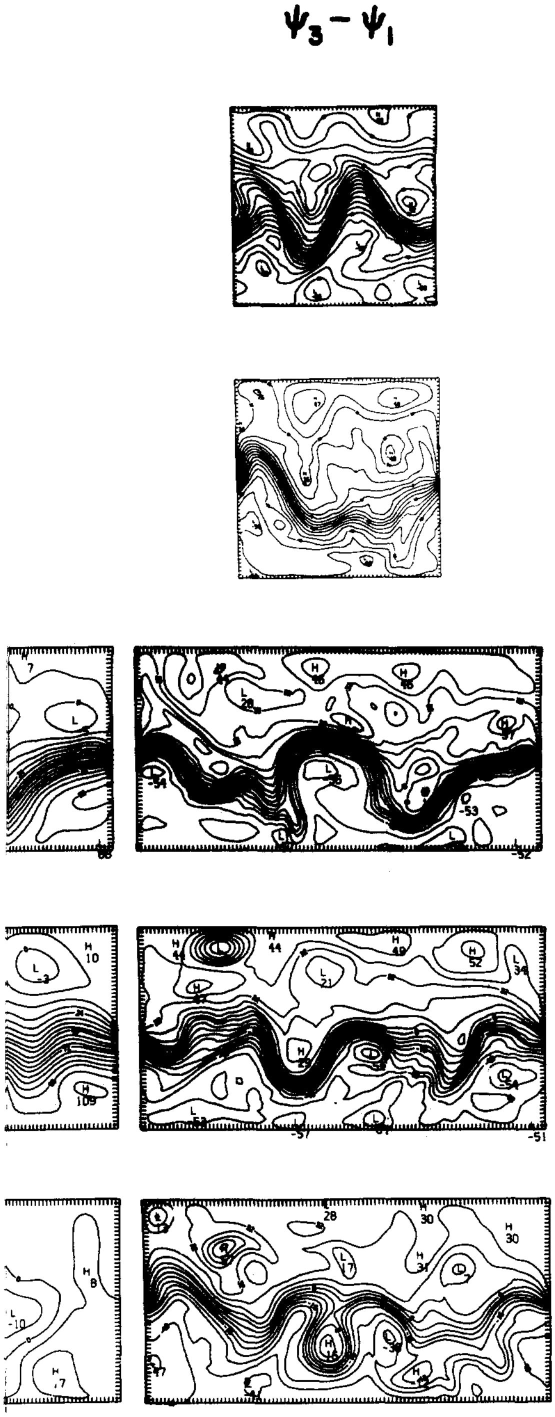

$\psi_3 - \psi_1$

equilibrium periods for the different cases. Shown for
hich, when multiplied by $f_0/g' = -0.55 \cdot 10^{-2}$ s m^{-1},
for ψ_1 and $0.6 \cdot 10^3$ m^2 s^{-1} for $\psi_3 - \psi_1$; the labels are
m left to right, top to bottom) is 292, 165, 132, 199,
espectively.

m^2

-1,

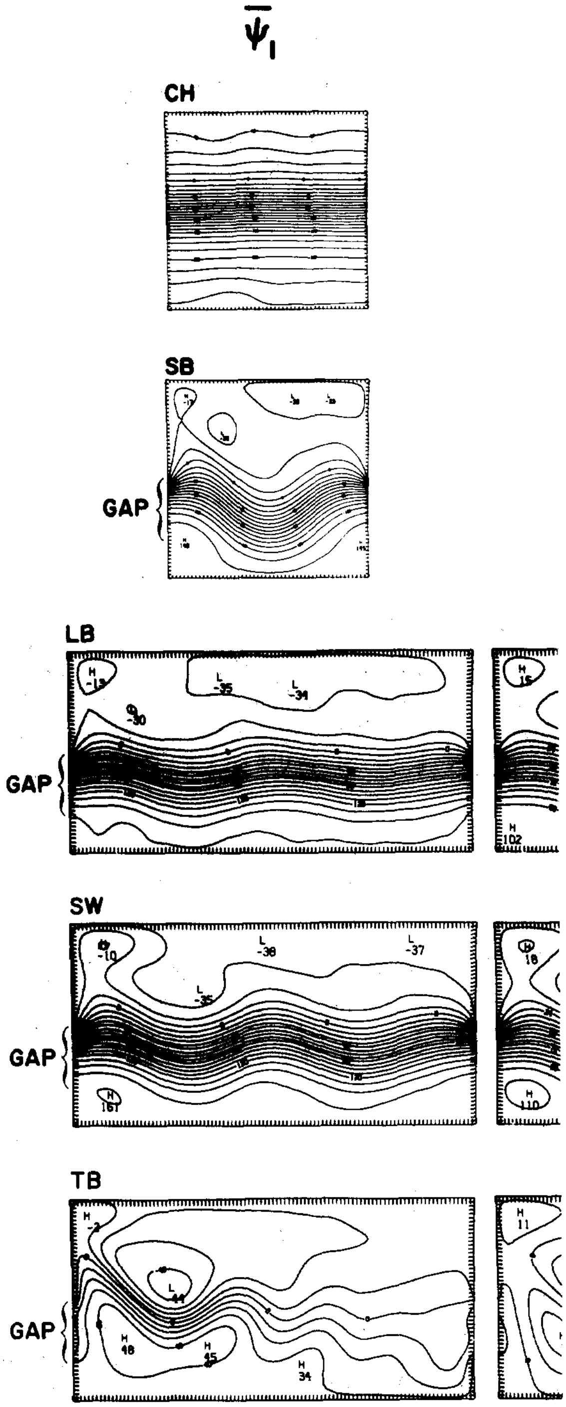

Fig. 2. Time averaged streamfunction patterns (the s^{-1} for ψ_1 and $0.6 \cdot 10^4 \mathrm{m}^2 \mathrm{s}^{-1}$ for ψ_3 and ψ_{*1}; th figures (from left to right, top to bottom) is 277, 1 respectively.

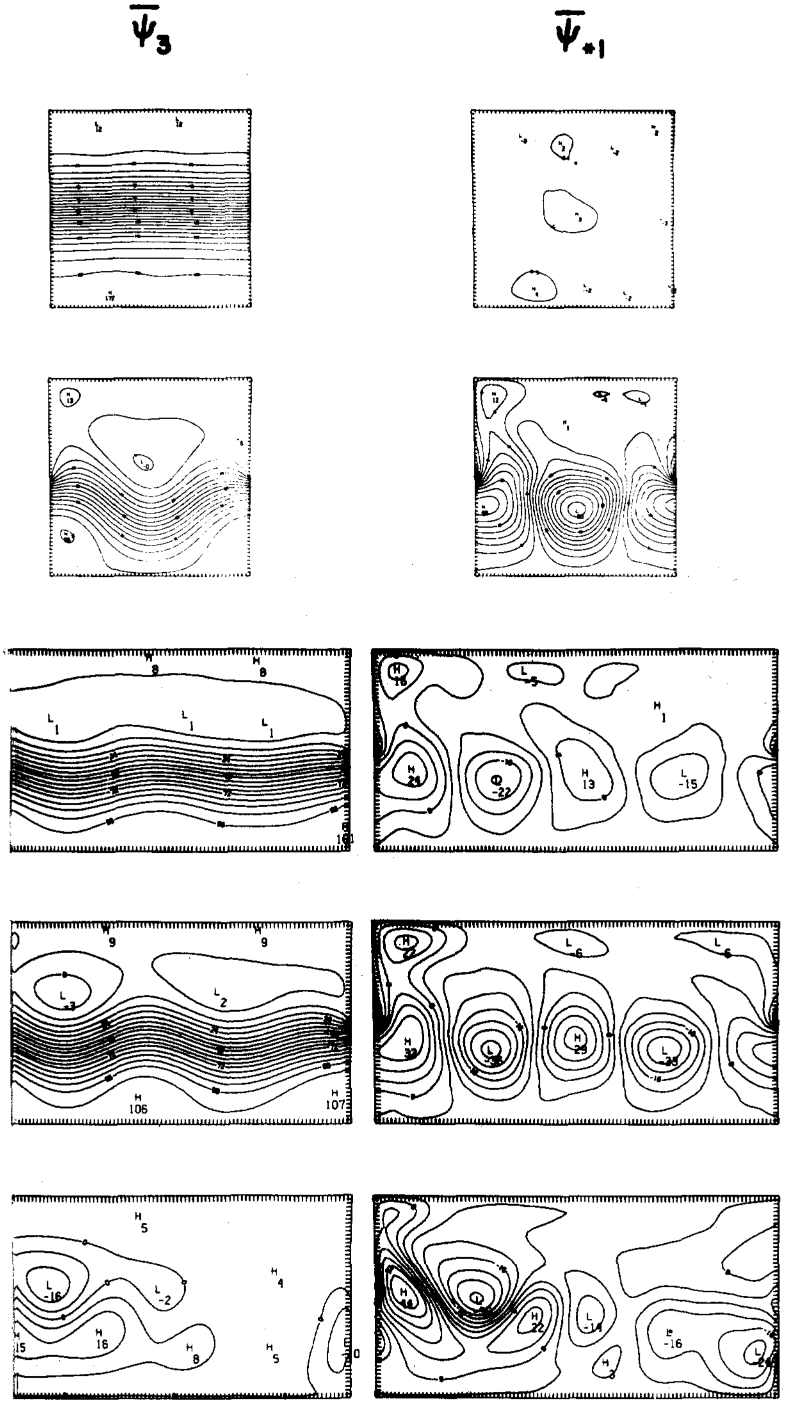

averaging intervals are defined in Table I). The contour intervals are 10^4 m^2
labels are in units of 10^3 m^2 s^{-1}. The range of ψ values in each of these
0, 179, 96, 108, 187, 101, 46, 199, 113, 68, 92, 32, and 79 $\cdot$ 10^3 m^2 s^{-1},

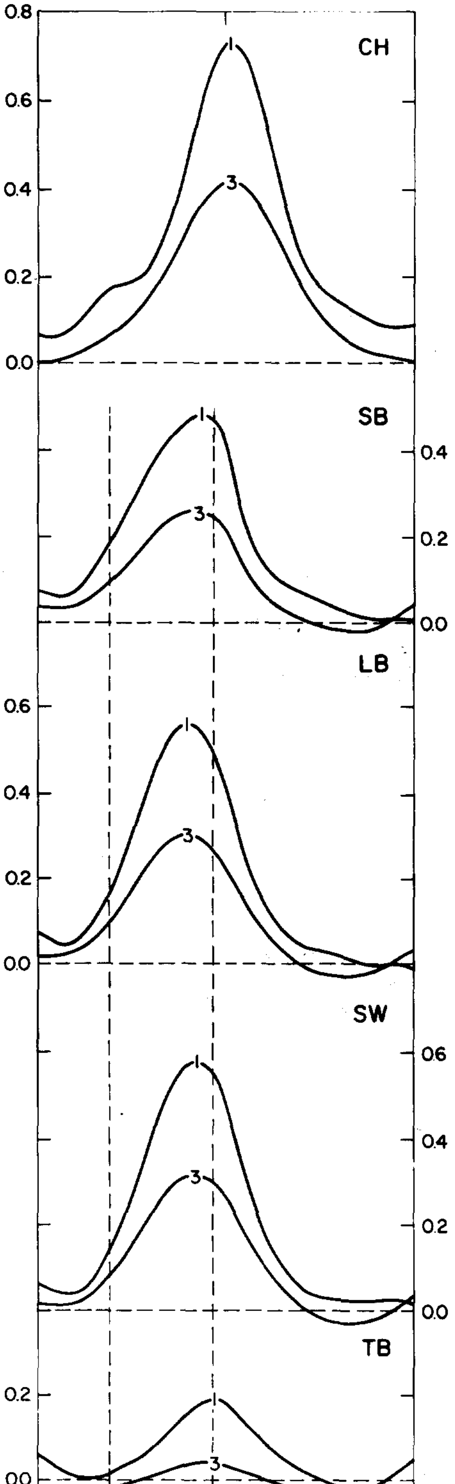

Fig. 3. The zonal means of the zonal velocities $\langle\bar{u}_i\rangle$ (m s^{-1}) for the equilibrium periods in Table I.

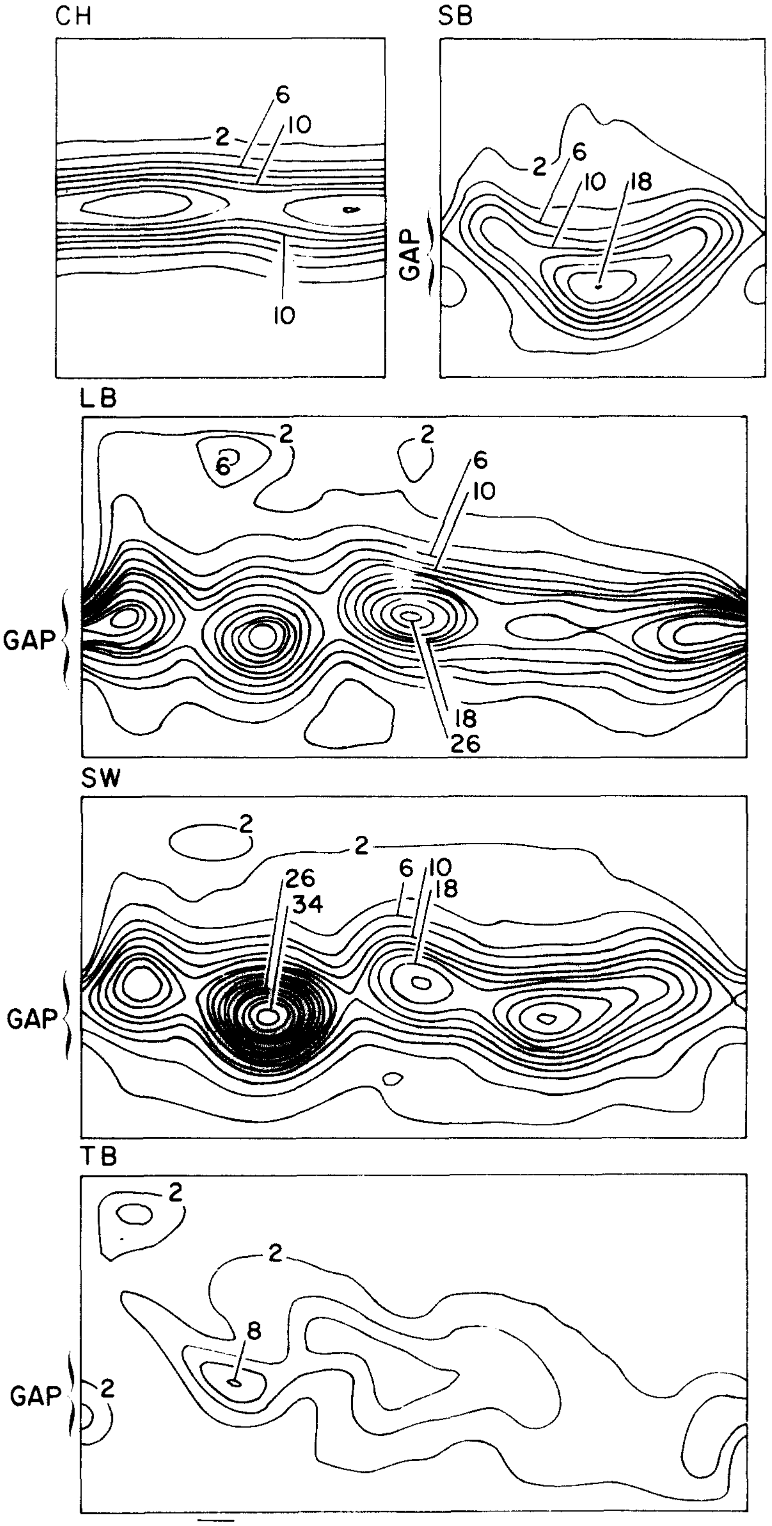

Fig. 4. Patterns of $\overline{\psi_1'^2}$ for the equilibrium periods of Table I. The contour interval is $2 \cdot 10^8$ m^4 s^{-2} and labels are in units of 10^8 m^4 s^{-2}.

5. ENERGETICS

One of the most useful gross measures of the numerical solution behavior is the time history of the depth integrated and area averaged energies. We define these energies analogously to equation (6),

$$\begin{aligned} \mathcal{K}_i &\equiv \tfrac{1}{2}H_i \iint_{\Omega} \nabla\psi_i \cdot \nabla\psi_i \, \mathrm{d}x \, \mathrm{d}y \qquad (i = 1, 3) \\ \mathcal{P} &\equiv \tfrac{1}{2} f_0^2/g' \iint_{\Omega} (\psi_1 - \psi_3)^2 \, \mathrm{d}x \, \mathrm{d}y \end{aligned} \tag{29}$$

Plots of $\mathcal{K}_i$ and $\mathcal{P}$ are shown in Fig. 5 for all cases except WW.

Generally, the fluctuations of these curves are not large compared to their mean values. The kinetic energies in the two layers are correlated in time and have nearly equal magnitudes (though $\mathcal{K}_3 > \mathcal{K}_1$ in CH and $\mathcal{K}_1 > \mathcal{K}_3$ in TB). The potential energy exceeds the kinetic energies; this is to be expected, simply by a scale analysis of (29), for currents whose dominant horizontal scale exceeds the deformation radius r. There appears to be a generally weaker correlation between $\mathcal{P}$ and the $\mathcal{K}_i$ (compared with $\mathcal{K}_1$ and $\mathcal{K}_3$); where the bottom is flat (in CH, SB, and LB) or the oscillations are forced (in SW), there is no phase lag, but the $\mathcal{K}_i$ follow $\mathcal{P}$ in TB.

The initial periods of the integration are not of fundamental interest since the initial conditions are somewhat arbitrary (see Table I). Fig. 5 does, however, provide a basis for judging the correctness of the equilibrium periods defined in Table I. In two cases, CH and TB, there are significant initial adjustment periods shown prior to the equilibrium periods.

The equilibrium time scales in CH seem to be slightly larger than in SB and LB; for none of these cases does there appear to be any particular regularity (i.e., no vacillation cycles as in Hart, 1976).* The strongest transience in SW is clearly correlated with that of the wind. From (24)—(25), we note that the wind maxima occur at day 90 and every 180 days thereafter; it is remarkable how little phase lag there is in the total energy response. A very dramatic and regular natural oscillation is shown for TB. Its period is of the order of three years, and its amplitude in energy is 50% of the mean value. This oscillation cannot be simply interpreted as a topographic wave because the periods are too dissimilar (n.b., the topographic wave period should be of the order of $2\pi |H/f_0 B_0| \approx 7$ days). No satisfactory explanation has been found, though the associated spatial structure is shown in section 7.

Comparable time series for the instantaneous transient eddy energies are

---

* It is of interest that the mean energy balances in the two-layer stress-driven annulus studies of Hart (1976) are quite similar to ours (see Figs. 7—8) in spite of the differences in eddy structures. The most important difference between his circumstances and ours is our relatively much weaker interior friction, the essential consequence of which is that our flows are intrinsically aperiodic.

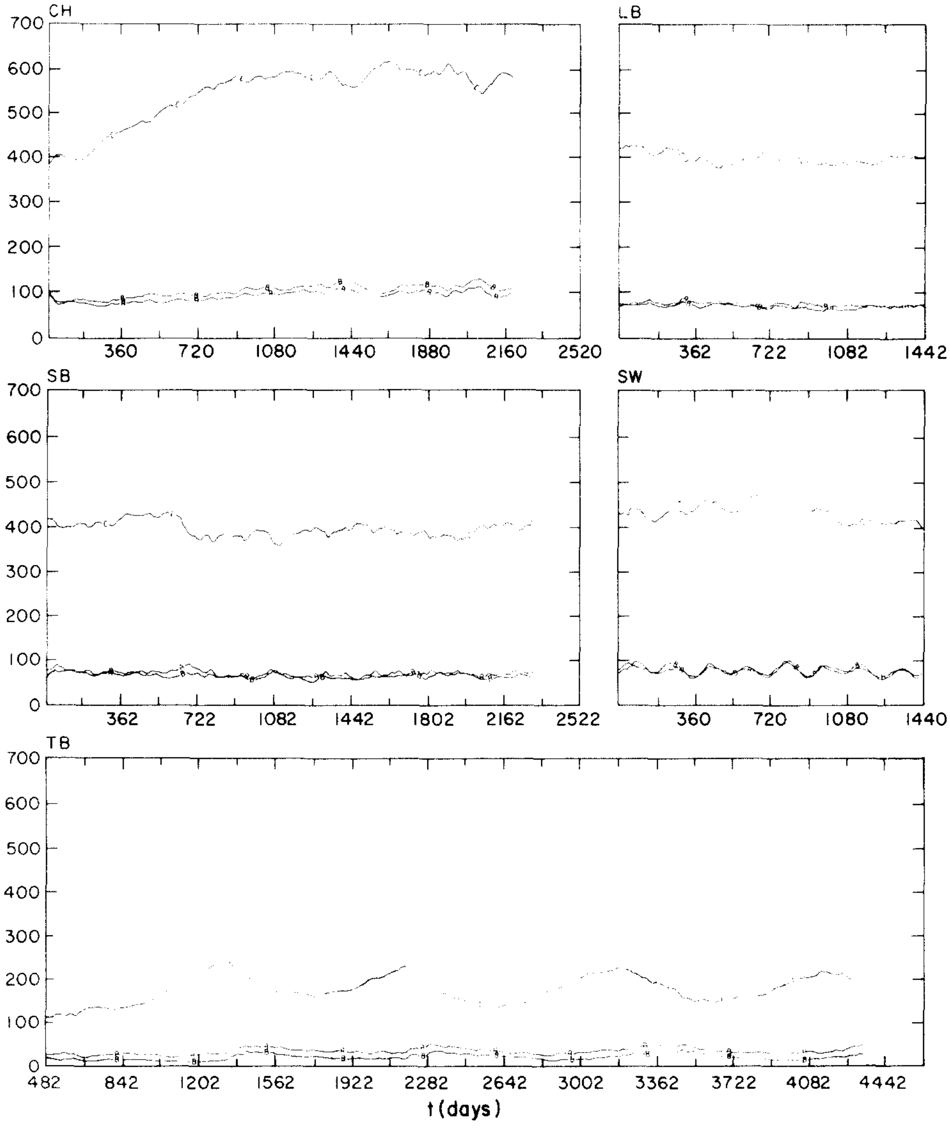

Fig. 5. The time histories of the total energies defined in eq. (29). The units are $m^3 s^{-2}$. The labels for the three curves in each case indicate upper layer kinetic (A), lower layer kinetic (B), and potential (C) energies.

shown in Fig. 6. These quantities are defined by:

$$\begin{aligned} \mathcal{K}_i' &= \tfrac{1}{2}H_i \iint_{\Omega} \nabla \psi_i' \cdot \nabla \psi_i' \\ \mathcal{P}' &= \tfrac{1}{2}f_0^2/g' \iint (\psi_1' - \psi_3')^2 \end{aligned} \qquad (30)$$

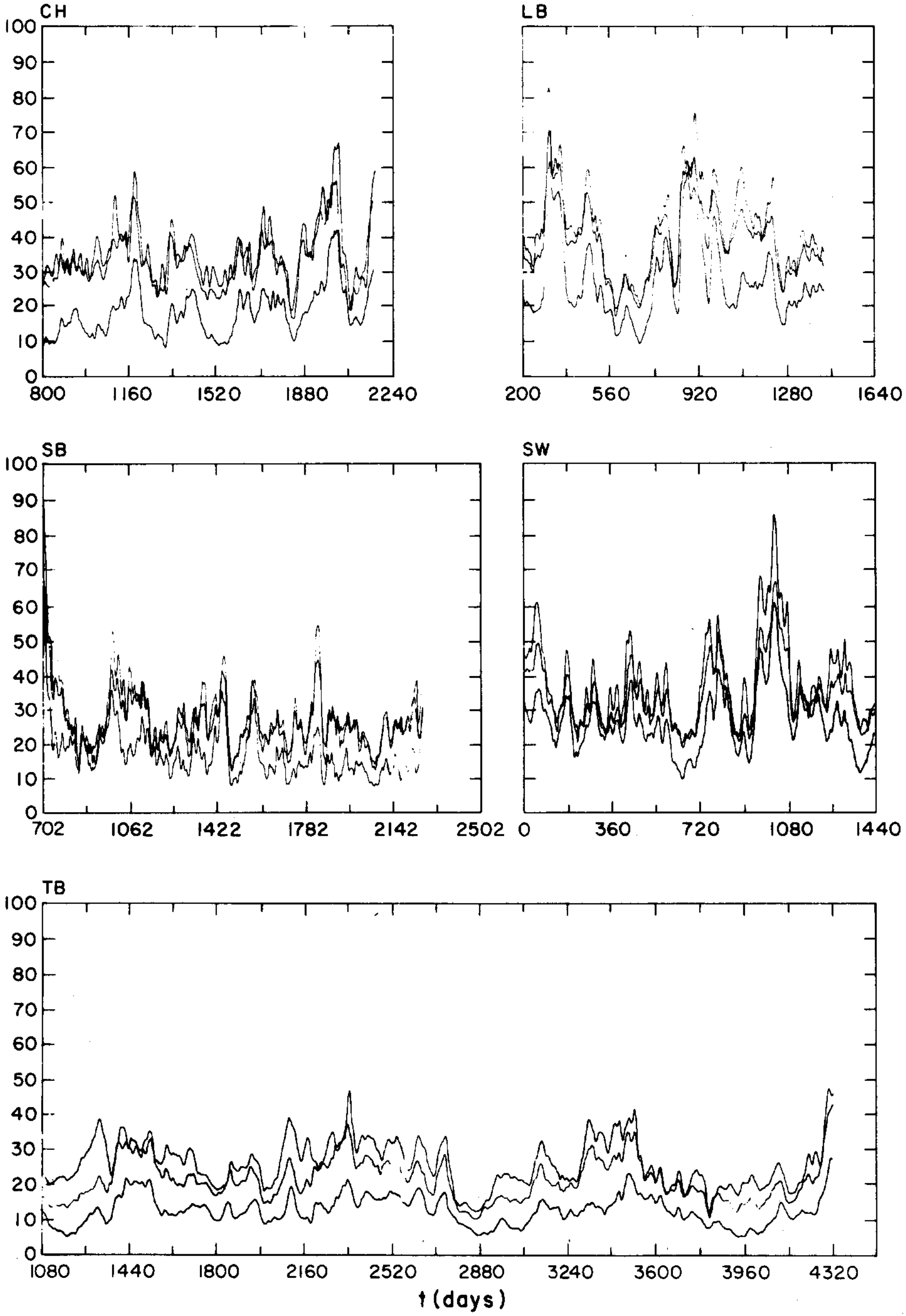

Fig. 6. The time histories of eddy energies during the equilibrium periods defined in Table I. The units are $m^3 s^{-2}$. On the average, $\mathcal{P}' > \mathcal{K}'_1 > \mathcal{K}'_3$, though instantaneously there are exceptions.

The fractional variation exhibited in these curves is considerably greater than those in Fig. 5, but their mean values are also much smaller. The $\mathcal{P}'$ and $\mathcal{K}'_1$ values are quite similar here, while the $\mathcal{K}'_3$ values are smaller; this was not true for the total energies (29). All of the eddy energies are mutually correlated.

There is quite a dramatic peak in the SB eddy energies near day 700, which, for example, reaches a value in $\mathcal{K}'_1$ more than four times larger than $\overline{\mathcal{K}'_1}$ (equal to $K'_1 = 26\ \text{m}^3\ \text{s}^{-2}$). This eddy energy peak is not associated with any peak in total energy (see Fig. 5). Rather it occurs because of a shift in the location of the eddy centers from their more usual locations near the standing eddy centers (see Fig. 2).

The periodicity in TB, seen above in Fig. 5, is also reflected in the eddy energies. In addition, irregularly spaced, shorter period fluctuations are evident. It is interesting, however, that the wind-induced periodicity in SW, which was seen so clearly in the total energies, is much less noticeable in the eddy energies. This is the first of several indications that even a strongly fluctuating wind (with peak-to-peak amplitude 4/3 times the mean) causes ocean responses which can be small compared to the natural variability or intrinsic turbulence of the fluid.

The energy budgets (7) and (14) are shown in Figs. 7 and 8 respectively. We shall discuss the different cases in turn. For CH, the energy input by the wind is transferred from K_1 to P. It then partly goes to either P' or K_3 (and then is lost to bottom friction). The eddy energy is thus generated by a baroclinic instability of the mean flow (defined by $\{P, P'\} > 0$ being the dominant mean-to-eddy energy transfer). The eddy energy is transferred from P' to either K'_3 (then lost to bottom friction) or to K'_1, where most of it is returned to the mean flow (a reverse instability) and a small fraction is lost to lateral friction. This latter transfer, $\{K'_1, A_4\}$, is typically the only lateral frictional transfer term which is non-zero when rounded off to the nearest $0.1 \cdot 10^{-5}\ \text{m}^3\text{s}^{-3}$. Even this magnitude is much smaller than the bottom frictional energy losses. The standing eddy budget (Fig. 8) is trivial for CH since the $\overline{\psi}_{*i}$ are so weak.

The eddy-mean budget for SB is qualitatively quite similar to CH. The only differences are generally lower values for energies and transfer rates and the appearance of a small reverse instability in the lower layer as well (i.e., $\{K'_3, K_3\} > 0$). In this case, however, the standing eddies play an active role in the mean budget (Fig. 8). They provide 25% of baroclinic instability conversion to the eddies and receive 50% of the upper layer reverse instability. Their primary source is a barotropic instability of the mean zonal jet in both layers (i.e., $\{K_{*i}, K_{zi}\} < 0$); note that this instability is a conversion of energy to a non-propagating current pattern. The bottom frictional loss from the standing eddies is 2/3 that from the mean zonal jet.

The mean-eddy budget for LB also conforms to the pattern of SB and CH. The standing eddy budget for LB is like that of SB as well, except that the standing eddies are much weaker in LB (see Fig. 2), and thus their energy

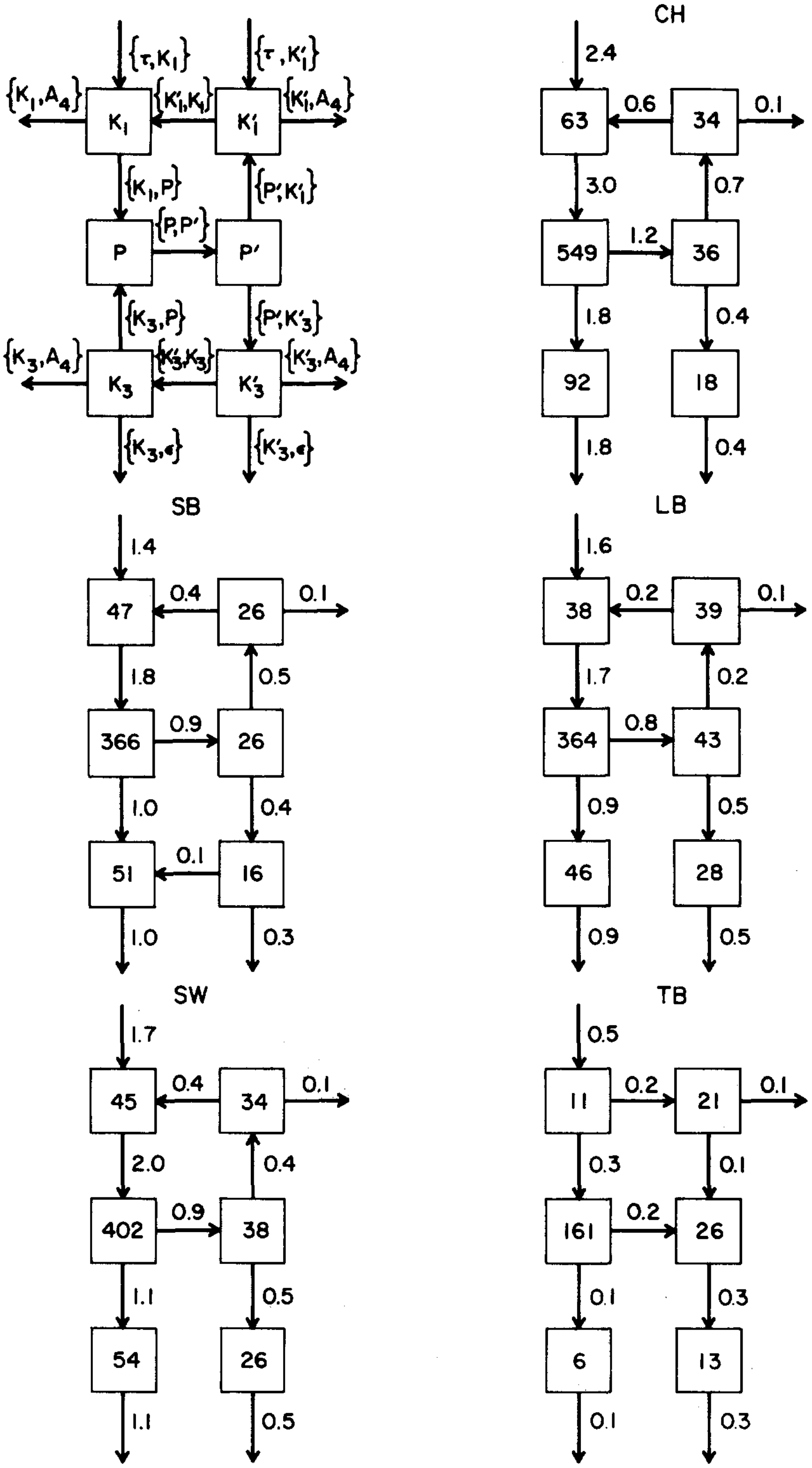

Fig. 7. A diagram of the budget (7) for mean and eddy energies. The diagram is defined in the upper left panel. The units for the energies are $m^3\ s^{-2}$, rounded to the nearest unit. Those for the transfer rates are $10^{-5}\ m^3\ s^{-3}$, rounded to the nearest 0.1 unit (zeroes have been deleted).

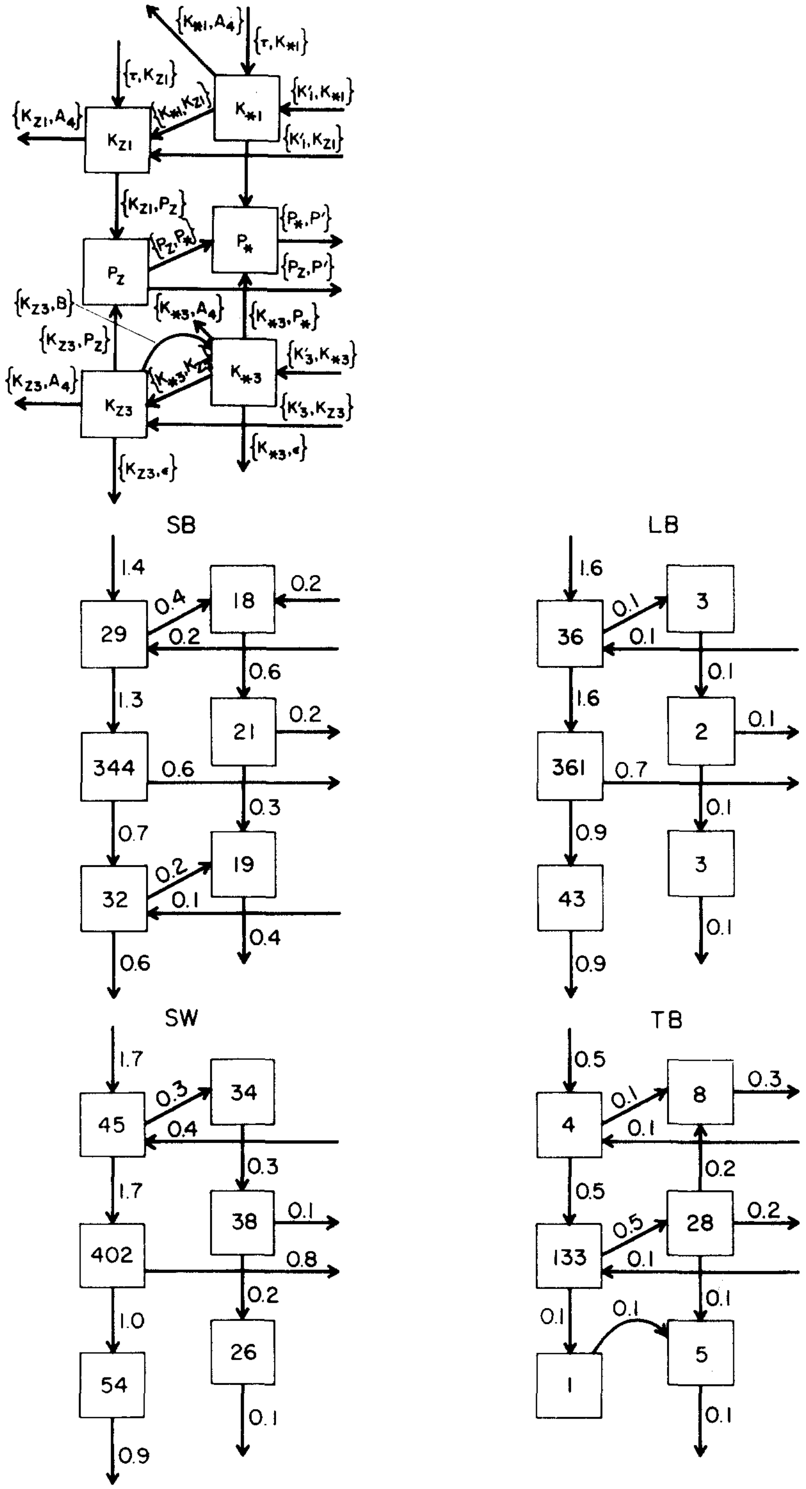

Fig. 8. A diagram of the budget (14) for zonal mean and standing eddy energies. The same conventions are used here as in Fig. 7. The budget for CH is deleted because its standing eddy energies are all less than 0.2 $m^3\ s^{-2}$.

transfer rates are weaker. However, the transient eddies in LB are more energetic than in SB. Thus, here, as well as in the other budgets below, there seems to be a compensation principle: as one process weakens another strengthens, so that the total budget quantity changes relatively little.

For SW, the mean-eddy budget is similar to the previous cases, and the standing eddy energies are even larger than in SB. Here, however, the standing eddy transfer rates are not quite as large as in SB. The most surprising feature is the absence of any significant work done on the fluid by the transient wind (n.b., $\{\tau, K_1'\} \approx 0.02 \cdot 10^{-5}$ m^3 s^{-3}). This implies an almost complete lack of correlation between the forcing and the response.

The most anomalous budgets are those of TB. In Fig. 7, the conversions from mean to eddy energy are, in equal measure, baroclinic and upper layer barotropic instabilities (i.e., $\{P, P'\} \approx -\{K_1', K_1\} > 0$). The eddy kinetic energies are larger than those of the mean flow, and the primary bottom frictional loss is through the eddies, which is in contrast to all previous cases. In Fig. 8, the standing eddy kinetic energies dominate the mean zonal ones, and the primary energy source for the $\overline{\psi}_{*i}$ is a baroclinic instability of the zonal mean flow. An upper layer barotropic instability and a topographic conversion provide lesser sources for standing eddy energy. All of the transient eddy exchanges with the zonal mean are reverse instabilities.

The general character of the eddy-mean budgets can be compared with those of the closed basin solutions of Holland (1977, 1978). The primary differences are the dominance in his case of upper layer barotropic instability as the eddy energy source and the relatively greater portion of the bottom frictional dissipation which occurs through the eddies. By these measures, then, TB is the case closest in behavior to a closed basin gyre. If one further splits the kinetic-potential energy transfer terms as indicated in (10), then all cases have systematic transfers from both K_i to P and from P' to both K_i'. In addition, $\{K_1 \hat{,} K_3\}$ is positive and $\{K'_1 \hat{,} K_3'\}$ negative. All of these features but the final one are true in the closed basin solutions as well; in barotropically unstable solutions, $\{K_1' \hat{,} K_3'\}$ is positive.

Bryden (1977) has estimated from moored observations the pointwise (rather than vertically integrated) rate of baroclinic energy conversion on the upstream side of the Drake Passage at a moderately deep level. He obtained a figure of about 10^{-8} m^2 s^{-3}, with a sign indicating conversion from the mean to the eddies (i.e., $\{P, P'\} > 0$). From (B.7) in Appendix B we can identify the (y, z) pointwise contribution to this conversion with $(\langle \overline{u_1} - \overline{u_3} \rangle) D'/(H_1 + H_3)$, if we disregard any ambiguities about energy fluxes, The $\langle \overline{u_i} \rangle$ are shown in Fig. 3, and the D' are plotted in Figs. 21—22. For the various cases, the peak value for this pointwise conversion varies from $1.1 \cdot 10^{-8}$ m^2 s^{-3} for CH to $0.8 \cdot 10^{-8}$ m^2 s^{-3} for LB to a small negative number for TB (n.b., in TB the primary baroclinic conversion is connected with the standing eddies — see Fig. 8 — with a pointwise conversion of $0.5 \cdot 10^{-8}$ m^2 s^{-3}). Thus, the numerical solutions exhibit conversions of the same order as the measurements. Considering the location of the measurements (i.e., at depth and near large topography) however, one might judge the model conversions as generally smaller.

6. TRANSPORTS

Much of the historical concern with the Antarctic Circumpolar Current has been focused on the volume transport through the Drake Passage. Fuel for controversy has been provided by the extremely diverse values which have been obtained by different investigators (Nowlin et al., 1977).

The volume transports through the gap are shown as functions of time in Fig. 9. For all cases except TB, the dominant contribution to the total transport comes from the lower layer. For all cases except CH, there is significant variability in the transport with periods from 10—200 days (and even longer for TB).* For all cases except TB, the total transports are excessive compared to observations (e.g., 400—600 Sv for SB, LB, and SW instead of the observed average values of 100—200 Sv). For TB, however, the total mean transport is less than 100 Sv, and the lower layer mean transport is slightly negative. The transport in SW is highly correlated with the wind transience with only a small phase lag (n.b., its correlated fluctuations are as large as 300 Sv peak-to-peak).

This figure suggests that the amount of variability in the transport, as well as the average value for it, are strong functions of all three influences — the constriction of the mean jet by the gap edges, the topography, and the variation in the wind forcing. Any precise simulation of the observed transport behavior is, therefore, likely to prove very difficult.

7. TRANSIENCE

The amount of data generated by a set of numerical solutions such as ours is vast. This becomes particularly apparent when attempting to describe the transient behavior of the solutions, which can be so varied in different quantities, at different locations, and during different intervals. Of necessity we can only present a few examples which seem to us to be representative. Four techniques are used: time sequences at a fixed location, spectra for those sequences, propagation diagrams (Hovmöller diagrams), and principal component plots and time sequences.

The case LB has been chosen to illustrate the geographical variations of the time sequences. A set of ψ' sequences are shown in Fig. 10, and a set of v' ones in Fig. 11. In Fig. 10, the most visually prominent fluctuation period in all cases is about 40—60 days. This period is not inconsistent with a mean jet advection period (n.b., $2\pi l/U$ matches this range of periods for $U = 0.3$ m s^{-1} and $l = 150$—250 km). Much longer periods are also apparent (particularly in the lower layer), as well as shorter ones (particularly in the center of

---

* CH is the only case in which all external conditions are independent of t and x.

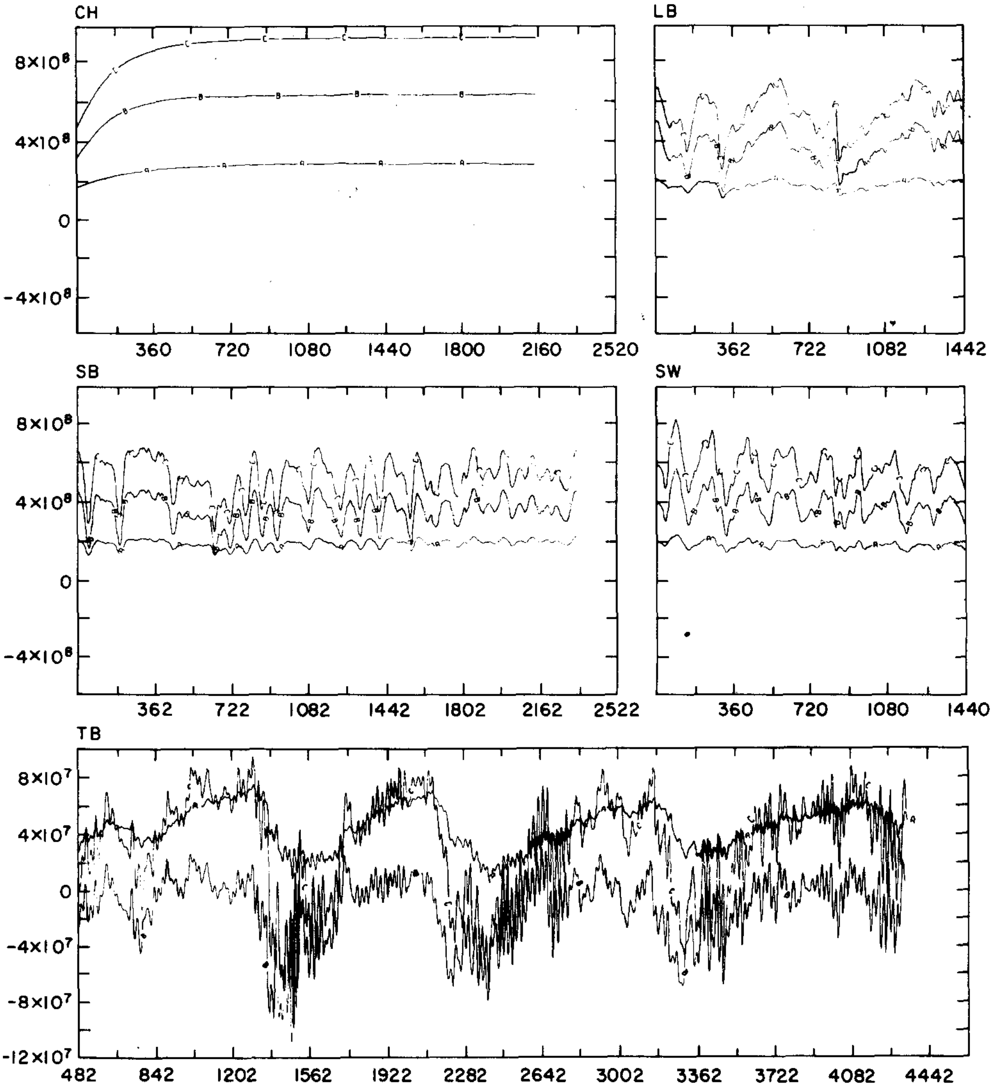

Fig. 9. The time histories of transport through the gap ($m^3 s^{-1}$). The three curves in each case are (a) upper layer $H_1(\psi_1(0) - \psi_1(L_y))$, (b) lower layer $H_3(\psi_3(0) - \psi_3(L_y))$, and (c) total transport. For TB only days 482—4320 are shown, since initial transients are off-scale for this graph (n.b. the scale for TB is different from the other cases).

the upper layer jet). There is an indication of non-stationarity in the contrast between the first and last halves of the record for $\psi_1'(980,451)$. The amplitude of the fluctuations is greatest in the center of the upper layer jet, somewhat smaller in the lower layer jet, and considerably smaller outside the jet.

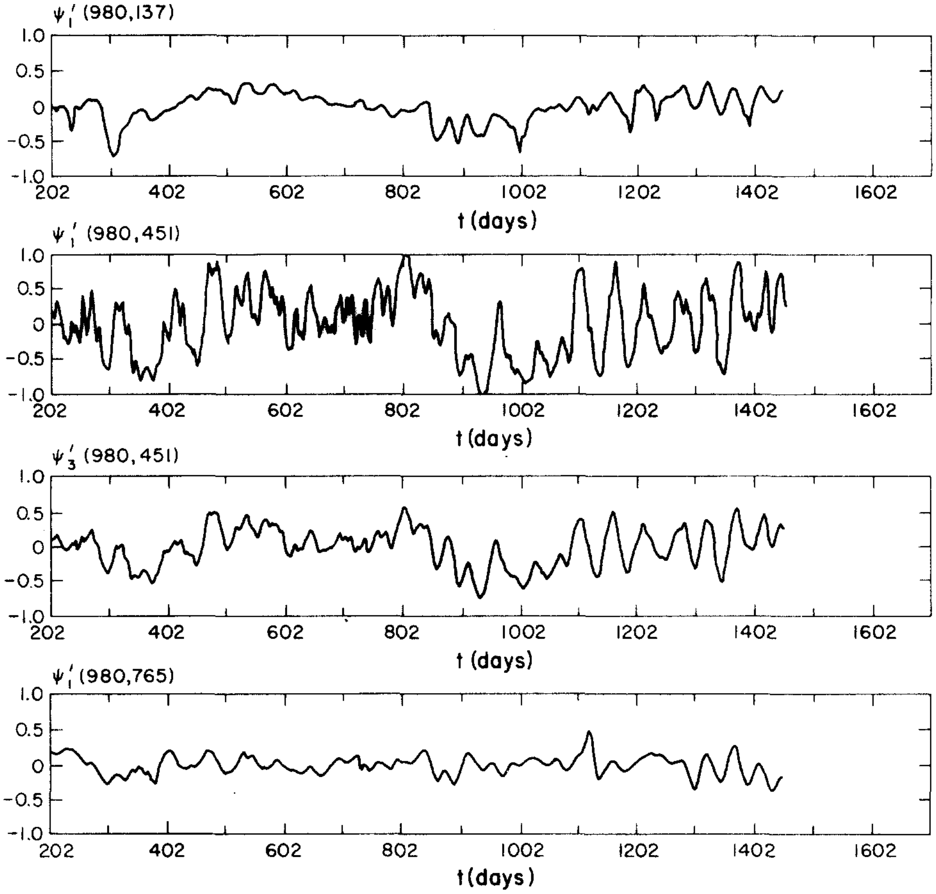

Fig. 10. Time series of the streamfunction at several locations in LB. Locations are indicated by the arguments (x, y) in km from the southwest-corner of the basin. Units are $10^5\ \mathrm{m^2\ s^{-1}}$.

The time scales for v are shorter than for ψ (Fig. 11), at least visually, with a dominant period of around 25 days. The same geographic tendencies occur here as before, however. Since $v = \psi_x$, the wavenumber spectrum for v would be peaked at a smaller scale than for ψ; hence, we would expect the fluctuation period for v to be shorter, if it were mainly caused by the advection of spatial structures by the mean jet. We shall not quantify this argument by exhibiting wavenumber spectra; in all cases except CH, the solutions are too spatially inhomogeneous for such spectra to be readily interpretable. The sequences in v at locations away from the mean jet exhibit a dramatic intermittence. Isolated, narrow (of only 5—10 days duration) velocity spikes occasionally occur.

There is also considerable variety in the time sequences of the different

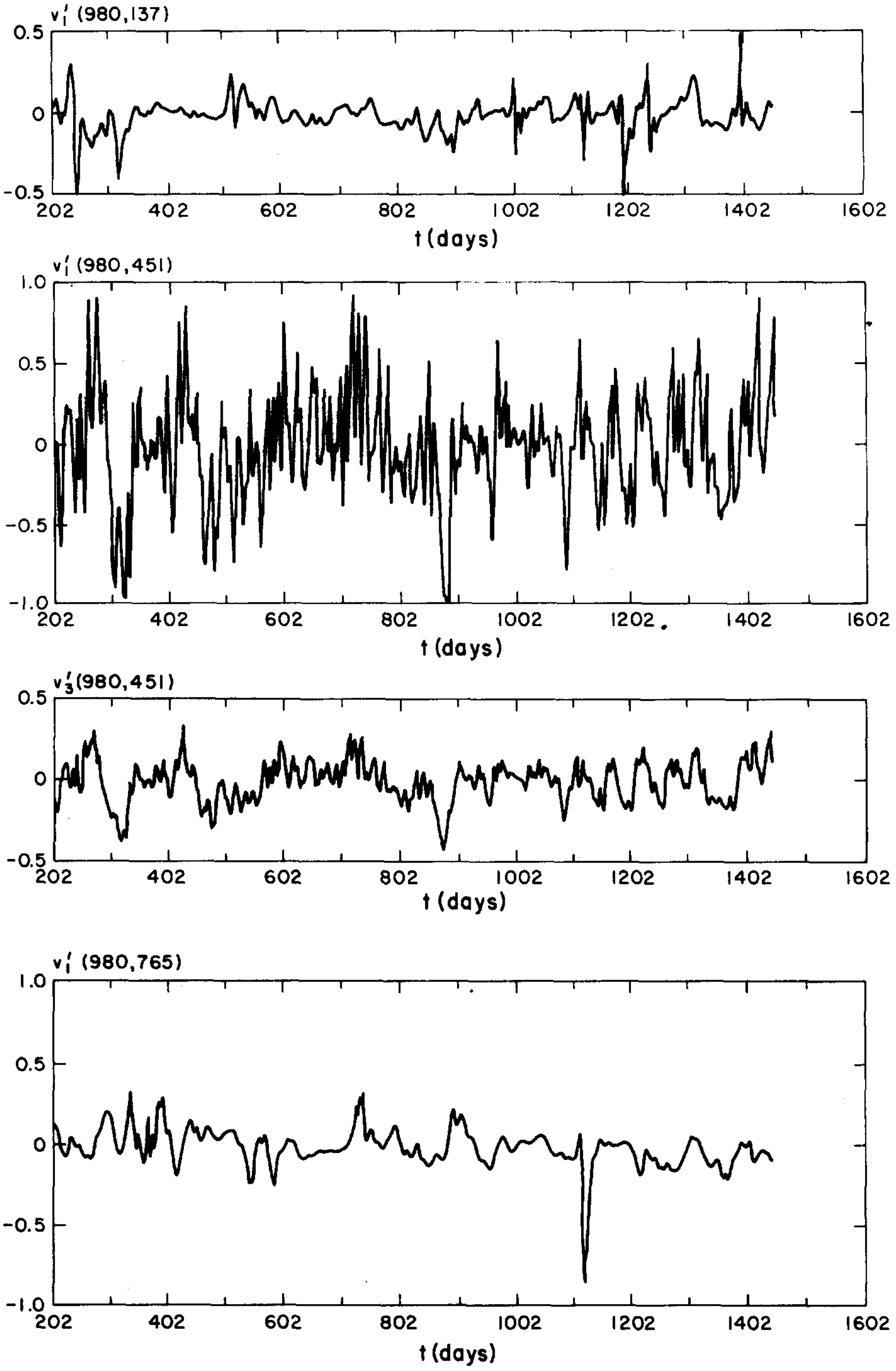

Fig. 11. Time series of the meridional velocity in LB (as in Fig. 10). Units are m s^{-1}.

numerical cases. Fig. 12 shows a set of sequences for ψ_1' near the center of the mean jet (the SB case is perhaps not as close as would be most desirable — compare the location $x = 490$ km, $y = 451$ km, with $\overline{\psi}_1$ in Fig. 2). The sequence from CH looks the least like those of Fig. 10. It seems to rather simply consist of two periods, one around 20 days and another around 200

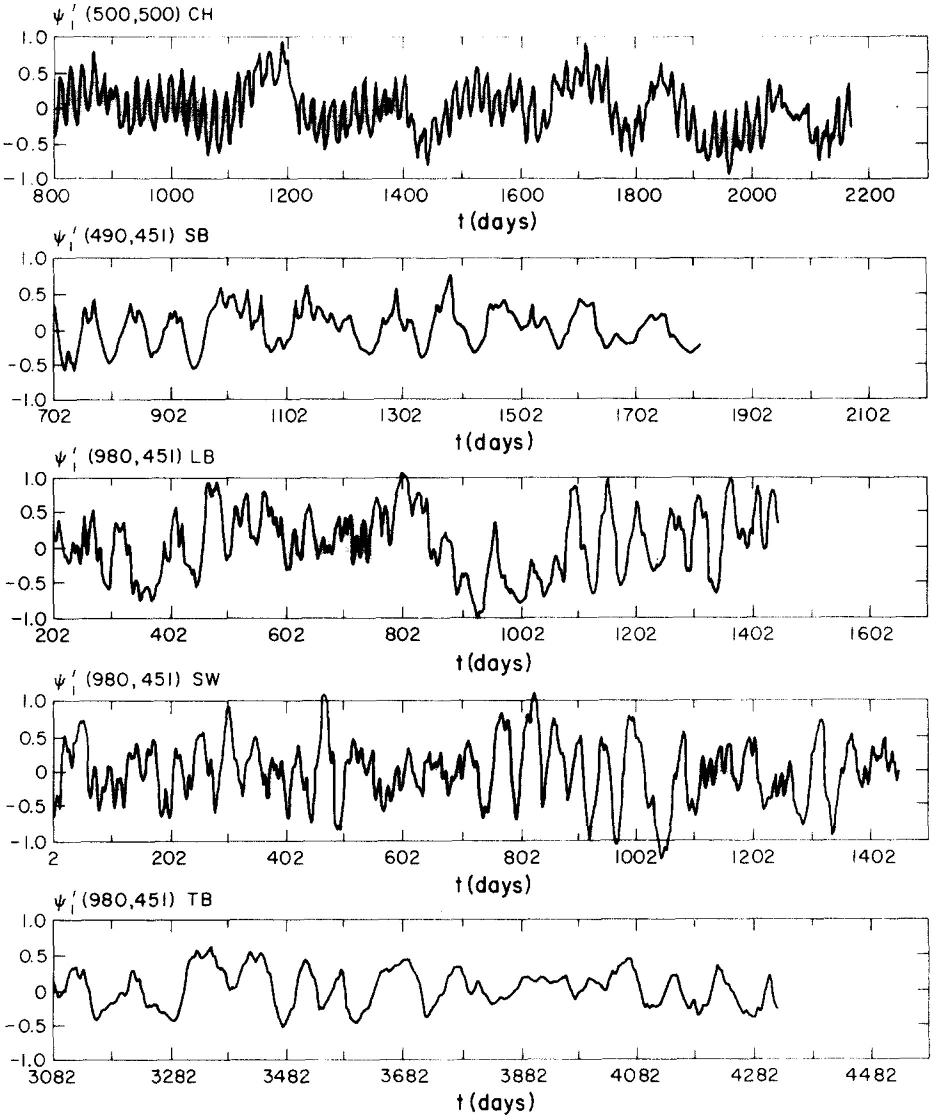

Fig. 12. Time series of upper layer streamfunction (10^5 m^2 s^{-1}) for different cases, at locations which are near the centers of the mean jets and well away from the zonal boundaries at $x = 0$ and L_x (see Fig. 2).

days. The former could be due to a mean jet advection (n.b., $\langle \overline{u}_1 \rangle$ is larger in CH than LB — see Fig. 3 — and the horizontal length scales seem to be smaller — see Fig. 1). The longer time period could not be due to bulk advection. The sequences for SB, LB, and SW are generally similar, particularly if the SB differences of a somewhat smaller amplitude and a lesser amount of high frequency structure are discounted due to the generally greater distance from its jet center (n.b., in Fig. 2 the mean SB jet is south of the time sequence location). A very clear illustration of the absence of correlation between the wind forcing and the fluid response is shown in SW; the wind has peak values at day 90 and every 180 days thereafter, whereas ψ_1' has no recognizable behavior with this period. The dominant time period in TB is about 90—130 days. Its slowness compared to the other cases may be due to the relative weakness of the mean TB jet, particularly at the location of the time sequence (see Fig. 2). The very long time periods exhibited in energy and transport (Figs. 5, 6, and 9) for TB are absent in ψ_1'. In particular, there are peaks in transport and total potential energy around days 3200 and 4150 and a minimum in the interval between days 3450—3650. These features are not simply reflected in ψ_1' in Fig. 12, although a spectral analysis does indicate their presence (see below). This implies that the point variability is dominated by relatively small scale quantities, whose spatial integrals (hence, the contributions to transport and volume average energies) must be small.

Various frequency spectra are shown in Figs. 13—15. Fig. 13 includes ψ' and v' spectra from different locations in LB, the same ones shown in Figs. 10 and 11. The dominant feature of these spectra is their redness (i.e., a monotonic decrease with frequency). In ψ this continues through the lowest frequency analyzed (a period of ~500 days); in v there appears to be a general flattening of the spectra for periods longer than ~100 days. The high frequency end of these spectra is quite steep, typically decaying faster than ω^{-2} and, in one location, for ψ_1' in the jet center, decaying as fast as ω^{-4}. There is no universal power law, independent of location. Two spectral peaks are generally identifiable, though neither is large enough to dominate the variability. They are located around periods of 25 and 60 days. The latter is more pronounced in ψ_1', the former in v_1'. The conclusion from the time series above, that v' has faster time scales than ψ', is confirmed in the spectra here.

A survey of spectra from locations near the upper layer mean jet centers is shown in Fig. 14. The CH case again stands out as the one with the simplest time behavior. Three spectral peaks are prominent (in contrast to only two dominant periods being visible in Fig. 12); they are located around periods of 8—9, 20, and 190 days. It is tempting to claim that vestiges of the 20 day peak carry over to the other cases, although its appearance is sometimes very faint and it is debatable whether a common cause should exist for it given the variety of cases. There are other low frequency peaks of prominence in all cases. They are located at the following periods: 190 days (CH), 80—150 days (SB), 60 days (LB, WW, SW), and 100—150 days (TB). These peaks are

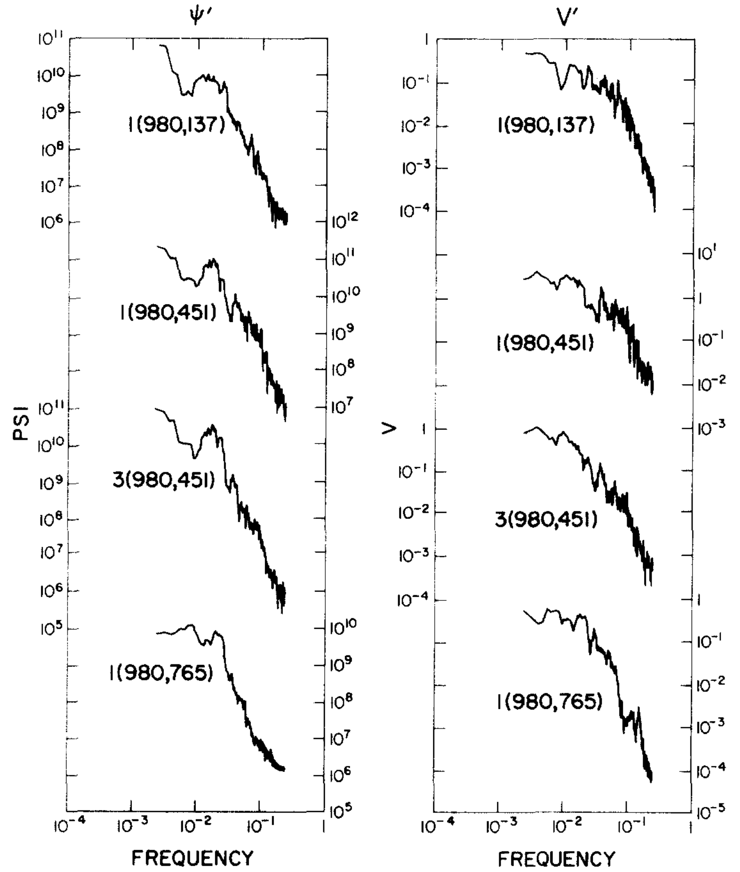

Fig. 13. LB spectra for the time series in Figs. 10—11. Spectral units for ψ' and v' are m^4 s^{-2}/(c.p.d.) and m^2 s^{-2}/(c.p.d.) respectively and the frequency units are c.p.d. All spectra are calculated from time series with a resolution of $\Delta t = 2$ days in the time interval of days 202—1440. A top-hat running average over 5 adjacent frequency bands has been applied to the raw spectral estimates. The curves are labeled by their locations $i(x, y)$, where i is the layer index and x and y are distances in km from the southwest corner of the basin.

evident in both ψ and v in all cases, though the 60 day peaks in LB, WW, SW are moderately weak in v.

The transient wind forcing sequence of LB, WW, and SW is of particular interest here. For these cases, the relative amplitude of the semi-annual forcing component increases from 0 to 2/3 (see (24), (25), and Table I). In the ψ_1' spectra it is difficult to see a response peak at the forcing frequency of $5.6 \cdot 10^{-3}$ cycles per day; if anything, it is WW which exhibits the closest approximation to a peak. The v_1' spectra suggest a slightly stronger response. The SW case shows a clearly significant peak in the correct location. How-

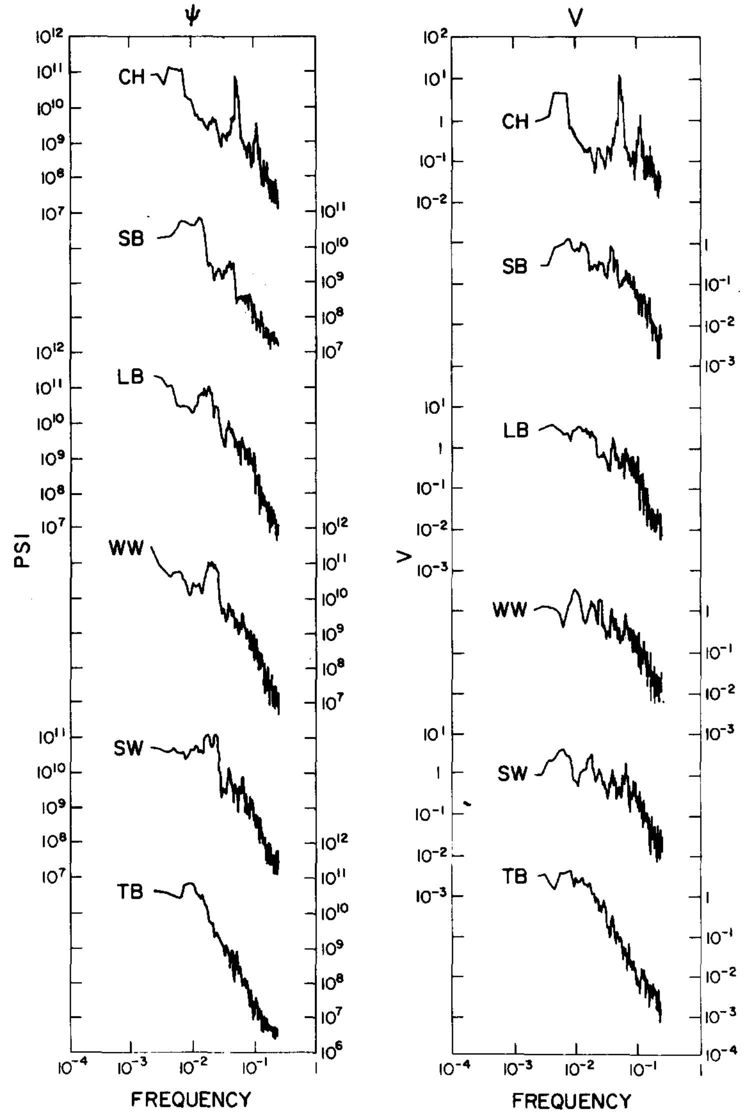

Fig. 14. Spectra for ψ'_1 and v'_1 in the upper layer jet for all six cases in Table I. The locations are as in Fig. 12 with the further specification of x = 980 km and y = 451 km for WW. For all cases, Δt = 2 days. The equilibrium intervals from Table I were used here, except for SB (instead only days 702—1800 were used) and TB (only days 3082—4320 were used).

ever, these results together indicate that the fluid response to even a very strongly fluctuating wind can be quite modest, and that the intrinsic turbulent variability of the equilibrium balance of the Antarctic Circumpolar Current can dominate many aspects of the forced transience. The present model is no doubt inadequate for modeling many aspects of transient wind-driven currents. In particular, high frequency forced currents, with small vertical scales, might behave quite differently from the present solutions. Nevertheless, the solutions do suggest that one should be cautious in drawing conclusions about the influence of fluctuating winds upon the ocean.

The case TB provides the longest time series from our set of numerical solutions. Spectra from the entire 3834 day equilibrium period are shown in Fig. 15. The red character of the ψ_1' spectrum does seem to be lost at very low frequencies, although, in contrast to previous cases, the v_1' spectrum seems more generally red than the ψ_1' one. The very regular three year oscil-

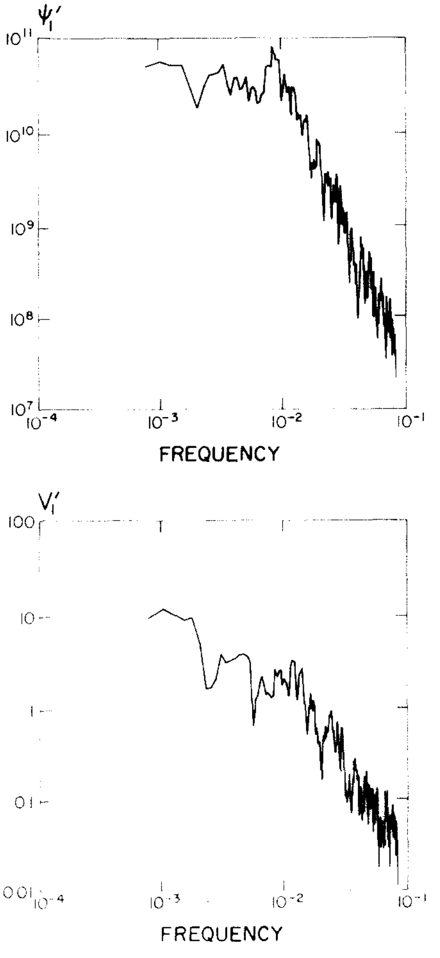

Fig. 15. Spectra for ψ_1' and v_1' from TB at $x = 980$, $y = 481$ for a long time series. Here $\Delta t = 6$ days and the time interval is days 486—4320. A running 5-band spectral average has been applied as in Figs. 13 and 14.

lation seen in transports and energies (Figs. 5, 6, and 9) does seem to be reflected in a peak near 10^{-3} c.p.d. The length of the time series is not quite sufficient to clearly define this peak, however. Also, this peak in ψ_1' and v_1', while present, is not nearly so dominant a feature of the spectrum as it would undoubtedly be in spectra of transports and energies. In Fig. 15, there appears to be an additional low frequency peak around 300 days which was not resolved in the shorter records analyzed in Fig. 14.

Phase diagrams are a means of exposing eddy propagation. In our Antarctic geometries, it is primarily zonal propagation which should occur, although, in selected locations (e.g., over the bottom slope in TB), some meridional propagation should occur as well. Figs. 16 and 17 present zonal phase diagrams; that is, they show contours of streamfunction in an (x, t) space. The full zonal interval is included $(0 \leqslant x \leqslant L_x)$, but only a 180 day time interval during the equilibrium period is shown. The slope of the contour lines should be interpreted as a phase propagation; uniform propagation would appear as a prevalent orientation of the slopes.

Diagrams for several y values and several streamfunction fields are shown in Fig. 16 for the case LB. The y values were selected to illustrate behavior in the narrow region south of the jet, in the jet, and in the broad region north of the jet. The most uniform propagation can be found in ψ_1 and $\psi_1 - \psi_3$ in the jet region. The contour slopes that characterize the places of strongest ψ gradients correspond to phase speeds of around 30—35 km day^{-1}. If this speed is divided into the distance between eddy centers of like sign (which we estimate as about 850 km), then a period of 24—28 days results; this is the faster of the two periods identified from the time sequences and spectra above. Because these regions of strong ψ_1 gradient do not typically persist for a time long compared to a period, it is clear that a single period or phase speed is insufficient to characterize the ψ field. Also, the individual eddy centers do not persist long enough to propagate across the entire domain. Thus, the simple description of mean jet advection of passive spatial structures, while useful for estimating the magnitude of periods and phase speeds, is by no means a complete description.

The ψ_3 diagram for the jet region shows a much less uniform pattern of contour line orientation. There are even periods of westward propagation, including one (for days 560—620 in the western half of the basin) where the phase speeds are of the order of Rossby wave speeds, a few km day^{-1}. This disparity between upper and lower layer propagation rates exists even though individual eddy centers are correlated between the layers. This is largely due to the fact that many of the eddy centers are nearly non-propagating; for example, there is a clear bias towards streamfunction maxima in the middle of the x domain.

The southern region streamfunction features are extremely intermittent and thus without any clear propagating character. Their diagrams are dominated by a barotropic event near day 670, which occurred almost simultaneously at all x, and two eastwardly propagating, baroclinic events between days

560 and 610. The northern region is not as intermittent. The bias in propagation is towards the west, rapidly in ψ_1 and ψ_3 (around 30 km day^{-1}) and much more slowly in the interfacial displacement field.

A comparison of ψ_1 phase diagrams for the different cases is shown in Fig. 17. The y values have been chosen to coincide with the mean jet regions (see Fig. 2). All cases except TB show a generally eastward propagation. The CH propagation is the most rapid, which reflects its greater $\langle\bar{u}_1\rangle$ magnitude. It is interesting that the central region in x for SB, where the propagation seems to be disrupted, corresponds to the region in Fig. 2 where the mean jet makes a large excursion to the south of this y value. Certainly the most anomalous propagation is shown by TB. Even in the x region where there exists a predominantly zonal mean jet (between about 500 and 1000 km east of $x = 0$ — see Fig. 2), there is little systematic eastward propagation. Apparently the eddy behavior in TB has little to do with mean current advections.

Our final manner of illustrating the nature of the transience is by use of a principal component analysis. This technique has, for example, recently been used by Davis (1976) in describing the variability of North Pacific sea surface temperatures. The principal components are also frequently referred to as empirical, orthogonal functions.

Consider a representation for the streamfunction fluctuations where the space and time variations are separated:

$$\psi'(x, y, z, t) = \sum_j a_j(t) f_j(x, y, z) \tag{31}$$

Such a representation is a complete one whenever there are as many components to the series as there are positions at which ψ' is measured (grid points in our models). One can furthermore require that the spatial functions be orthonormal with respect to a quadratic integral average over the fluid volume V:

$$\int_V f_j f_k \,\mathrm{d}V = \delta_{jk} \tag{32}$$

In our cases the total volume V is equal to HL_xL_y. One then forms the time average spatial covariance matrix:

$$A_{lm} = \frac{1}{V}\sqrt{\mathrm{d}V_l \mathrm{d}V_m}\ \overline{\psi'(x_l, y_l, z_l)\psi'(x_m, y_m, z_m)} \tag{33}$$

where the indices l and m indicate the locations where ψ' is sampled. For our two layer models, z_l can assume only two values. The $\mathrm{d}V_l$ are infinitesimal volume elements equal to $H_l \mathrm{d}x_l \mathrm{d}y_l$, where H_l is H_1 or H_3 depending upon whether z_l is in the upper or lower layer. It can be shown that the jth eigenvalue of A_{lm} is equal to $\overline{a_j(t)^2}$ (and further that $\overline{a_j a_k} = 0$ for $j \neq k$) if the jth eigenvector is taken to be equal to $f_j(x_l, y_l, z_l)\sqrt{\mathrm{d}V_l/V}$. By these definitions the representation (31) is an expansion in the principal components of streamfunction variability. The components with the largest eigenvalues are

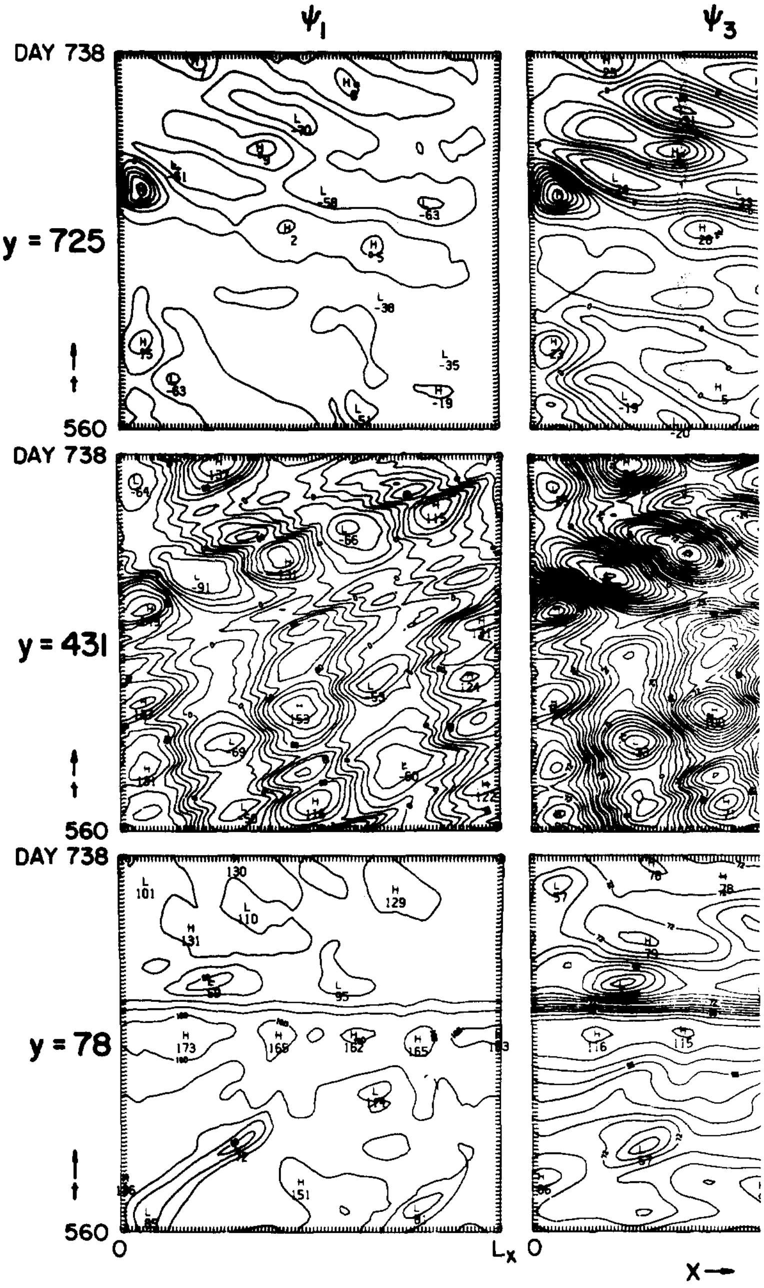

Fig. 16. Phase plots (contours of ψ in x—t space) for case LB along th
boundary. The contour intervals are $2 \cdot 10^4$ $m^2/s(\psi_1)$ or $0.6 \cdot 10^4$ m^2/s

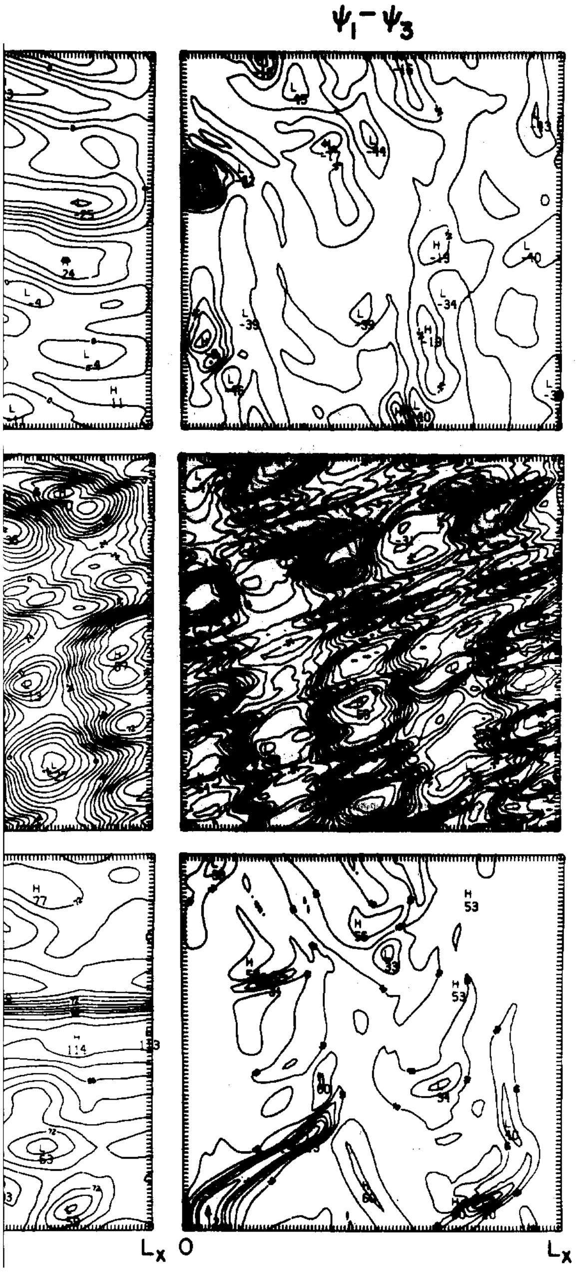

ee parallels: y = 78, 431, and 725 km north of the southern (ψ_3 and $\psi_1 - \psi_3$), and the labels are in units of 10^3 m^2 s^{-1}.

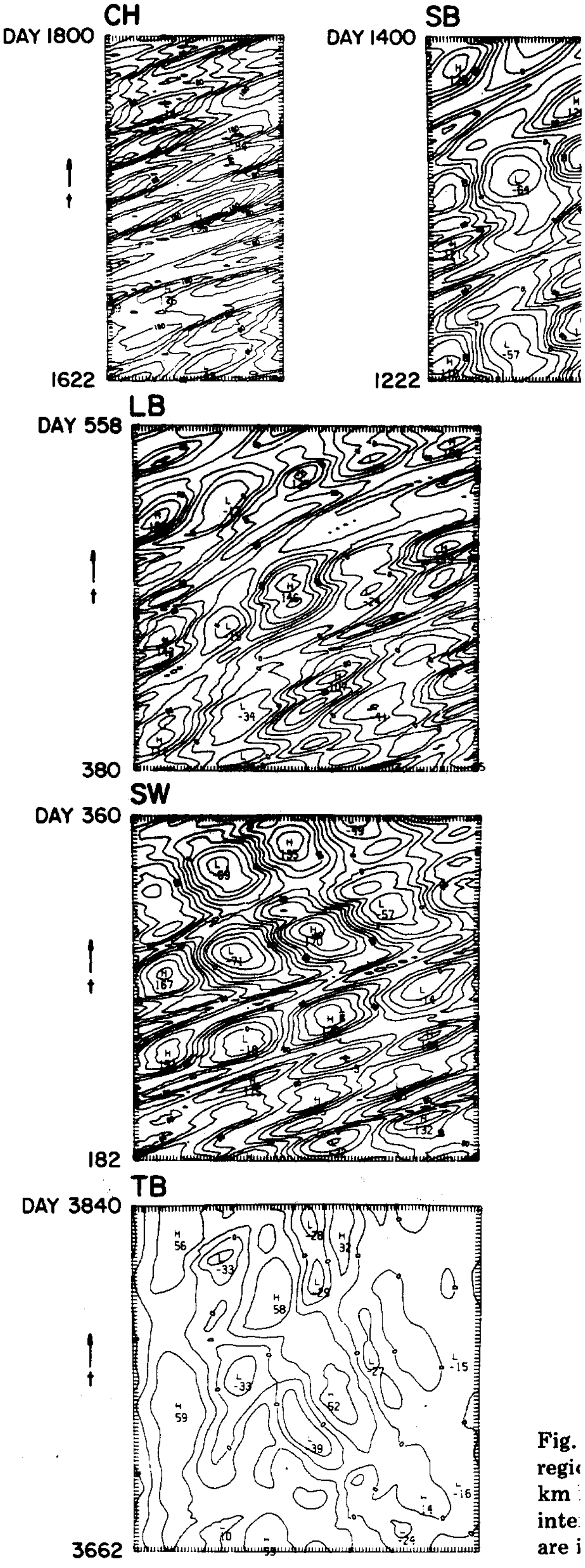

Fig.
regi
km
inte
are i

17. Phase plots for ψ_1 in the jet
on (y = 500 km for CH and y = 431
for the other cases). The contour
rval is $2 \cdot 10^4$ m^2 s^{-1} and the labels
n units of 10^3 m^2 s^{-1}.

the most efficient, statistically independent (with respect to the time average) descriptions of the variability of the streamfunction field. The f_j give the spatial structure of the components, and their associated amplitudes are calculated from:

$$a_j(t) = \int_V \psi'(v, t) f_j(v)\, \mathrm{d}V \tag{34}$$

The total streamfunction variance equals the trace of A_{lm}, and the ratio of $\overline{a_j^2}$ to tr(A) gives the percentage of the total variance associated with a given component. We shall only examine the first few components for the various cases below, because they contain almost all of the total variance. The separation between adjacent locations for calculating the f_j is about $\mathrm{d}x_l \approx \mathrm{d}y_l \approx$ 110 km. For the first few components, further resolution is unnecessary. We have also examined the principal components for u' and v' variability. For the first few components of ψ', the velocity information is redundant; that is, the velocity patterns agree with a geostrophic interpretation of the streamfunction patterns (n.b., between velocity and streamfunction there are differences in the fraction of the total variance associated with a given component).

The first seven principal components for CH are shown in Fig. 18. This case has a particularly simple and orderly description in terms of these components. The gravest component, which contains 34% of the variance, is a zonally invariant ridge in ψ, which is coherent between the layers, though weaker and broader at depth. It has virtually zero transport (recall from Fig. 9 that the total transport does not fluctuate in CH). It can be interpreted as a bulk meridional shift in the location of the zonal jet, without any change in its strength. Its time sequence is unrelated to bulk energy fluctuations (Figs. 5 and 6), but is highly correlated with the longer time fluctuations in ψ_1' in the middle of the basin (Fig. 12). Its amplitude is sufficient to account for most of those fluctuations.

The remaining six components should be considered in pairs. The second component is quite similar to the third, but shifted by one quarter wavelength to the east. $a_3(t)$ is highly correlated with $a_2(t)$, but leads it by a quarter period. Thus, these two components combine to represent simple eastward propagation of the associated spatial structures. These structures are eddies of 1000 km zonal wavelength, with meridional dimensions of the mean jet vertically in phase but stronger in the upper layer (where the mean jet is stronger), of larger meridional scale in the lower layer, and with a phase speed of 0.06—0.07 m s^{-1} to the east. These characteristics are qualitatively those of the stable jet modes discussed in McWilliams (1977c), though the phase speeds are somewhat lower here. The period of these components is about 200 days; this period was previously identified in component 1 and Figs. 12 and 14.

Components 4 and 5 also comprise an eastwardly propagating pair with a jet mode character (a_5 leads a_4). The meridional scale is that of the jet, the

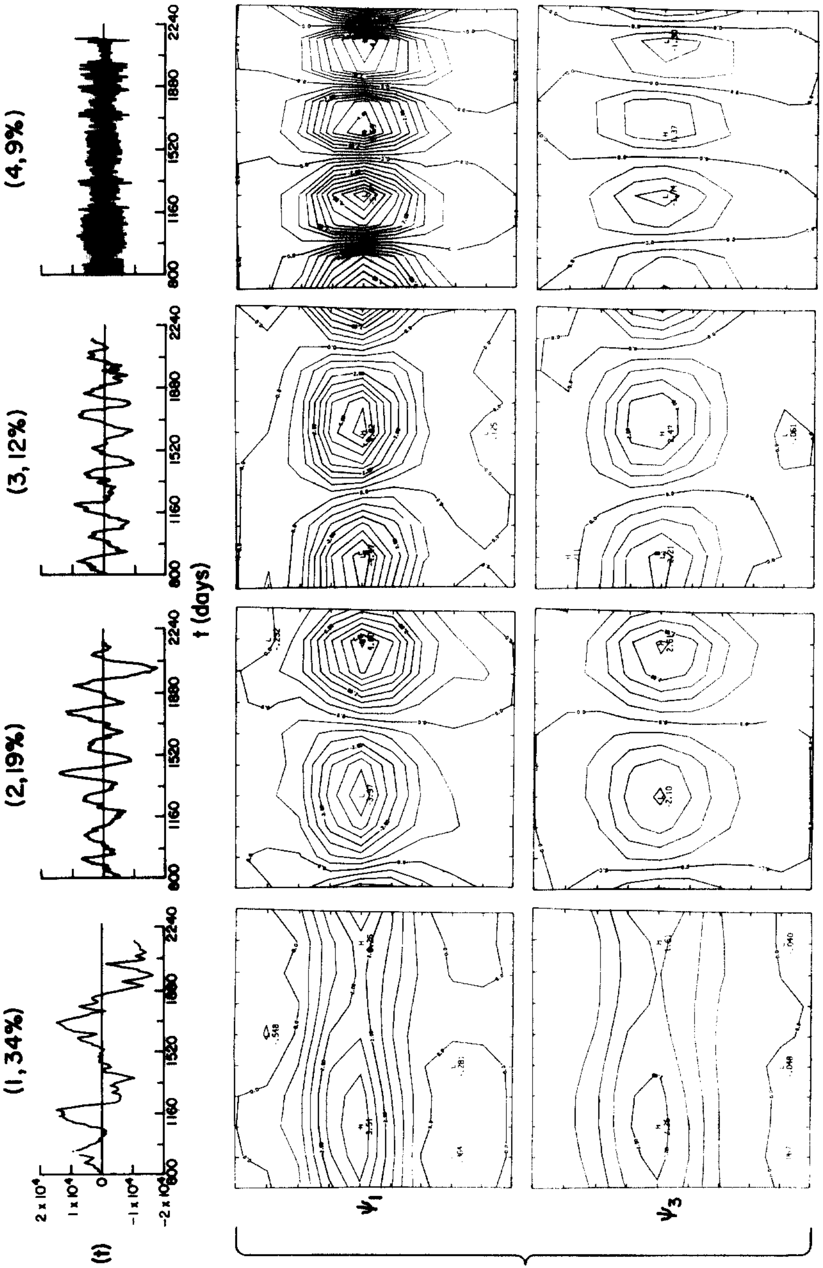
(1, 34%)
(2, 19%)
(3, 12%)
(4, 9%)
$a_j(t)$
2 x 10⁴
1 x 10⁴
0
−1 x 10⁴
−2 x 10⁴
800
1160
1520
1880
2240
t (days)
ψ_1
ψ_3
f_j

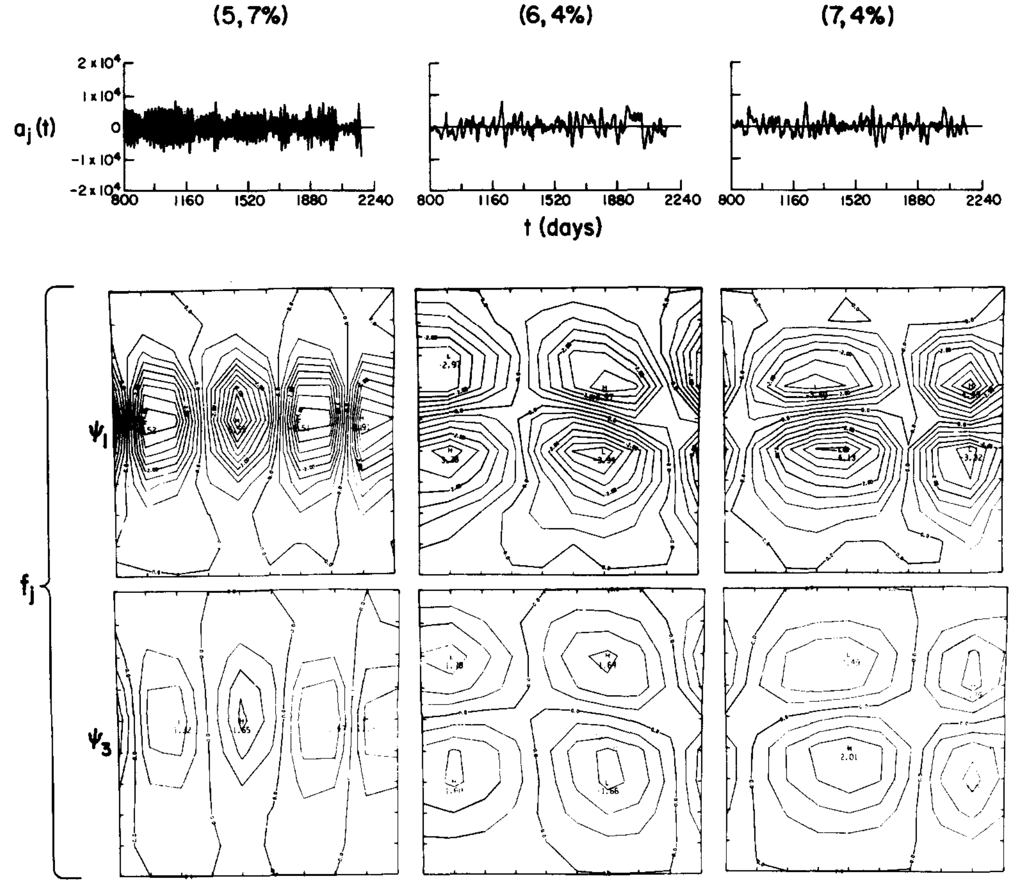

Fig. 18. The first 7 principal components for ψ' in CH. For each one, the amplitude time sequence $a_j(t)$ ($m^2\ s^{-1}$) and the upper and lower layer spatial patterns (normalized as in (32)) are shown. The components are labeled by (j, p_j%), where p_j% is the percentage of the total variance residing in the jth component. The total variance for CH is tr(A) = $1.7 \cdot 10^8\ m^4\ s^{-2}$. The contour interval is 0.5.

zonal wavelength is shorter than that of components 2 and 3 (500 km), the phase speed is higher (0.30—0.35 m s^{-1}), and the period is about 20 days (which also was previously identified). Components 6 and 7 are an eastwardly propagating jet mode pair which is anti-symmetric about the jet center. The associated period is variable, but approximately 40—50 days (one can recognize a small peak in the ψ'_1 spectrum at this period in Fig. 14). The phase speed is 0.2—0.3 m s^{-1} to the east.

Together these seven components account for 88% of the total ψ'_1 variance in CH; actually, they represent only one standing and three propagating patterns. They account for all but one of the prominent features (i.e., the 8—9 day period) in the frequency spectra*, and conform in many ways to a simple analog, the jet mode. As a succinct summary of the variability, they must be considered of fundamental value. Obviously, however, there remain important unanswered questions about why these particular components are present and what are their dynamical couplings with each other, the mean jet, and the wind driving and dissipation.

The interpretation for the principal components of other cases is less simple than those of CH. Fig. 19 shows the first four components for LB; collectively, they account for 73% of the total streamfunction variance for this case. The dominant component is one with a significant transporting element, and its amplitude is highly correlated with the time sequence of total transport (Fig. 9); the magnitude of a_1 is within about 70% of being able to account for the magnitude of the total transport fluctuations. The second component has the structure of the standing eddies for LB (see Fig. 2), and thus represents fluctuations in their amplitudes; there is almost no transport associated with this component. Propagating component pairs are not as apparent in LB as in CH. Components 2 and 3 have something of a spatially shifted relationship and, at least for certain intervals, their amplitudes are correlated with a temporal shift (e.g., during days 300—400, component 3 leads component 2, implying a westward propagation). The oscillation periods of these components are highly variable (which is consistent with the generally red spectra shown in Fig. 10). Nevertheless, one can recognize a very long period of about two years in components 1 and 2, a period of around 100 days in components 2 and 3, and a period of about 60 days in component 4. Only the last of these was identified as a spectral peak in Fig. 10.

Finally, in Fig. 20 are shown the dominant principal components for the remaining cases. In all cases the amplitude time sequences are highly correlated with the total transports (Fig. 9), as is also true of LB (the only exception occurs in CH where the transports do not fluctuate). A remarkable 63% of the SB variance is associated with its dominant principal component. This is perhaps related to the fact that it combines a transporting structure with elements of the standing eddy patterns (see Fig. 2); thus, these two processes must be linearly coupled in SB so that a single structure can describe much of the variability of both. There are also some aspects of this combination in SW and TB, though not as many; also, the dominant modes in these cases account for smaller percentages of the total variance. The amplitude in SW is clearly in phase with the transient wind driving; the associated pattern is thus a major part of the fluid response. One might describe this pattern as a standing wave, but there is no known reason why this should be thought of

---

* In fact, a propagating jet mode pair of principal components has been found with the 8—9 day period. They each account for 0.6% of the total variance, are symmetric about the jet center, have a wavelength of 300—350 km, and have a phase speed of 0.4—0.5 m s^{-1} to the east. This pair is further discussed in section 10.

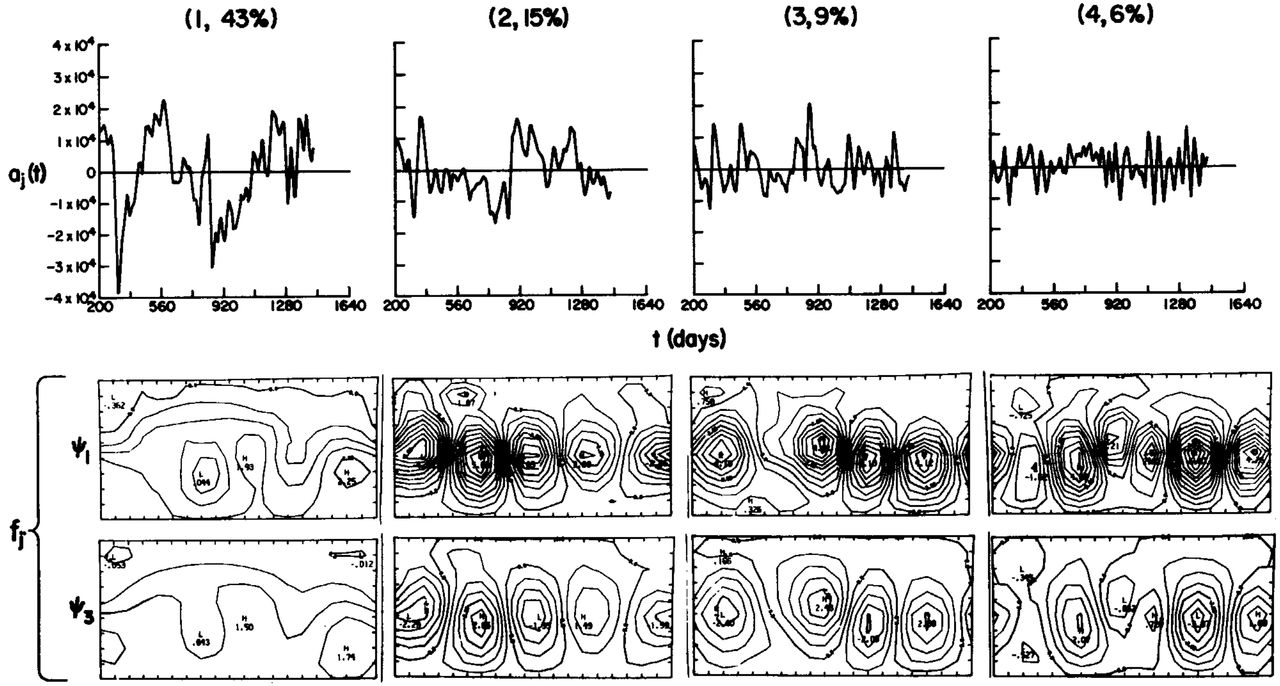

Fig. 19. The first 4 principal components for ψ' in LB. The format is as in Fig. 18. The total variance is $\mathrm{tr}(A) = 3.9 \cdot 10^8$ m^4 s^{-2}.

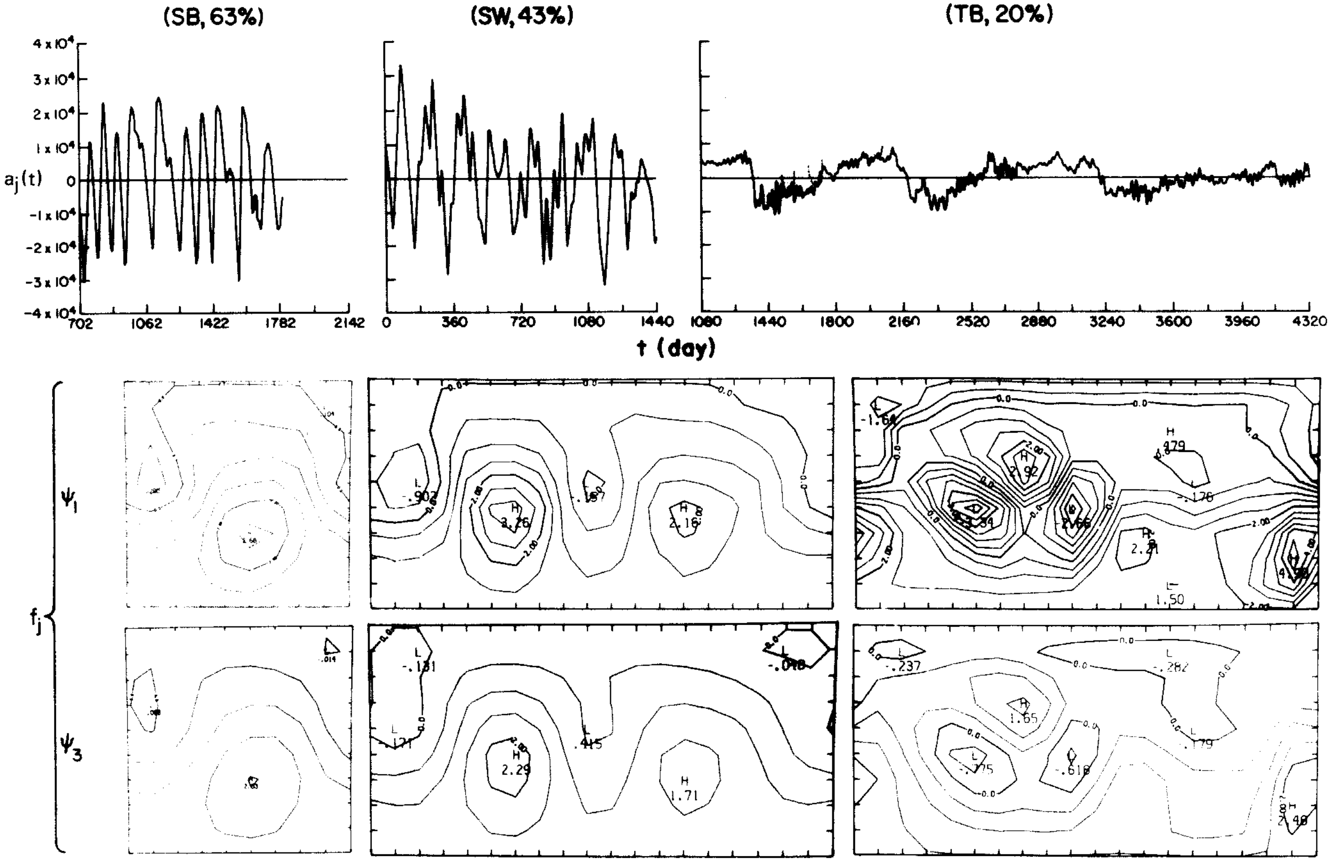

Fig. 20. The dominant principal components for the cases SB, SW, and TB. The percentages of the total variance associated with these components is listed for each one; the total variances are 3.1, 4.0, and 0.9 · 10^8 m^4 s^{-2} respectively.

as a situation of near resonance with the basin geometry or mean flow. In a similar manner, we recognize the dominant component of TB as the pattern associated with the strong, 1000 day oscillation described above. Certainly there is no simple relation between the ψ_i' and the topographic contours in this case.

8. ZONAL MOMENTUM

The budget equations for mean zonal momentum are given in equations (18)–(20). In this section we shall examine these budgets and identify the important processes in them.

As was also true for the transient descriptions, the case CH has the simplest momentum balance. Fig. 21 shows this balance for both the upper layer and the total (depth integrated) momentum. For each of these, only three of the source or sink terms make any appreciable contribution. The zonal wind stress provides a source of eastward momentum at all latitudes in the upper layer, the horizontal Reynolds' stress divergence C_1 is an eastward source in the middle of the jet and a sink on its periphery (i.e., the eddies concentrate mean momentum), and the transient interfacial pressure drag D' is a sink for upper layer momentum at all latitudes (n.b., it is a source for lower layer momentum — see (18)). The standing eddies play no role here because they are too weak in CH (see Fig. 2). The budget for the depth integrated momentum is equally simple: the wind is the primary source, the horizontal eddy transports (primarily in the upper layer) concentrate the jet, and the bottom friction is the momentum sink. In fact, the two budgets are virtually identical, with eddy pressure drag for the upper layer being replaced by bottom drag for the total.

The fact that horizontal eddy transports tend to concentrate and intensify the mean mid-latitude jet has been known for the atmosphere for many years (Starr, 1951; Kidson et al., 1969). Furthermore, the essential physical characterization of this fact is that barotropic planetary waves transport westward momentum (Kuo, 1951). If one imagines a source for these waves in the jet center (by some instability process such as the baroclinic instability evident in Fig. 7 for CH), then they leave behind eastward momentum as they propagate out from the jet and subsequently deposit westward momentum in an exterior region. This deposition process is probably associated with near-critical layers (Dickinson, 1968, 1971). It seems probable that some variant of this process is occurring in CH, since the eddies are at least equivalent barotropic and undoubtedly have their source in the jet region.

The momentum budgets for the remaining cases are shown in Fig. 22 for the gap latitudes only. In the upper layer, the primary source is always the direct wind forcing and the primary sink is the interfacial pressure drag (mainly D' in SB, LB, and SW and mainly D_* in TB). The horizontal, transient eddy Reynolds' stress divergence C_1 is a strong secondary source in the jet centers, though usually a sink on the southern flank of the jet. The

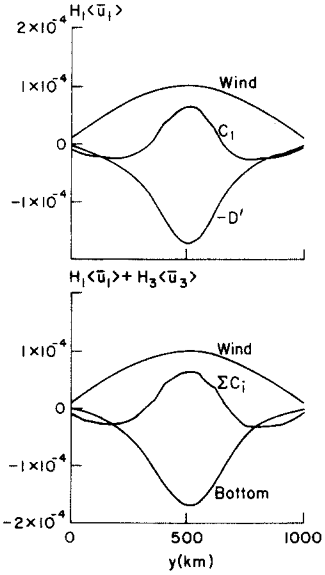

Fig. 21. The major elements of the budget for the time and zonal averaged zonal momentum for the case CH. Only the larger terms in (18) are included here. The upper panel is for the tendency in $H_1\langle\overline{u_1}\rangle$, the lower for that in $H_1\langle\overline{u_1}\rangle + H_3\langle\overline{u_3}\rangle$. Units are $\mathrm{m}^2\ \mathrm{s}^{-2}$.

standing eddy Reynolds stress divergence B_1 and pressure drag D_* are weakly opposing to the transient C_1, except in TB. For TB, all of the above quantities except D_* are momentum sources, with D_* the sole sink.

The total momentum budget presents a similar picture. The pressure drag terms D_* and D' can no longer contribute, but their role as momentum sinks is simply replaced by either bottom friction or, for TB, by the bottom pressure drag E. There are appreciable lower layer contributions, as well as upper, to the Reynolds' stress divergences B_i and C_i.

A summary description of these budgets is the following one. The wind stress is the major momentum source, the eddies (transient and standing) concentrate the upper jet and transfer momentum downward, and either the frictional bottom drag of the mean lower layer jet or, if $\langle\overline{u_3}\rangle$ is too weak, the topographic pressure drag against the bottom serve as the momentum sink. The downward transfer of zonal momentum by the transient interfacial pressure drag is equivalent to the downward transfer of mean energy in Fig. 7 (i.e., $\int\int \bar{\mathbf{u}}_1 \cdot \overline{p_1'\nabla h_1'} = \{K_1, P\}$).

9. POTENTIAL VORTICITY

In many respects, the potential vorticity is the most fundamental dependent variable of our quasigeostrophic model. It is a conservative property of a fluid parcel except for dissipation and wind driving [see (1)]. The instan-

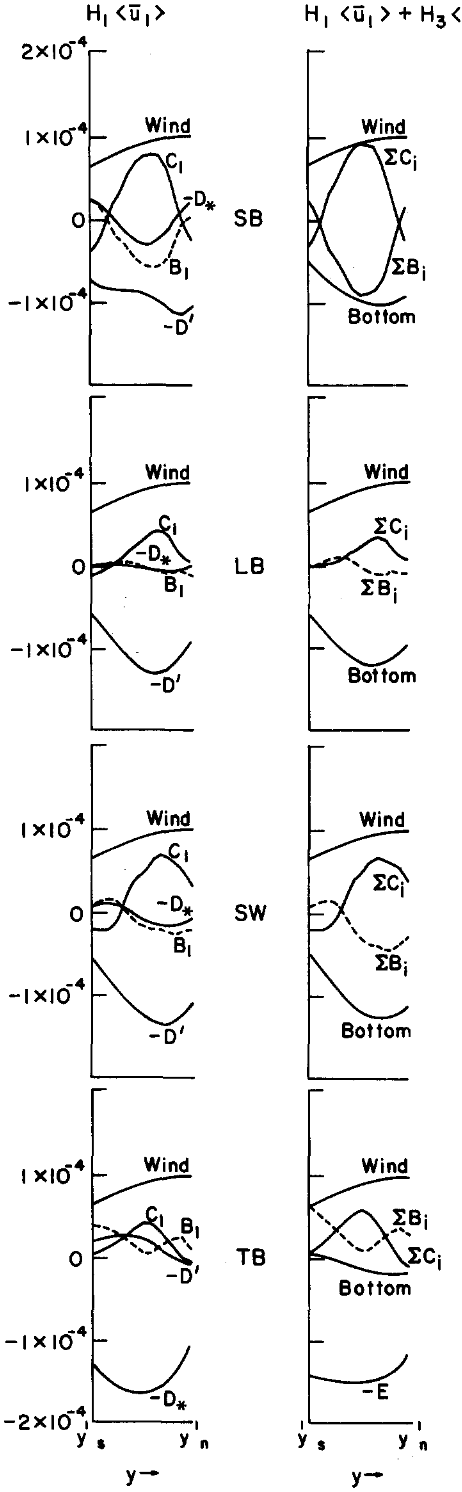

Fig. 22. Momentum budgets for SB, LB, SW and TB. The format is as in Fig. 21. Only points within the gap are plotted.

taneous balance for equation (1) is a structurally complicated one, with short space and time scales. The local rate of change q_t is primarily balanced by potential vorticity advections — the contributions from dissipation and wind forcing are two to three orders of magnitude smaller [their relative unimportance in a few realizations of mid-latitude mesoscale eddy potential vorticity balances was shown empirically by McWilliams (1976b)]. This situation remains true even for the time averaged point balances, though the disparity between the conservative and non-conservative terms is not quite as great. The pointwise changes in $\overline{q}_1$ are mainly due to interfacial height changes in (2), with both relative vorticity and planetary vorticity changes each contributing about 25% as much. In $\overline{q}_3$ all three types of potential vorticity contribute comparably.

It is only for the time and zonal mean, $\langle \overline{q}_i \rangle$, that the budget contributions from the non-conservative processes become appreciable. The various terms in these budgets are defined in (21) and (22), and the upper and lower layer budgets are plotted in Figs. 23 and 24, respectively. In the $\langle \overline{q}_1 \rangle$ budget, the wind is a source of positive vorticity in the north and negative in the south. For CH only two other terms contribute appreciably, and both are due to the transient eddies. Away from the jet latitudes d_1 and e_1 from (22) balance the wind vorticity. In the jet, however, the eddy stretching term d_1 strongly opposes the wind while the eddy relative vorticity transport e_1 reinforces it: together these two terms support a very strong meridional gradient of $\langle \overline{q}_1 \rangle$ in the jet, which is an expression of the momentum concentration seen in section 8. In this sense, then, the horizontal transport of e_1 is a local jet source — stronger than the wind for potential vorticity — while the vertical stretching of d_1 is the sink. Since $d_3 = -(H_1/H_3)d_1$, this upper layer sink is a lower layer source. In the lower layer (Fig. 24), the source due to eddy stretching transport d_3 is balanced by a bottom frictional sink. The horizontal transport e_3, while not negligible, acts in a lesser way to spread the meridional gradient of $\langle \overline{q}_3 \rangle$ (hence, the lower layer jet). It does this by forcing locally intensified gradients on the edges of the jet (at $y \approx 360$ and 640 km).

In a less simple manner, these balances also occur in the other cases. There, however, the standing eddies, as well as the transient ones, make important contributions and the meridional structures are more complex. In general, in the upper layer the standing eddy transports tend to oppose the transient eddy ones, and the horizontal transports (c_1 and e_1) oppose the vertical ones (b_1 and d_1). The most consistent opposition to the wind vorticity forcing is provided by the transient eddy stretching d_1 (which, as above, can be viewed as systematically transferring the wind driving to the lower layer through d_3). In SB, LB, and SW the horizontal transient eddy transport e_1 acts most clearly to intensify $\partial\langle \overline{q}_1 \rangle/\partial y$ in the jet, while this role is partly taken over by the standing eddies in TB through the term c_1.

In the lower layer balances (Fig. 24), there is again a tendency for mutual opposition between standing and transient eddy terms of like type (i.e., c_3 versus e_3 and b_3 versus d_3). As in the CH interpretation above, it is reason-

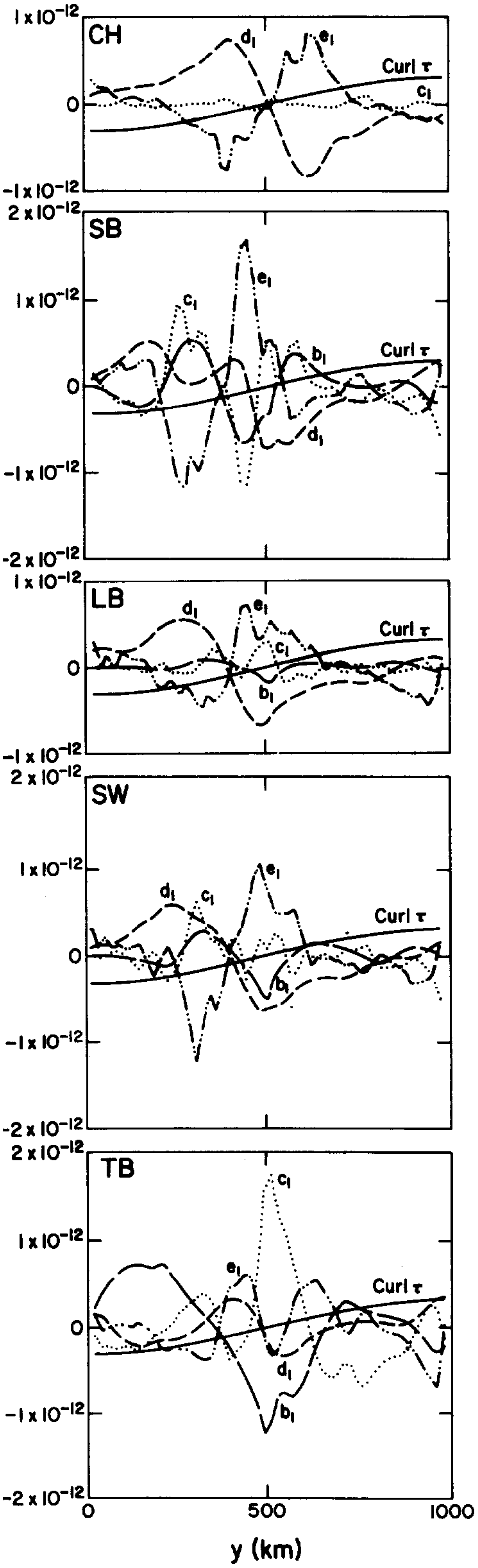

Fig. 23. The major terms in the budget (21) for $H_1^{-1}\langle\overline{q_1}\rangle$. Units are s^{-2}.

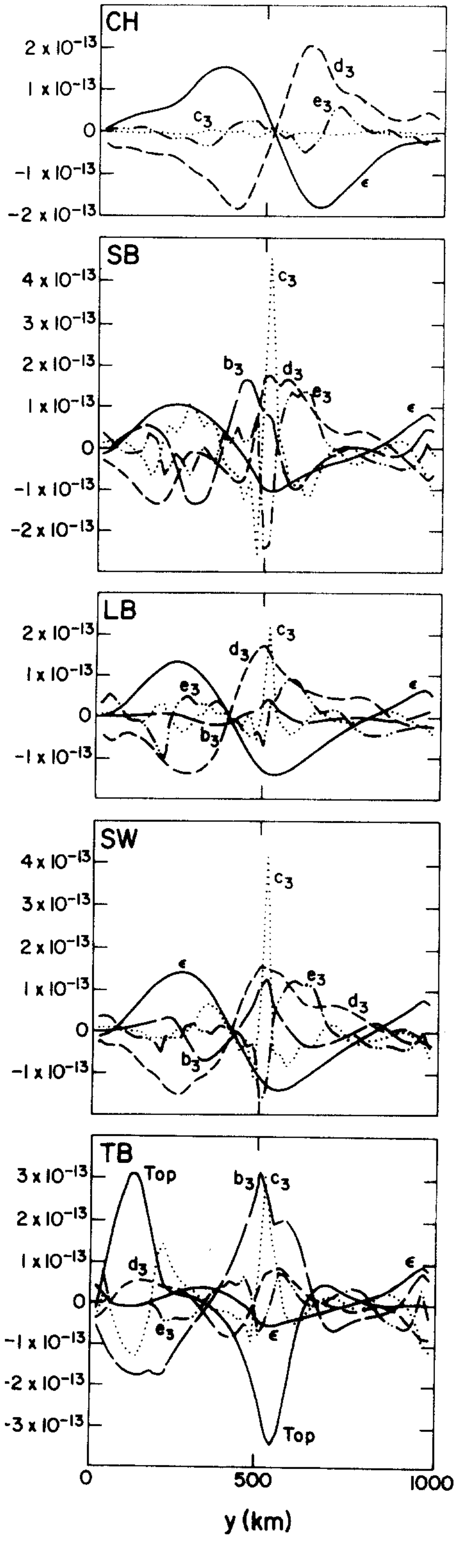

Fig. 24. The major terms in the budget (21) for $H_3^{-1}\langle \bar{q}_3 \rangle$. Units are s^{-2}. The curve labeled "top" is the final term in (21).

able to regard the eddy stretching terms (mainly d_3 in SB, LB, and SW and b_3 in TB) as transmitting the systematic wind vorticity forcing to the lower layer. The primary balance to this forcing is provided by the bottom friction and, in TB, the topographic torque [the last term in (21)]. In all of the cases with a partially blocked channel, there is a strong spike in the horizontal standing eddy transport c_3 at the northern edge of the gap. This spike is balanced primarily by lateral friction a_3 (which is not plotted). This is the only location in either layer where lateral friction makes an important contribution to the $\langle \overline{q} \rangle$ budget.

For the numerical solutions we have been analyzing, the purely steady-state solutions to (1) would be ones where the standing eddies could effect all the transports which are necessary in the energy, momentum, and vorticity budgets (e.g., D_* would dominate D' in momentum and the b_i would dominate the d_i in potential vorticity). Furthermore, insofar as the point balances are dominated by conservative process, any steady solution would have to approximately satisfy:

$$J(\overline{\psi}_i, \overline{q}_i) = 0 \qquad (35)$$

in each layer.

In fact, the transient eddies do not play a negligible role in the budgets for these solutions; in most cases they play an essential role. Also, the wind forcing and bottom friction must contribute significantly at least in a volume integral. Nevertheless, it is of interest to examine (35) as a relevant null model. A general solution to (35) is $\overline{q}_i$ a function of $\overline{\psi}_i$ alone, with no direct dependence on x or y separately. Figs. 25 and 26 show scatter plans of all point values for $\overline{q}_i$ and $\overline{\psi}_i$ throughout the domains of the various cases. A single valued functional relationship would imply a solution to (35). While clearly this is not strictly true for any of the cases, it is remarkable how much, viewed from this perspective, this characterization does seem apt for all cases except TB.

The closest approximation to such a functional relationship occurs in CH, and the upper layer relationship seems somewhat tighter than the lower layer one; in this case it is the absence of standing eddies which assures the relationship. Cases SB, LB, and SW seem generally similar, with a recognizable width (i.e., degree of non-uniqueness) to the functional relationship. For these cases the largest departures to the unique relationship occur on the side boundaries, where our boundary conditions (3) force a discrepancy: $\overline{\psi}_i$ is constant, while $\overline{q}_i$ varies because of $H_i\beta y$. This boundary departure is most noticeable in the lower layer (Fig. 26). The case TB exhibits no basic functional relationship.

It was shown in McWilliams (1977a) that the quasigeostrophic stability of these mean states, assuming they approximately satisfy (35), is assured by:

$$\frac{d\overline{q}_i}{d\overline{\psi}_i} > 0$$

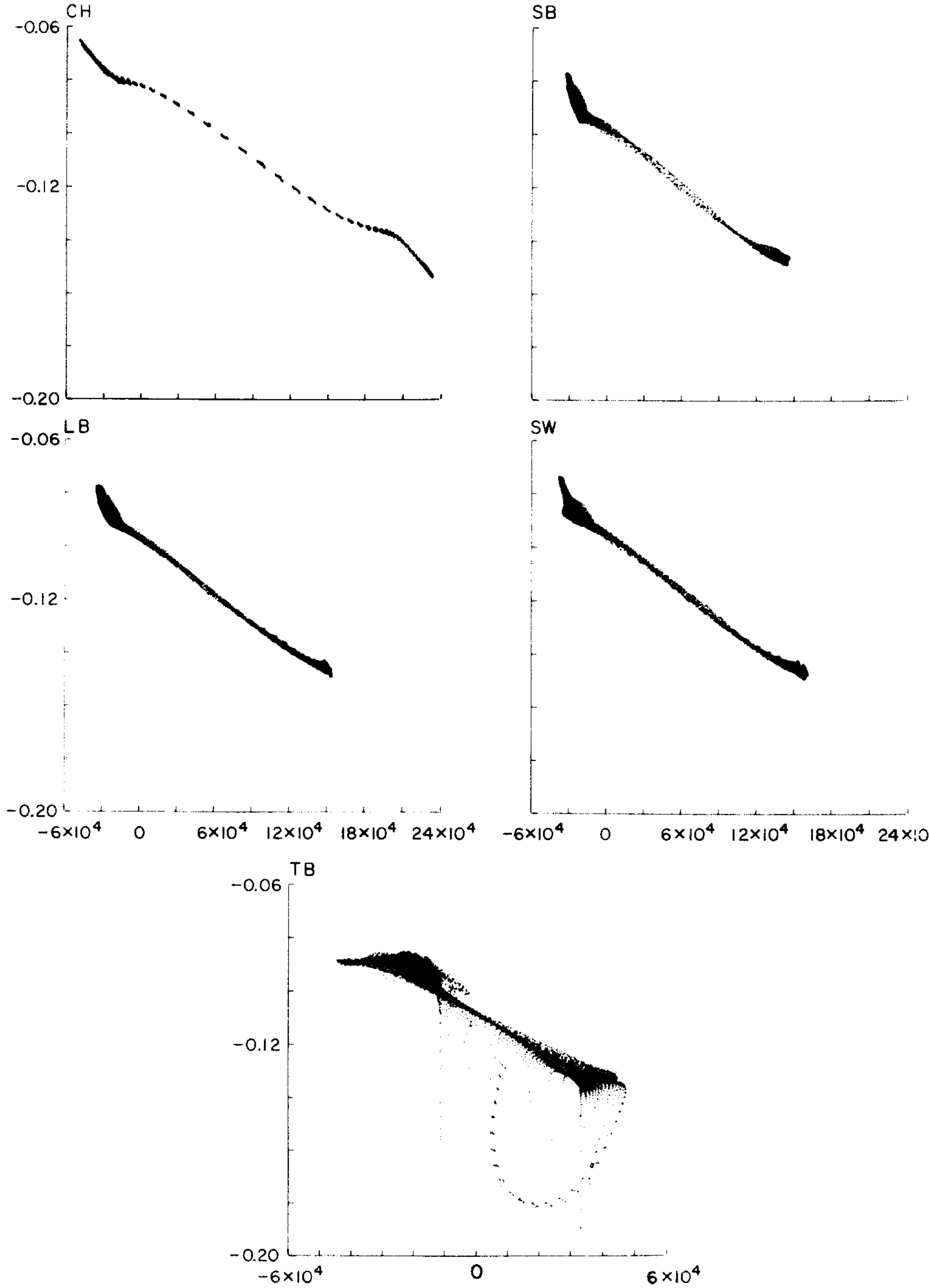

Fig. 25. Scatter plots of $\overline{q}_1$ against $\overline{\psi}_1$ for the various cases. Units are m s^{-1} for $\overline{q}$ and m^2 s^{-1} for $\overline{\psi}$.

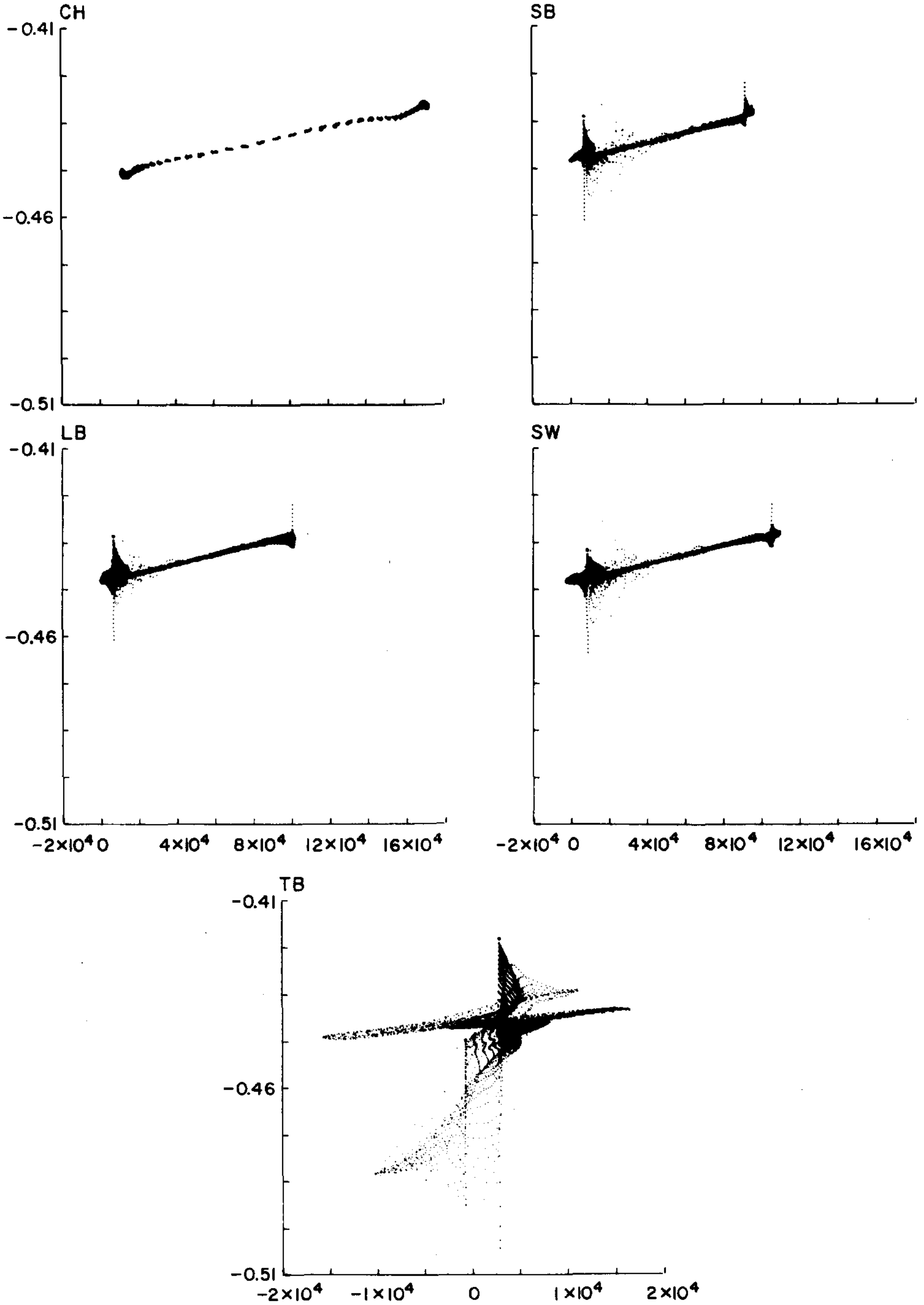

Fig. 26. Scatter plots of $\overline{q_3}$ against $\overline{\psi}_3$ (as in Fig. 25).

everywhere in each layer. This inequality does seem to be generally characteristic of the lower layer, but it is clearly isolated in the upper layer. Thus, while it is approximately correct to view these mean states as close to ones which have steady, purely conservative point balances there is no basis for believing such mean states would be nearly stable ones. The reality about these solutions, of course, is that transient eddies are forced from the fluid response to a purely mean driving force, and that the mean states do have significant transient eddy transports contributing to their balances. Nevertheless, the idealized equation (35) is a fundamental reference relation for these solutions, and the whole transient cycle is associated with the slight non-uniqueness of this relation.

10. EDDY PROPERTIES AND FLUXES IN A CHANNEL

In the preceding sections, we have presented several gross measures of eddy structural and propagation characteristics and eddy contributions to mean budgets. By an equally gross measure, we have identified eddy generation through the baroclinic instability of the zonal mean jet in all cases except TB (see section 5). Because of the relative simplicity of the CH solution, clearly indicated in the principal components of section 7, we can be more precise about the eddy properties in this case. In this section we shall consider the relation between linear instability theory and the numerical principal components, the momentum transports by each of these, the validity of several eddy heat flux parameterizations, the degree of supercriticality in the mean state of CH, and the role of a reverse energy cascade, analogous to that of two-dimensional turbulence.

A linear stability analysis has been made for CH, similar to that described in Haidvogel and Holland (1978). Equations (1) and (3) were solved as a linear eigenvalue problem for the small amplitude fluctuations about the time and zonal mean solution. The fluctuations were assumed proportional to $e^{\sigma t - ikx}$, where σ is the eigenfrequency, and the eigenfunctions varied with y only. When Haidvogel and Holland (1978) applied such an analysis to numerical solutions for enclosed gyres, the results were only partially successful in matching the numerical eddy characteristics; this was perhaps to be expected, since the numerical mean state was not zonally invariant and the numerical fluctuations were not zonally periodic. In CH, however, the geometrical assumptions of the instability analysis conform to the numerical circumstances, and more exact correspondences between the two should occur.

Curves of the eigenfrequency σ associated with the meridional mode of maximum instability [largest $\mathrm{Re}(\sigma)$] are shown in Fig. 27, plotted as a function of zonal wavenumber k. Because of the zonal periodicity of CH, on a distance L_x, only integer k values in Fig. 27 are directly comparable to the numerical solution. Wavenumber 3 lies near the maximum instability value; wavenumber 2 has a much smaller but significantly positive $\mathrm{Re}(\sigma)$; wavenumber 4 has a negligible rate of instability; and wavenumbers $\leqslant 1$ or $\geqslant 5$ are

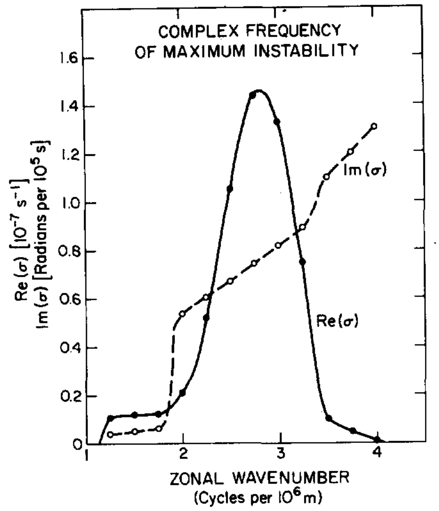

Fig. 27. The complex frequencies of maximum linear instability about the mean CH state shown in Fig. 3.

stable. We might, therefore, expect to observe the wavenumber 3 mode, and perhaps mode 2, in the CH solution. Fig. 28 shows the wavenumber 3 spatial structure in comparison with an additional CH principal component propagating pair (with a_j^2 values smaller than those in section 7). The wavelengths of the mode and the components are identical, 330 km. The period of the unstable mode is 9 days (see Fig. 27). The time behavior of the principal components is shown in Fig. 29. The time lagged covariance $C_{AB}(\tau)$ indicates that the two components form an eastwardly propagating pair, with component B preceding A by slightly more than 2 days. This corresponds to a period of 8—9 days, matching that of both the unstable mode and the spectral peak in Fig. 14 (the only peak unaccounted for in the components of Fig. 18). Thus, both the unstable mode and the components have an eastward phase speed of 0.3 m s^{-1}. The e-folding growth time for wavenumber 3 is 87 days from Fig. 27. The amplitude ratio, (max ψ_3/max ψ_1), is somewhat different in the mode and the components, respectively it is 0.45 and 0.2—0.3. Another difference between the two is in their degree of spatial phase shifts: the unstable mode has larger horizontal displacements separating eddy centers in the two layers and more of a banana-shaped pattern in the horizontal than does the principal component pair. These features are equivalent to greater maximum eddy flux divergences (e.g., in C_1 or D') per unit streamfunction amplitude in the mode compared to the component.

A similar identification can be made between the unstable wavenumber 2 mode (with a wavelength of 500 km, a period of 14 days, a growth time of 550 days, and an amplitude ratio of 0.4) and the principal components 4 and 5 in Fig. 18 (with a wavelength of 500 km, a period of ~20 days, and an am-

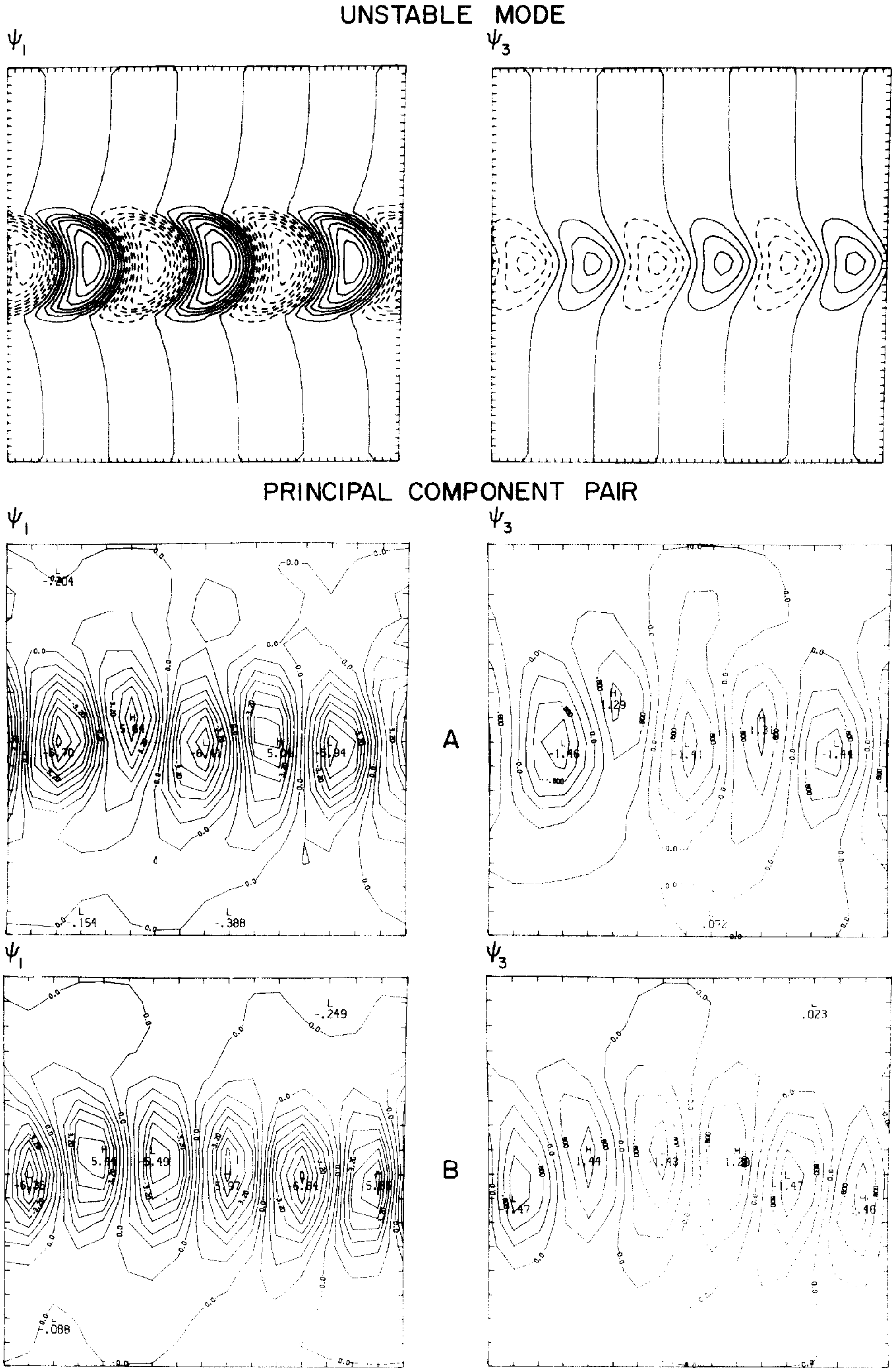
UNSTABLE MODE
ψ_1
ψ_3
PRINCIPAL COMPONENT PAIR
ψ_1
ψ_3
A
ψ_1
ψ_3
B
L
-.204
-6.70
5.64
-6.41
5.04
-5.84
L
-.154
-.388
-1.46
1.29
-1.41
1.31
-1.44
.072
L
-.249
-6.36
5.44
-6.49
5.97
-6.64
5.88
.088
.023
-1.47
1.44
-1.43
1.28
-1.47
1.46
0.0

plitude ratio of 0.5). The discrepancy between the periods should not be taken seriously, given the steepness of the $\mathrm{Im}(\sigma)$ curve near $k = 2$ in Fig. 27. Note that this component pair, which has a 16 times greater streamfunction variance than does the component pair in Figs. 28—29, also has a 6 times smaller growth rate in the linear theory.

We also can compare the unstable modes and the principal components in their flux divergence contributions to the general circulation. The presentation will be in terms of the zonal mean momentum transports D' and C_1; however, from section 2 and Appendix B it is apparent that analogous conclusions could be drawn from other mean budgets. Because of the orthogonality of the $a_j(t)$ with respect to a time average, any total quadratic eddy flux divergence can be written as the sum of divergences from individual principal components alone. When the first 20 principal component contributions to D' and C_1 were evaluated, it was found that only two propagating component pairs contributed significantly. These two are those which have been identified above with the linear unstable modes. Their meridional distributions are shown in Fig. 30 and should be compared to the distributions of the total D' and C_1 in Fig. 21. The component contributions have shapes similar to those of the totals, although they are somewhat more restricted in meridional extent and exhibit a relatively excessive contribution to C_1 compared to D'. Their amplitudes are comparable to those of the totals: in the jet center the components in Fig. 30 together provide more than the total C_1 and about 80% of the total D'. Thus, these few components accomplish the greater part of the eddy contribution to the maintenance of the general circulation. Also shown in Fig. 30 are the contributions from the linear unstable modes with wavenumbers 2 and 3, normalized so that their peak D' values equal those of the components with which they have been identified. Their meridional extent is less and their C_1/D' ratio is larger than that of the components.

Together the principal components of Fig. 30 account for only 17% of the total streamfunction variance. Since the linear theory does not suggest that any of the other, more energetic, principal components can be generated by an instability of the mean state — and since Fig. 30 suggests that the others are generally unimportant in the mean budgets — we conclude there must be an efficient energy cascade from the unstable modes to the other (generally larger scale) components. This cascade is thus a reverse one, as in two-dimen-

Fig. 28. The top panel shows the streamfunction patterns associated with the unstable mode with k = 3 cycles per 1000 km (see Fig. 27). The lower four panels are the principal components for CH which have a dominant 8—9 day period. Their eigenvalues $\overline{a_j^2}$ are $0.987 \cdot 10^6$ and $0.984 \cdot 10^6$ $\mathrm{m}^4\,\mathrm{s}^{-2}$ respectively (i.e., they each account for 0.6% of the total variance). The horizontal grid for the covariance matrix is smaller here than for Figs. 18—20 (i.e., $dx_l = dy_l = 63$ km instead of the 110 km of Section 7). The eigenmode has an arbitrary normalization but equal contour intervals in each layer (solid and dashed lines imply positive and negative values respectively). The principal components are normalized as in (32) and have a contour interval of 0.4.

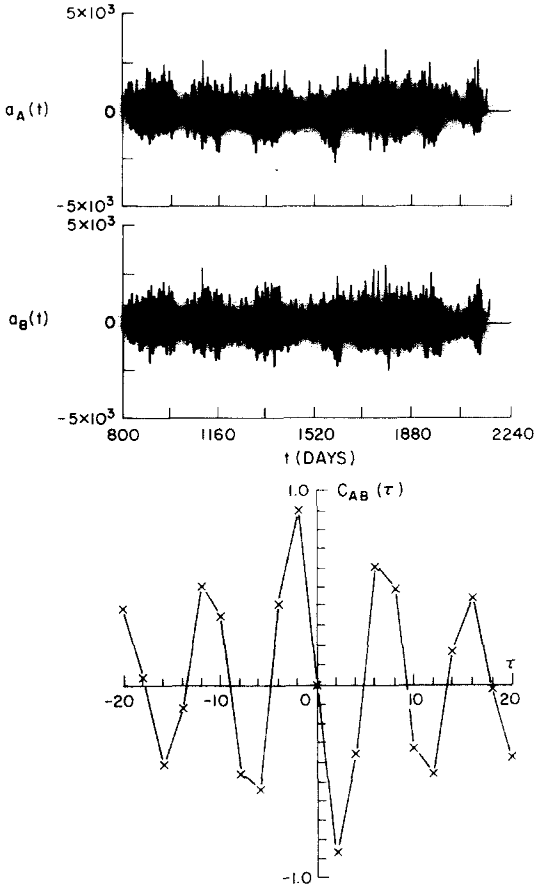

Fig. 29. The time series associated with the two principal components shown in Fig. 28 and their correlation function (n.b., $C_{AB}(\tau) = \overline{a_A(t)a_B(t + \tau)}\ \{\overline{a_A^2}\,\overline{a_B^2}\}^{-1/2}$).

sional turbulence (see Batchelor, 1969). Note, however, that this cascade is not a "barotropification" of the flow (as described by Rhines, 1977), undoubtedly because of the presence of a vertically sheared mean jet.

Linear theory can, therefore, be judged relevant to many aspects of the equilibrium turbulent balance in CH. Since linear theory has been invoked in derivations of parameterizations of equilibrium eddy heat fluxes (e.g., Green 1970; Stone, 1974; Sasamori and Melgarejo, 1977), one can use the CH numerical solution as a test of these parameterizations. This test is far more theoretically germane than the comparisons with the equilibrium state of the earth's atmosphere which these authors discussed. From equation (B.5) the parameterization of heat flux is equivalent to that of D' in CH.

From equation (5.15) of Stone (1974), we can derive the following

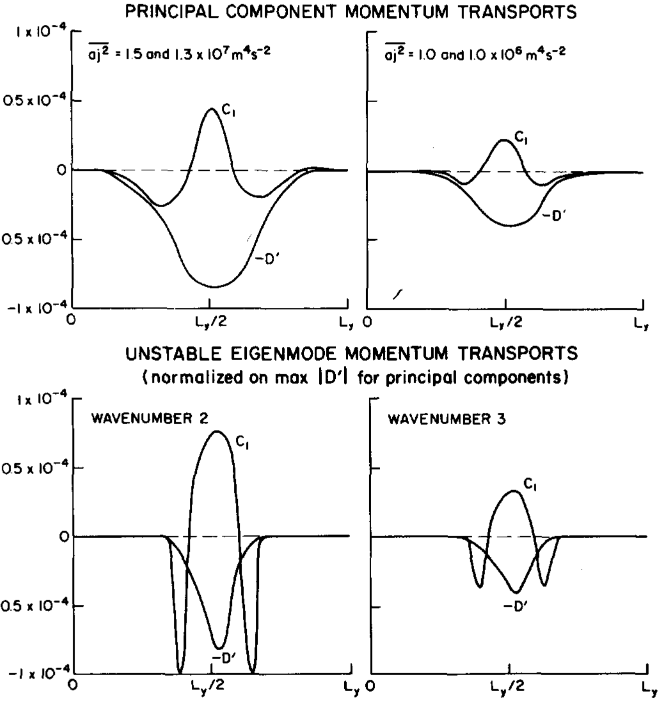

Fig. 30. The variation of D' and C_1 with y for selected propagating pairs of principal components (4 and 5 from Fig. 18 in the upper left and those from Fig. 28 in the upper right) and for the linear unstable modes with which these component pairs have been identified. Units are $m^2\ s^{-2}$.

parameterization formula (when $\beta = 0$):

$$D'_p(y) = -0.144\, f_0 \sqrt{\frac{H_1 + H_3}{2g'}}\, |\langle\bar{u}_1\rangle - \langle\bar{u}_3\rangle|\, (\langle\bar{u}_1\rangle - \langle\bar{u}_3\rangle) \qquad (36)$$

This curve is plotted in Fig. 31 along with D' from CH. There are striking discrepancies: the parameterization formula is a significant overestimate of D' in the jet center, (36) is much less smooth in y than D', and (36) does not vanish near the bounding walls. This latter defect can be eliminated by including Stone's (1974) correction for $\beta \neq 0$; this correction has little influence upon the parameterization in the jet center. Green (1970) and Sasamori and Melgarejo (1977) recommended formulas which are similar to (36), though ones intended to apply only in a y average. Their numerical coefficients were somewhat different, and in Green (1970) there was an additional Froude number factor. For the parameters of the earth's atmosphere, the three parameterizations agree; for the parameters of CH, they all yield overestimates of D'. If one examines the assumptions upon which (36) is based,

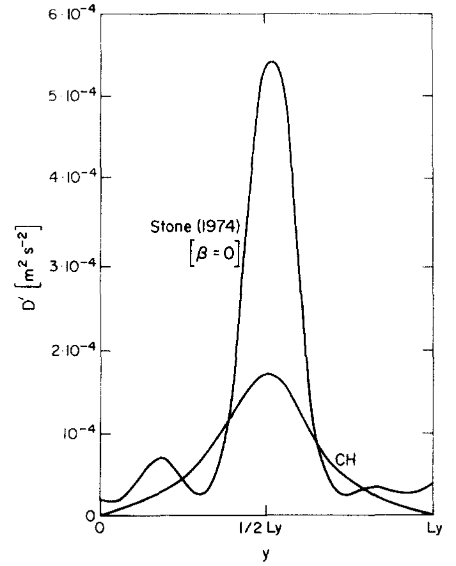

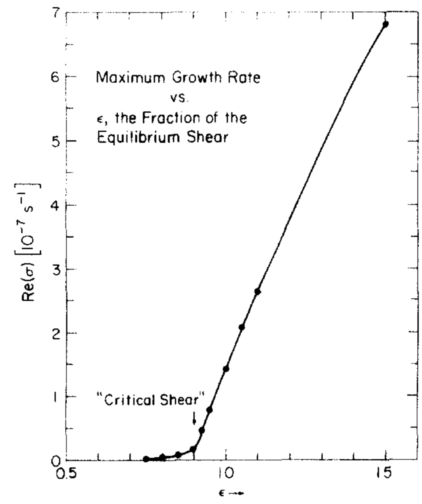

Fig. 31. A comparison of $D'(y)$ from the numerical solution CH and the parameterization formula (36), taken from Stone (1974). Units are $m^2\ s^{-2}$.

Fig. 32. The maximum growth rate as a function of the fraction of the equilibrium velocity shear in CH. This graph is the result of an eigenvalue calculation based upon a lower layer velocity $\langle \overline{u}_3 \rangle$ and an upper layer $\langle \overline{u}_3 \rangle + \epsilon(\langle \overline{u}_1 \rangle - \langle \overline{u}_3 \rangle)$, where the $\langle \overline{u}_i \rangle$ are from Fig. 3.

one finds them in disagreement with various properties of the CH solution. For example, Stone (1974) assumed equal mean and eddy kinetic energies in equilibrium, whereas in CH K_i' is about half as large as K_i (see Fig. 7). Even worse, the total K_i' in CH is much greater than the small fraction which is associated with the most unstable mode in contrast to Stone's identification of the mode with the total. Secondly, the conversion efficiency of the unstable mode (i.e., the correlation coefficient between v' and T') is not the same at infinitesimal and finite amplitudes (see Fig. 28). Finally, the instability process in CH is not purely local in y — note the greater smoothness of D' from CH in Fig. 31. The prediction of localness is based upon the meridional scale of the most unstable mode being that of the deformation radius, which is smaller than that of the jet. This is not always true even in the linear theory (n.b., Simmons, 1974), nor is it true in CH (see Fig. 28).

Recently, Stone (1977) has presented an alternative parameterization for heat flux, though one which yields similar results to (36) for the earth's atmosphere. The hypothesis is that the heat flux is what it must be so that the time and zonal mean vertical shear in zonal velocity is near the value for marginal instability. The advocated criterion for marginal instability is that for a broad jet in an inviscid, two layer fluid. Phillips (1954) derived the critical velocity difference ΔU_c when $H_1 = H_3$; when $H_1 \neq H_3$, the following formula is the relevant one (Robinson and McWilliams, 1974):

$$\Delta U_c = \min\left[\frac{\beta g' H_1}{f_0^2}\frac{\gamma^4}{4\delta\gamma^4 - 1}\{1 - \delta + \sqrt{4\delta(\gamma^4(1+\delta)^2 - 1)}\}\right] \qquad (37)$$

where $\gamma = f_0/K_e\sqrt{g'H_1}$, $\delta = H_1/H_3$, and K_e is the zonal wavenumber of the perturbation mode. The minimization is over all values of γ. For the parameters of CH, $\gamma_{\min} = 1.3$ and $\Delta U_c = 0.09$ m s^{-1}. From Fig. 3, we can see that the numerical $\Delta U(y) = U_1 - U_3$ has a peak value of 0.33 m s^{-1}; thus, by the criterion (37), CH is significantly, not marginally, supercritical. However, if we use instead of (37) a criterion based upon the eigenvalue problem described at the beginning of this section, then $\Delta U(y)$ in CH is within 10% of a bulk ΔU_c. This is shown in Fig. 32, where an abrupt transition in growth rate (as well as other modal properties) occurs at a fraction of 0.9 of the equilibrium shear in CH. Thus, the results from CH conform quite well to a variant of Stone's (1977) hypothesis: the eddies do indeed effect a marginally supercritical mean flow, at least by the more complicated criterion of Fig. 32.

11. THEORIES OF THE ANTARCTIC CIRCUMPOLAR CURRENT

The essential difference between the present theoretical calculations and previous ones is that the interior fluxes of momentum and potential vorticity are caused by turbulent processes which are calculated rather than grossly parameterized by eddy viscosities (representing generally unspecified processes). This, in our opinion, represents a significant advance in the completeness and self-consistency of the theory, but it does not necessarily obviate the conclusions from previous theories which were more cavalier about the turbulent processes.

Crease (1964) presented a succinct but valuable summary of the current theoretical hypotheses about the gross balances in the Antarctic Circumpolar Current (ACC), and the reader is referred there for more detail than we shall give. One simple conception is that the ACC is purely zonal and the direct wind driving should be locally balanced by eddy momentum diffusion. Hidaka and Tsuchiya (1953) estimated that the diffusivities required for this would be either 0.2 m^2 s^{-1} or 10^6 m^2 s^{-1} depending upon whether the friction were vertical or horizontal. Stommel (1957) felt these levels of turbulence were indefensible* and he, and later Wyrtki (1960), argued that the geometry of the ACC should not be considered zonally open — because of the intrusion of partial barriers by islands and topographic features along all latitude lines in the ACC region — and that, therefore, a zonal pressure gradient could exist to balance the wind stress. In such a case the frictional

---

* A typical value for horizontal diffusivity in the middle of a subtropical gyre would perhaps be 100 m^2 s^{-2} (Freeland, Rossby, and Rhines, 1975).

requirements for balance would be less than in a zonally open channel, and the ACC would behave as the confluence of closed basin western boundary currents driven by interior gyres with a Sverdrup (1947) vorticity balance. It is obvious, however, that this conception cannot be wholly correct since it requires no zonal transport across some meridian.

In several ways topography has been hypothesized as important for the ACC. Kamenkovich (1962) stressed its importance in guiding the transport streamlines [along lines of $f/(\text{depth})$] and influencing the total transport. He relied on a vertical eddy diffusivity to obtain a local frictional balance with the winds. He stated that a value of 10^{-2} m^2 s^{-1} was sufficient, but Gill (1968) later pointed out that at least 10^{-1} m^2 s^{-1} was required for a consistent application of this model. Fandry (1971) examined a linear, barotropic model with bottom friction and topography and concluded that topography impedes transport by enhancing the bottom frictional drag. This is because the circumpolar circuit is lengthened for any fluid parcel due to meridional deviations induced by the topography and because the bottom velocities are enhanced near topography. Schulman (1970) presented numerical examples of barotropic flow with bottom friction and topography. Munk and Palmen (1951), in an early but insightful paper, argued that the bottom velocities were probably too small for bottom friction to balance the wind driving but felt that bottom pressure drag [the final term in (19)] would be adequate. They recognized the difficulty in vertically transferring the stress to the bottom and suggested either vertical eddy diffusion or large northwards excursions of the ACC water in a meridional cell (with sinking equatorwards of the ACC) as means of effecting this transfer. The former mechanism, which has a counterpart in our solutions, is certainly the more direct one.

There have also been a few studies of combined thermal and wind forcing of the ACC. In an early study, Fofonoff (1955) argued that the two forces would augment each other, while relying on a vertical eddy diffusivity of 2 m^2 s^{-1} to obtain a balance. Several steady-state numerical calculations, with large eddy diffusivities have also been made. Cox (1975) presented solutions for the global oceans, and Gill and Bryan (1971) studied a more local model of the ACC. In the latter, a complicated coupling was discovered involving a thermally driven meridional cell and wind-driven flow through a topographically blocked Drake Passage. The vertical and horizontal eddy coefficients of friction were $0.5 \cdot 10^{-2}$ and $5 \cdot 10^{4}$ m^2 s^{-1} respectively. Both of these values are larger than in usual subtropical gyre simulations but smaller than the values identified by Hidaka and Tsuchiya (1953) for either process acting alone. However, the numerical experiments were made for an $f_0 \sim 10^{-5}$ s^{-1}. If f_0 were increased by an order of magnitude to a correct value, then the diffusivities would have to be increased as well in order to preserve the Ekman numbers.

We feel it inappropriate to assess the combined thermal and mechanical aspects of the ACC on the basis of our present solutions. However, the validity of the purely wind-driven hypotheses discussed above can be examined.

In most cases — the major exception is the extreme form of the Stommel hypothesis — it is crucial that the fluid interior either be barotropic or have a very large vertical diffusion of momentum (with a coefficient on the order of 1 $\mathrm{m}^2\,\mathrm{s}^{-1}$). The several numerical solutions we have presented demonstrate (rather than assume) the partially barotropic nature of the ACC and also demonstrate the nature of the large vertical momentum transfer (i.e., the interfacial pressure drag induced by the geostrophic, mesoscale eddies — see section 8). An approximate measure of the magnitude of this transfer comes from equating the surface stress $\underline{\tau}$ [$=10^{-4}\,\mathrm{m}^2\,\mathrm{s}^{-2}$ from (24)] and the mean bottom frictional stress $h_3\epsilon\bar{u}_3$ with an interior, vertical eddy stress:

$$\nu_\mathrm{V}\frac{\partial\bar{u}}{\partial z}\approx\nu_\mathrm{V}\frac{\bar{u}_1-\bar{u}_3}{\frac{1}{2}H}$$

For the approximate values of $\bar{u}_1\sim0.5\ \mathrm{m\,s}^{-1}$ and $\bar{u}_3\sim0.25\ \mathrm{m\,s}^{-1}$ (see Fig. 3), we find $\epsilon h_3\bar{u}_3$ equal to $10^{-4}\mathrm{m}^2\,\mathrm{s}^{-2}$; for an equivalent interior stress, ν_V must equal 1 $\mathrm{m}^2\,\mathrm{s}^{-1}$. Thus, our mean balance for the ACC is quite consistent with many of the previous conceptions; also, the turbulent eddies which can accomplish this have been exposed. Furthermore, the various hypotheses about topography — its influence on the transport magnitude and the location of the streampaths (e.g., Kamenkovich, 1962), its capability of producing topographic form drag to balance the wind stress (e.g., Munk and Palmen, 1951), and even its tendency to partly support Sverdrup interior balances (e.g., Stommel, 1957) — all find partial confirmation in the comparison of TB with the flat bottom cases. Our set of solutions does not adequately delineate the parametric sensitivities of the present class of numerical models. Hence, we are reluctant to assign proportional roles to the various mechanisms above. Nevertheless, we feel that models of this type can lead to a considerable refinement of our theoretical knowledge about the ACC.

Finally, for completeness, we include approximate estimates for several other eddy diffusion coefficients. In general, the eddy flux divergences exhibit much more structure than can be expressed by a single coefficient. However, for CH the divergences are relatively simple (n.b. Fig. 21) and such estimates are reasonable. By comparing integrands in (B.15), we can estimate the upper layer horizontal particle diffusivity as:

$$K\sim1-2\cdot10^3\ \mathrm{m}^2\,\mathrm{s}^{-1}$$

based upon Figs. 21 and 25. An upper layer, horizontal diffusivity for momentum ν_H and an interfacial, horizontal thermal diffusivity K_T can be estimated within the mean jet from the following ratios:

$$\begin{aligned}\nu_\mathrm{H}&\sim-\overline{\langle u_1'v_1'\rangle}\Big/\frac{\partial\langle\bar{u}_1\rangle}{\partial y}\\K_\mathrm{T}&\sim-\overline{\langle v_\mathrm{I}'T_\mathrm{I}'\rangle}\Big/\frac{\partial\langle\bar{T}_\mathrm{I}\rangle}{\partial y}\end{aligned}\qquad(38)$$

where the interfacial temperatures are defined by (B.3). For the CH numerical solution, we have approximately:

$\nu_H \sim -3 \cdot 10^3 \text{ m}^2 \text{ s}^{-1}$

$K_T \sim 0.9 \cdot 10^3 \text{ m}^2 \text{ s}^{-1}$

Tennekes (1977) predicted that $K_T = -\nu_H$; this is only approximately true in CH.

12. DISCUSSION

The numerical solutions presented above illustrate the nature of equilibrium turbulent balances between geostrophic eddies and mean jets. In these balances the two types of motion are inextricably coupled. However, any application of these results to the Antarctic Circumpolar Current must be made very cautiously, because it is clear that at least the basin geometry and topography are important and as yet insufficiently explored regulators of the turbulent balances.

Certainly the simplest case is the channel one CH. Because of the zonal and temporal invariance of the basin and forcing, there are no important variations in the transports and no standing eddies, and the transient eddies are, on the average, either independent of the zonal coordinate or occur as homogeneous, zonally propagating patterns. The mean jet is a strong one, with its maximum at the latitude of the maximum wind stress. It is narrower in the upper layer than the lower, because of the up-gradient horizontal momentum fluxes by the transient, upper layer eddies. The lower layer jet receives its momentum from the upper layer by action of the eddy interfacial pressure drag forces and loses it to the bottom through the parameterized frictional drag. The most energetic transient motions have the form of trigonometric functions in the zonal coordinate and appear in the frequency spectra as about four separate, broad peaks superimposed on a generally red spectrum. Their space and time structures approximately correspond to neutral, linear jet modes. Two of these peaks, at periods of 9 and 20 days, are associated with the baroclinic instability of the mean jet, as predicted by a linearized eigenvalue analysis. The unstable eddy motions have scales somewhat larger than the deformation radius. This process serves as the energy source for the transient eddies, with the other, more energetic transient motions receiving their energy by a reverse cascade similar to that of two-dimensional turbulence. The fundamental horizontal scale of the system is set by the strength of the concentration of the mean, meridional potential vorticity gradient, which is accomplished primarily by the upper layer relative vorticity flux; this scale is smaller than that of the wind-stress or channel width, but much larger than the deformation radius.

None of the other cases have a zonally invariant geometry. They are thus more complicated, and our interpretations of the essential processes are less certain. The set of cases of SB, LB, WW, and SW can be viewed as members of a common family. They differ from CH by having energetic standing eddies and other departures from zonal invariance. On the other hand, they do retain an approximate zonal symmetry (reflection about the basin center; the equivalence of the up- and downstream sides of the gap), and their mean energy, momentum, and potential vorticity budgets are broadly similar to each other and to those of CH (n.b., the standing eddy contributions do not dominate the budgets). It is plausible, therefore, that the processes identified in CH are occurring in these other cases as well, albeit with an extra degree of complexity. Furthermore, we can tentatively conclude that, while the presence of a narrow gap is important, the zonal length of the basin and a semiannual component in the wind do not make as substantial an alteration of the general circulation.

In contrast, the presence of a large topographic barrier in the gap does away with much of the simplicity seen in the other cases. The mean standing eddies dominate the zonal mean, the transports and energies are greatly reduced, and the energy budgets indicate a mixed baroclinic and barotropic eddy generation mechanism. Closed gyres with partial Sverdrup balances are present both north and south of the jet. In addition, for the zonal mean momentum and potential vorticity budgets, the standing eddies (rather than the transient ones) produce the requisite interior fluxes, while the topographic drag and torque serve as the major sinks (rather than bottom friction). No vestige of zonal symmetry remains; the region downstream from the barrier is much more energetic than upstream. Particularly vexing is our inability to explain the regular but extremely long period oscillation seen most clearly in the transport (Fig. 9); the associated principal component has its maximum expression well away from the topography (Fig. 20).

In several respects, TB is our most realistic analog for the Antarctic Circumpolar Current. There is, in fact, a very large topographic barrier near the Drake Passage, in addition to sizable obstacles at other locations. (A two-layer, quasigeostrophic model can only crudely represent such topography; more vertical resolution and primitive equations would be required for any great precision.) The transports in all cases but TB are greatly excessive compared to observations; there seems little doubt that the topography plays a major role in regulating this. Finally, TB exhibits, more than any other case, plausible analogs to the Weddell Gyre and Falkland Current, immediately downstream from the gap (Fig. 2). Perhaps the greatest qualitative discrepancy between our model solutions and the observations is the substantially smaller horizontal scales in the latter, at least in the deep water near the Drake Passage (Bryden and Pillsbury, 1978).

We do feel, though, that these idealized calculations demonstrate the probable importance of geostrophic turbulent processes in describing the mean state of the Antarctic Circumpolar Current. Whatever ultimate skill in simulation models such as ours might exhibit, it seems most likely that only models with plausible turbulent processes can be viewed as adequate. For the success of any systematic effort to develop detailed simulations of the Antarctic, it seems to us imperative that much more globally extensive measurements of the ocean variability be obtained in order to indicate the types of theoretical studies which would be most relevant.

13. ACKNOWLEDGEMENTS

Ms. Karla Nolan helped prepare the manuscript for publication. This research was supported by the National Science Foundation through a grant to the National Center for Atmospheric Research.

APPENDIX A

The two-layer quasigeostrophic potential vorticity equations (1)—(2) with the boundary and auxiliary conditions (3)—(4) have been solved by standard finite-difference methods using a staggered velocity and streamfunction grid system (as in Arakawa's, 1966, Scheme C) and energy conserving formulas for Jacobian evaluations (see Holland (1978) for the vorticity equations). All of the budgets in section 2, as well as the vorticity equations, have finite difference forms which result from derivations, purely by finite difference mathematics, from the momentum equations on velocity grid points.

In solving (1)—(2), q_1 and q_3 are stepped forward in time at the interior grid points and the gap points. From new potential vorticity values we next obtain new streamfunctions.

We define the barotropic streamfunction by:

$$\phi \equiv (H_1\psi_1 + H_3\psi_3)/(H_1 + H_3) \equiv \hat{\phi} + c(t)\phi' \tag{A1}$$

Its two components $\hat{\phi}$ and ϕ' are determined as follows:

$$\nabla^2\hat{\phi}^{n+1} = (q_1^{n+1} + q_3^{n+1} - f_0 B)/(H_1 + H_3) - f$$

with:

$$\hat{\phi} = 0 \text{ on } \delta\Omega_N \text{ and } \delta\Omega_S, \text{ and } \nabla^2\phi' = 0 \text{ with } \phi' = \begin{cases} 0 & \text{on } \delta\Omega_N \\ 1 & \text{on } \delta\Omega_S \end{cases}.$$

The superscript $n + 1$ indicates the new time level. Using the third auxiliary condition in (4), we have an equation for $\mathrm{d}c/\mathrm{d}t$ from which c^{n+1} is determined. The new baroclinic streamfunction:

$$\psi \equiv \psi_1 - \psi_3 \equiv \hat{\psi} + c'(t)\psi' + c''(t)\psi''$$

is obtained from the following equations:

$$(\nabla^2 - \lambda^2)\hat{\psi}^{n+1} = \frac{q_1^{n+1}}{H_1} - \frac{q_3^{n+1}}{H_3} + \frac{f_0 B}{H_3}$$

where:

$$\lambda^2 = f_0^2(H_1 + H_3)/g' H_1 H_3$$

and:

$$\hat{\psi} = 0 \text{ on } \delta\Omega_N \text{ and } \delta\Omega_S ; \; (\nabla^2 - \lambda^2)\psi' = 0$$

with:

$$\psi' = \begin{cases} 0 \text{ on } \delta\Omega_N \\ 1 \text{ on } \delta\Omega_S \end{cases}$$

and:

$$(\nabla^2 - \lambda^2)\psi'' = 0$$

with $\psi'' = 1$ on $\delta\Omega_N$ and $\delta\Omega_S$. Using the second and the fourth auxiliary conditions in (4), we have a set of equations from which $(c')^{n+1}$ and $(c'')^{n+1}$ can be determined. Then ψ_1^{n+1} and ψ_3^{n+1} are obtained from ϕ^{n+1} and ψ^{n+1}, and the boundary values of q_1^{n+1} and q_3^{n+1} filled in using the relations (2)—(4). In the evaluation of the Jacobian terms, the grid points representing y_S and y_N must be treated as interior points in order to satisfy the area conservation relations (e.g., $\iint J(\psi, q) = \underset{\sim}{0}$).

To solve the Poisson equation for ϕ and the Helmholtz equation for $\hat{\psi}$ for the idealized geometry of the Antarctic Circumpolar region, we followed the algorithm developed by Buzbee et al. (1971) using direct methods to treat problems in irregular domains. The method of solution is first to represent the finite-difference approximation to the Poisson equation as a matrix equation. The algorithm for solving such an equation ($A\underset{\sim}{v} = \underset{\sim}{y}$) requires modifying $\underset{\sim}{A}$ and $\underset{\sim}{y}$ so that a different matrix equation $B\underset{\sim}{z} = \underset{\sim}{w}$ can be solved by an efficient direct method and then the solution $\underset{\sim}{v}$ constructed from $\underset{\sim}{z}$. The procedure is as follows:

(1) Partition A and $\underset{\sim}{y}$ in the form:

$$A = \begin{pmatrix} A_1 \\ A_2 \end{pmatrix} ; \qquad \underset{\sim}{y} = \begin{pmatrix} \underset{\sim}{y}_1 \\ \underset{\sim}{y}_2 \end{pmatrix} \tag{A5}$$

Define:

$$B = \begin{pmatrix} B_1 \\ A_2 \end{pmatrix} ; \qquad \underset{\sim}{\overline{y}} = \begin{pmatrix} \overline{\underset{\sim}{y}_1} \\ \underset{\sim}{y}_2 \end{pmatrix} \qquad \underset{\sim}{\overline{w}} = \begin{pmatrix} \underset{\sim}{w} \\ 0 \end{pmatrix} \tag{A6}$$

(2) Solve $B\underset{\sim}{z} = \overline{\underset{\sim}{w}}$ by a direct method and compute $C = A_1\underset{\sim}{z}$.

(3) Solve $B\overline{\underset{\sim}{x}} = \overline{\underset{\sim}{y}}$ by a direct method.

(4) Solve $C\underset{\sim}{\beta} = \underset{\sim}{y}_1 - A_1\overline{\underset{\sim}{x}}$ by pivoted Gauss elimination (C is a $p \times p$ matrix). Then the solution $\underset{\sim}{v}$ can be computed from:

$$\underset{\sim}{v} = \overline{\underset{\sim}{x}} + \underset{\sim}{z}\underset{\sim}{\beta} \tag{A7}$$

For our system, we define:

$$A_1 = (\hat{A} I_2 0 I_2) \tag{A8}$$

A_1 is a $p \times (n \times m + p)$ matrix where p is the number of gap points, n is the column dimension and m is the row dimension. $\hat{A}$ is a $p \times p$ tridiagonal coefficient matrix, and I_2 is a $p \times m$ identity matrix with unity on the diagonals in the gap point positions and zero elsewhere. $\underset{\sim}{y}_1$ is the forcing function of length p associated with the gap points. B_1 is a $p \times (n \times m + p)$ matrix of the form:

$$B_1 = (\hat{I}\, 0) \tag{A9}$$

$\hat{I}$ is a $p \times p$ identity matrix. $\overline{\underset{\sim}{w}}$ is defined to be the transpose of B_1, and $\overline{\underset{\sim}{y}}_1$ is taken to be $\underset{\sim}{1}$.

APPENDIX B. RELATIONS AMONG EDDY FLUXES

It is possible to derive a set of relations among various eddy fluxes which appear in the mean momentum, energy, and potential vorticity budgets of section 2. We shall do this for circumstances which do not precisely conform to any of the cases defined in section 3, but which are certainly similar; namely, a periodic channel which is not necessarily invariant in the zonal direction. The "mean" which is relevant here is a combined time and zonal average (denoted by ~). The departures from this mean, the "eddies" (denoted by ^), thus combine the standing and transient eddies; for averaged quadratic quantities, this combination is a simple sum of the two types of individual eddy fluxes.

Consider the loss rate for mean zonal momentum in a layer. From (18)—(20), the vertical momentum flux divergence is equivalent to an interfacial pressure drag contribution defined by:

$$D = -\widetilde{\hat{p}\hat{h}_x} \tag{B.1}$$

where p is the layer pressure ($=f_0\psi$) and h the layer thickness. This also is proportional to an eddy thickness flux, or an eddy mass flux, as can be shown by an integration by parts zonally:

$$D = f_0 \widetilde{\hat{v}\hat{h}} \tag{B.2}$$

The momentum loss rate (B.1) is, furthermore, proportional to a horizontal heat or buoyancy flux. We can define interfacial buoyancy and temperature fluctuations by:

$$\begin{aligned} \hat{\rho}_\text{I} &= -\frac{2}{H}\frac{\rho_0 f_0}{g}(\hat{\psi}_1 - \hat{\psi}_3) \\ \hat{T}_\text{I} &= -\hat{\rho}_\text{I}/\rho_0\alpha \end{aligned} \tag{B.3}$$

where ρ_0 is a reference density and α the coefficient of thermal expansion. Then, in combination with an interfacial velocity,

$$\underset{\sim}{v}_I = (H_3\underset{\sim}{v}_1 + H_1\underset{\sim}{v}_3)/H \tag{B.4}$$

the meridional eddy fluxes are given by:

$$\begin{aligned} \widetilde{\hat{v}_I\hat{\rho}_I} &= -\frac{2\Delta\rho}{f_0 H} D_1 \\ \widetilde{\hat{v}_I\hat{T}_I} &= \frac{2\Delta\rho}{\alpha\rho_0 f_0 H} D_1 \end{aligned} \tag{B.5}$$

where D_1 is the upper layer form of (B.1). For isothermal top and bottom boundary conditions, vertical integrals of the fluxes (B.5) are approximated, in a two layer fluid, by multiplying the interfacial fluxes by $H/2$.

A baroclinic energy conversion rate is, from (7)—(9), defined by:

$$\{\tilde{P}, \hat{P}\} = f_0 \int_0^{L_y} \tilde{w}(\tilde{\psi}_3 - \tilde{\psi}_1)\,\mathrm{d}y \tag{B.6}$$

An integration by parts yields:

$$\{\tilde{P}, \hat{P}\} = \int_0^{L_y} (\tilde{u}_1 - \tilde{u}_3)D_1\,\mathrm{d}y \tag{B.7}$$

which indicates that this conversion is effected by the product of the upper layer momentum loss rate and the vertical difference in mean zonal velocities. Clearly one could write analogous formulas for the conversions $\{\tilde{K}_i, \tilde{P}\}$. By use of (B.5), (B.7) may be alternatively expressed in terms of heat transports as:

$$\{\tilde{P}, \hat{P}\} = -\alpha g \int_0^{L_y} \int_{-H}^{0} \widetilde{\hat{v}\hat{T}}(\tilde{T}_y/\tilde{T}_z)\,\mathrm{d}y\,\mathrm{d}z \tag{B.8}$$

The loss rate of mean potential vorticity from eddy fluxes of vortex stretching [see (21)—(22)] can be written for the ith layer as:

$$-[b_i + d_i] = -\frac{1}{H_i}\frac{\partial}{\partial y}(D_i) \tag{B.9}$$

We can also identify Taylor's (1921) horizontal particle diffusivity with the momentum loss rate. For a particle originally at a rest latitude y_*, we define its meridional departure by $\hat{\eta} = (y(t) - y_*)$, where $y(t)$ is its latitude at time t. For times short compared to diffusion across the channel (so that particle has not yet significantly changed its mean environment), but long compared to an eddy circulation time, the diffusivity K is defined by:

$$K = \frac{\mathrm{d}}{\mathrm{d}t}\langle \tfrac{1}{2}\hat{\eta}^2 \rangle \tag{B.10}$$

The brackets indicate an ensemble average over many realizations of particle diffusion about y_*. Since $(\mathrm{d}/\mathrm{d}t)\hat{\eta} = \hat{v}$, it follows that:

$$K = \langle \hat{\eta}\hat{v} \rangle \tag{B.11}$$

When there also exists a mean meridional potential vorticity gradient, a particle at $\hat{\eta}$ will, if potential vorticity is approximately conserved with the motion, have an anomalous value:

$$\hat{q} = -\frac{\partial \tilde{q}}{\partial y}\hat{\eta} \tag{B.12}$$

at least for small $\hat{\eta}$, (i.e., small compared to the scale of $\tilde{q}(y)$ changes).
(B.11)–(B.12) imply:

$$K = -\langle \hat{v}\hat{q} \rangle / \tilde{q}_y = -\widetilde{\hat{v}\hat{q}}/\tilde{q}_y \tag{B.13}$$

The ensemble average for vorticity flux is equal to the time and zonal average. Thus, by the definition of q, we obtain for layer i:

$$\begin{aligned} K_i \frac{\partial \tilde{q}_i}{\partial y} &= f_0 \widetilde{\hat{v}_i \hat{h}_i} + H_i \frac{\partial}{\partial y}(\widetilde{\hat{u}_i \hat{v}_i}) \\ &= D_i - (C_i + B_i) \end{aligned} \tag{B.14}$$

where $C_i + B_i$ is a horizontal Reynolds stress divergence as in (19). A meridional integral of (B.14) across the channel yields

$$\int K_i \frac{\partial \tilde{q}_i}{\partial y}\,\mathrm{d}y = \int D_i\,\mathrm{d}y \tag{B.15}$$

Note that for $D_1 > 0$, $D_3 < 0$, $\partial \tilde{q}_1/\partial y > 0$, and $\partial \tilde{q}_3/\partial y < 0$, as in our channel solutions, the integrated diffusivity in (B.15) is positive. From (B.14) we see that K will be point-wise positive wherever $D_i - (C_i + B_i)$ is of the same sign as $\partial \tilde{q}_i/\partial y$. From Fig. 21, this is true almost everywhere in the upper layer for the channel case; only on the extreme meridional edges is K_1 slightly negative.

Finally, we note that, in our 2-layer model, D is a purely internal transfer, hence:

$$\int_{-H}^{0} \int_{0}^{L_y} D\,\mathrm{d}y\,\mathrm{d}z = 0$$

This implies:

$$\int_{0}^{L_y} \int_{-H}^{0} K \frac{\partial \tilde{q}}{\partial y}\,\mathrm{d}y\,\mathrm{d}z = 0 \tag{B.16}$$

which is a form of the theorem derived by Bretherton [1966, eq. (13)].

REFERENCES

Arakawa, A., 1966. Computational design for long term numerical integration of the equations of fluid motion: Two-dimensional incompressible flow. Part I. J. Comput. Phys., 1: 119—143.

Baker, D.J., Nowlin, W.D., Pillsbury, R.D. and Bryden, H., 1977. Antarctic Circumpolar Current: Space and time fluctuations in the Drake Passage. Nature, 268: 696—699.

Batchelor, G.K., 1969. Computation of the energy spectrum in homogeneous two-dimensional turbulence. Phys. Fluids Suppl., 12 (II): 233—239.

Brekhovskikh, L.M., Fedorov, K.N., Fomin, L.M., Koshlyakov, M.N. and Yampolsky, A.D., 1971. Large-scale multi-buoy experiment in the tropical Atlantic. Deep-Sea Res., 18: 1189—1206.

Bretherton, F.P., 1966. Critical layer instability in baroclinic flows. Q. J. R. Meteorol. Soc., 92: 325—334.

Bretherton, F.P. and Haidvogel, D.B., 1976. Two-dimensional turbulence above topography. J. Fluid Mech., 78: 129—154.

Bryden, H., 1977. Poleward heat flux, conversion of available potential energy, and baroclinic instability in the Drake Passage. J. Mar. Res., submitted.

Bryden, H. and Pillsbury, D., 1978. Variability of deep flow in the Drake Passage. J. Phys. Oceanogr., in press.

Cox, M.D., 1975. A baroclinic numerical model of the World Ocean: preliminary results. Numerical Models of Ocean Circulation. Natl. Acad. of Sciences, Washington, D.C., pp. 107—120.

Crease, J., 1964. The Antarctic circumpolar current and convergence. Proc. R. Soc. London, 281: 14—21.

Davis, R.E., 1976. Predictability of sea surface temperature and sea level pressure anomalies over the North Pacific Ocean. J. Phys. Oceanogr., 6: 249—266.

Dickinson, R.E., 1968. Planetary Rossby waves propagating vertically through weak westerly wind wave guides. J. Atmos. Sci., 25; 984—1002.

Dickinson, R.E., 1971. Cross-equatorial eddy momentum fluxes as evidence of tropical planetary wave sources. Q. J. R. Meteorol. Soc., 97: 554—558.

Fandry, C.B., 1971. A three-dimensional model of the Antarctic circumpolar current. GFDL Paper No. 35, Monash University.

Fofonoff, N., 1955. A Theoretical Study of Zonally Uniform Oceanic Flow. Thesis, Brown University.

Freeland, H., Rossby, T. and Rhines, P., 1975. Statistical observations of the trajectories of neutrally buoyant floats in the North Atlantic. J. Mar. Res., 33: 383—404.

Gill, A.E., 1968. A linear model of the Antarctic circumpolar current. J. Fluid Mech., 32: 465—488.

Gill, A.E. and Bryan, K., 1971. Effects of geometry on the circulation of a three-dimensional southern-hemisphere ocean model. Deep-Sea Res., 18: 685—721.

Green, J., 1970. Transfer properties of the large-scale eddies and the general circulation of the atmosphere. Q. J. R. Meteorol. Soc., 96: 157—185.

Haidvogel, D.B., 1976. The Sensitivity and Predictability of Mesoscale Eddies in an Idealized Ocean Model. Thesis, Massachusetts Institute of Technology, 250 pp.

Haidvogel, D.B. and Holland, W.R., 1978. The stability of ocean currents in eddy-resolving general circulation models. J. Phys. Oceanogr., in press.

Hart, J., 1976. The modulation of an unstable baroclinic wave field. J. Atmos. Sci., 33: 1874—1889.

Hidaka, K. and Tsuchiya, M., 1953. On the Antarctic Circumpolar Current. J. Mar. Res., 12: 214—222.

Holland, W.R., 1977. Numerical models of ocean circulation with mesoscale eddies. Proc. of the POLYMODE Theoretical Institute, August 1976, Yalta, U.S.S.R.

Holland, W.R., 1978. The role of mesoscale eddies in the general circulation of the ocean — numerical experiments using a wind-driven quasigeostrophic model. J. Phys. Oceanogr., in press.

Holland, W.R. and Lin, L.B., 1975a. On the origin of mesoscale eddies and their contribution to the general circulation of the ocean. I. A preliminary numerical experiment. J. Phys. Oceanogr., 5: 642—657.

Holland, W.R. and Lin, L.B., 1975b. On the origin of mesoscale eddies and their contribution to the general circulation of the ocean. II. A parameter study. J. Phys. Oceanogr., 5: 658—669.

Kamenkovich, V.M., 1962. On the theory of the Antarctic circular current. Tr. Inst. Okeanol. Akad. Nauk S.S.S.R., 56: p. 241.

Kidson, J.W., Vincent, D.G. and Newell, R.E., 1969. Observational studies of the general circulation in the tropics: long term mean values. Q. J. R. Meteorol. Soc., 95: 258—287.

Kuo, H.-L., 1951. Dynamical aspects of the general circulation and the stability of zonal flow. Tellus, 51: 268—284.

McWilliams, J.C., 1976a. Maps from the Mid-Ocean Dynamics Experiment. Part I. Geostrophic streamfunction. J. Phys. Oceanogr., 6: 810—827.

McWilliams, J.C., 1976b. Maps from the Mid-Ocean Dynamics Experiment. Part II. Potential vorticity and its conservation. J. Phys. Oceanogr., 6: 828—846.

McWilliams, J.C., 1977a. On a class of stable, slightly geostrophic mean gyres. Dyn. Atmos. Oceans, 2: 19—28.

McWilliams, J.C., 1977b. A note on a consistent quasigeostrophic model in a multiply-connected domain. Dyn. Atmos. Oceans, 1: 427—441.

McWilliams, J.C., 1977c. Stable jet modes: a special case of eddy and mean flow interaction. J. Phys. Oceanogr., in press.

Munk, W. and Palmén, E., 1951. Note on the dynamics of the Antarctic Circumpolar Current. Tellus, 3: 53—55.

Nowlin, W., Whitworth, J. and Pillsbury, R.D., 1977. Structure and transport of the Antarctic Circumpolar Current at the Drake Passage from short term measurements. J. Phys. Oceanogr., in press.

Phillips, N., 1954. Energy transformations and meridional circulations associated with simple baroclinic waves in a two-level, quasigeostrophic mode. Tellus, 6: 273—286.

Rhines, P.B., 1975. Waves and turbulence on a β-plane. J. Fluid Mech., 69, 417—443.

Rhines, P.B., 1977. The dynamics of unsteady currents. The Sea, 6: 189—318.

Robinson, A. and McWilliams, J., 1974. The baroclinic instability of the open ocean. J. Phys. Oceanogr., 4: 281—294.

Robinson, A.R., Harrison, E., Mintz, Y. and Semtner, A.J., 1977. Eddies and the general circulation of an idealized oceanic gyre: a wind and thermally driven primitive-equation numerical experiment. J. Phys. Oceanogr., 7: 182—207.

Salmon, R.L., Holloway, G. and Hendershott, M.C., 1976. The equilibrium statistical mechanics of simple quasi-geostrophic models. J. Fluid Mech., 75: 691—704.

Sasamori, T. and Melgarejo, J., 1977. A parameterization of large-scale heat transport in mid-latitudes. Part I. Transient eddies. Tellus, submitted.

Schulman, E.E., 1970. The Antarctic Circumpolar Current. Proc. of the 1970 Summer Computer Simulation Conf., June 1970, Denver.

Semtner, A.J. and Holland, W.R., 1977. Intercomparison of quasigeostrophic simulations of the western North Atlantic circulation with primitive-equation results. J. Phys. Oceanogr., in press.

Semtner, A.J. and Mintz, Y. 1977. Numerical simulation of the Gulf Stream and mid-ocean eddies. J. Phys. Oceanogr., 7: 208—230.

Simmons, A., 1974. The meridional scale of baroclinic waves. J. Atmos. Sci., 31: 5115—5125.

Simmons, W. and the MODE Group, 1977. The Mid-Ocean Dynamics Experiment. Deep-Sea Res., in press.
Starr, V.P., 1951. A note on the eddy transport of angular momentum. Q. J. R. Meteorol. Soc., 77: 44—50.
Stommel, H., 1957. A survey of ocean current theory. Deep-Sea Res., 4: 178—184.
Stone, P., 1974. The meridional variation of the heat fluxes by baroclinic waves and their parameterization. J. Atmos. Sci., 31: 444—456.
Stone, P., 1977. Baroclinic adjustment. J. Atmos. Sci., in press.
Sverdrup, H.U., 1947. Wind-driven currents in a baroclinic ocean; with application to the equatorial currents of the eastern Pacific. Proc. Natl. Acad. Sci., 33 (11): 318—326.
Tennekes, H., 1977. The general circulation of two-dimensional turbulent flow on a beta plane. J. Atmos. Sci., 34: 702—712.
U.S. POLYMODE Organizing Committee, 1976. U.S. POLYMODE Program and Plan, Polymode office, 15-1417, MIT Cambridge, 87 pp.
Van Loon, H., 1971. A half-yearly variation of the circumpolar surface drift in the Southern Hemisphere. Tellus, 23: 511—516.
Wyrtki, K., 1960. The Antarctic Circumpolar Current and the Antarctic Polar Front. Dtsch. Hydrogr. Z., 13: 153—174.
Wyrtki, K., 1976. Eddy energy in the oceans. J. Geophys. Res., 81: 2641—2646.